# Integrated Optical Parametric Generators And Oscillators For The Mid-Infrared (MIR) Range

**Thesis**

Submitted to the
Department of Physics, Faculty of Science
University of Paderborn, Germany
for the degree
Doktor der Naturwissenschaften (Dr. rer. nat.)

by

Sergey Orlov

Reviewers:
1. Prof. Dr. W. Sohler
2. Prof. Dr. K. Lischka

Submitted on: October 30, 2008

Oral examination: January 23, 2009

*To my* $\boxed{\textit{father}}$...

# Contents

# Chapter 1

# Introduction

## 1.1 Background

The infrared spectral range of electromagnetic (EM) radiation, which extends roughly from $3\times10^{11}$ Hz to about $4\times10^{14}$ Hz, was first detected by the renowned astronomer Sir William Herschel (1738-1822) in 1800. As the name implies, this band of EM-radiation has the wavelength longer than red light. The infrared, or IR, is often subdivided into four regions: the *near* IR, that is near the visible, (780 - 3000 nm), the *intermediate* IR (3000 - 6000 nm), the *far* IR (6000 - 15000 nm), and the *extreme* IR (15000 nm - 1.0 mm). This is again a rather loose definition.

Mid-infrared (MIR) radiation, which will be described in this thesis, will cover the wavelength range from $2 < \lambda < 4$ $\mu$m. Therefore the spectral range between visible light and 2 $\mu$m will be called in this work as near infrared (NIR).

Radiant energy at the long-wavelength extreme can be generated by either microwave oscillators or incandescent sources. Indeed, any material will radiate and absorb IR via thermal agitation of its constituent molecules [1].

The molecules of any object at a temperature above absolute zero (-273 °C) will radiate IR, even if only weakly. On the other hand, infrared radiation is highly emitted in a continuous spectrum from hot bodies, such as electric heaters, glowing coals, and ordinary house radiators.

Besides rotating, a molecule can vibrate in several different ways, with its atoms moving in various directions with respect to one another. The molecules need not to be polar, and even a linear system such as $CO_2$ has three basic vibrational modes and a number of energy levels, each of which can be excited by photons. The associated vibrational emission and absorption spectra are, as a rule, in the IR (1000 nm to 0.1 mm).

Thus, it is in this spectral region that most molecules will absorb infrared radiation at characteristic wavelengths determined by their atomic composition and bond structure. As a result, most molecules will absorb infrared radiation in such a way as to produce a unique infrared absorption „fingerprint“. For example, Fig. 1.1 shows the infrared spectra of methane, ethane and ethylene. The absorption bands, seen

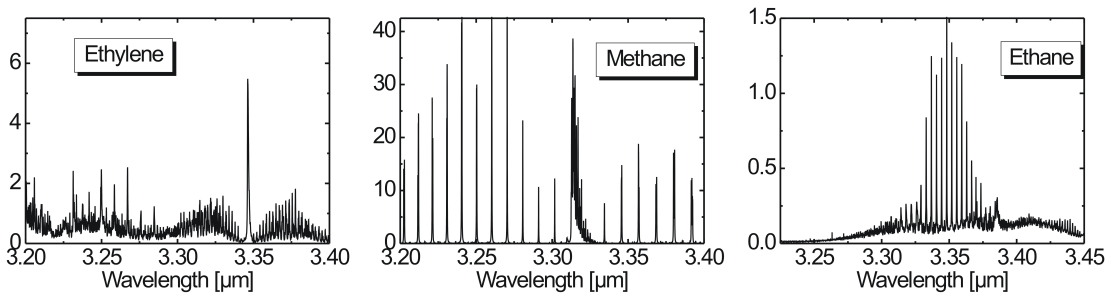


**Figure 1.1:** Examples of absorption spectra in the MIR range [2].

in the spectra, correspond to a specific vibrational mode of the molecules. Since the molecules contain different types of atoms that have different bonds, they produce different characteristic infrared „fingerprints“ [3].

While one of the advantages of working in the middle-infrared is that this region covers the vibrational frequencies of most molecules, it should be noted that this can also be a problem. The infrared spectra of complex samples can be quite confusing since they will contain the overlapping absorption bands of many different molecular species. This can make the interpretation of the spectra very difficult. In some cases, different samples having distinctly different, but related molecules can produce spectra that are nearly identical. An excellent example of this is provided by the infrared spectra of DNA[1]. The DNA molecules of different living species (or even members of the same species for that matter) differ from each other in the order in which their nucleotides are arranged in large numbers of ways. Despite all of these differences, however, the infrared spectra of all DNA looks essentially the same, independent of whether it is from a bacterium, a fish, or a person (a humbling thought). This is because all DNA is made up of four main molecular structures with their characteristic interatomic bonds and they, but not the overall molecules that are being probed by the infrared spectra.

These are some examples of the great interest to this part of an EM-radation. The variety of these and other applications in MIR spectral range are also listed here. Among them are remote sensing [4–7], spectroscopy [8–10], medicine [11, 12] and military countermeasures.

## 1.2 Motivation

Since more than 30 years integrated optics (IO) has proved to be a very dynamic and active area, with new significant development being made at very fast pace. The new area of integrated optics has been based primarily on the fact that light waves

[1]DNA - **D**eoxyribo**N**ucleic **A**cid is a nucleic acid molecule that contains the genetic instructions used in the development and functioning of all living organisms.

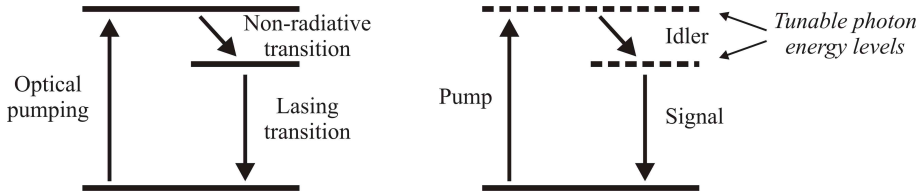


**Figure 1.2:** Optically pumped 3-level laser (left), and 3-photon optical parametric process (right).

can propagate through and be contained by very thin layers (films) of transparent materials. By combining such layers and shaping them into appropriate configurations, IO technology has realized a large variety of components which can perform a wide range of operations using an optical waves. Thus, light can be guided, modulated, deflected, filtered, radiated into space or, by using lasers, it can also be generated within a thin-film structure.

Other technological and scientific research of IO include new devices made possible by the development of thin-film structures having special properties, phenomena produced by the concentration of high intensity fields in thin films and effects due to the attendant enhancement of nonlinear and/or active properties of such films [13].

Lasers are basically discrete-wavelength sources of coherent radiation involving stimulated emission between quantized energy levels in a amplifying medium. Only when these quantized energy levels are tunable or there are neighbouring energy levels that are sufficiently broadened to merge into one another to form a continuous band, continuously tunable laser emission can be achieved. Even then, the tuning range tends to be limited. Since the invention of the laser, there has been a great deal of interest in the development of truly continuously and broadly tunable coherent radiation sources. Such sources would have broad applications in research and industry.

Optical parametric devices are powerful solid state sources of broadly tunable coherent radiation capable of covering the entire spectral range from the near UV to the MIR. They can be operated from continuous-wave down to the femtosecond time domain. They are nonlinear optical devices that convert laser radiation at one frequency to a continuously tunable spectral range through a three-wave parametric process in the whole transparency range of the material. As a result of recent progress in the development of lasers that can serve as pump sources for optical parametric devices, optical parametric oscillators and amplifiers are now becoming practical devices. Looking toward the future, it can be surely said, that research and development of new highly nonlinear materials as well as high power lasers for pumping of optical parametric oscillators and amplifiers and availability of them on the market, will result in fabrication of more efficient devices for already discovered wavelength and extend it to the new wavelength range [14].

Optical parametric devices are in many ways analogous to the optically-pumped 3-level laser (Fig. 1.2). Thus, many of the techniques and device physics issues for lasers such as the exact mode properties, the transverse and longitudinal mode field distributions, line-narrowing schemes, noise properties, soliton formation, and effect

of phase-conjugation mirrors, squeezing, and microcavity on the emission process, etc. are also relevant to the parametric devices. There are, however, also a number of important differences. Instead of discrete energy levels as in the laser, tunable photon energy levels are involved in the optical parametric devices. As shown in Fig. 1.2, for these devices, the virtual energy level can be tuned through the phase-matching condition, and the top energy level can be tuned by tuning the pump frequency. In the laser, because the involved radiative processes are the single-photon transitions and because of the possible involvement of nonradiative transitions, the temporal and spatial coherence properties of the laser output are not directly related to those of the pump radiation. In the optical parametric devices, where are no non-radiative transitions involved, and the whole process is a single three-photon process. The temporal and spatial coherence properties of these devices are, therefore, directly related to those of the pump and cavity. The pump source for a laser can, therefore, be a coherent or an incoherent source, whereas the pump source of the optical parametric devices must be a laser (Nowadays some theoretical publications show, that the coherent radiation in the nonlinear optical devices can also be built up using an incoherent pump source [15, 16]). Also, because the laser involves three single-step resonant transitions while the parametric process involves a single three-photon transition, the cross-sections for the parametric process are generally much smaller than those for the stimulated emission process in lasers. The threshold for oscillation is, therefore, generally much higher for OPO's than that for the lasers. On the other hand, above the threshold for oscillation, OPOs can be very efficient devices because there is no non-radiative process involved; there is in principle no loss. The quantum efficiency of the OPO can potentially be 100% with all used pump photons converted to useful output photons.

While the importance of OPOs as useful source of tunable coherent radiation was clear from beginning and a variety of theoretical and experimental studies were carried out, the realization of practical OPO technology was hampered by the lack of suitable nonlinear optical crystals. Progress in the search of these crystals was slowly being made during the past decade, leading to many new nonlinear optical crystals (e. g. $\beta$-$Ba_2O_4$, $LiB_3O_5$, L-arginine phosphate, MgO:$LiNbO_3$, $KTiOPO_4$ and its isomorphs). This, along with the steady improvement in the quality of efficient nonlinear crystals such as $KNbO_3$, $AgGaS_2$, $AgGaSe_2$, $ZnGeP_2$, and $Tl_3AsSe_3$, has led to the recent rapid progress in optical parametric oscillator technology.

The desirable properties of OPO crystals are: broad transparency, high nonlinearity, sufficient birefringence for phase matching, high damage threshold, good temperature stability, low optical loss, chemical inertness and ease of sample fabrication.

Using natural material birefringence of the crystal it would be possible to convert pump wavelength into the newly generated wave, according to the dispersion properties. This so called *true* or birefringent phase-matching allow at relative low expenses to generate tunable radiation in the limited wavelength range. Proposed for the first time by Armstrong etc. [17] in the early sixties modulation of the direction of the optical axis and therefore a nonlinear coefficient has led to the new turn in the generation of new frequencies on one hand and new researches have been taken place in discov-

ering of microdomain ferroelectric gratings of a high quality to extend the existing wavelength range on another. Nowadays such ferroelectric gratings have been already reported in the sub-micron range by, for instance, molecular e-beam writing [18] or UV illumination [19]. This technique might be utiluzed for bulk devices as well as for integrated optics.

Contrary to bulk configurations nonlinear integrated optical waveguides promise conversion efficiencies, which can exceed those of bulk optical approaches by several orders of magnitude. Moreover, if quasi phase matching is used in periodically poled $LiNbO_3$ waveguides, the largest nonlinear coefficient $d_{33}$ can be exploited and MIR spectral range can be adjusted by a corresponding periodicity of a ferroelectric domain grating [20, 21].

## 1.3 Organization of the Thesis

This thesis is based on nonlinear $\chi^{(2)}$ interaction in the titanium indiffused periodically poled lithium niobate (Ti:PPLN or Ti:$LiNbO_3$) and is divided into several chapters.

Chapter 2 starts with the waveguide model and light propagation along the waveguide. It also gives an introduction into nonlinear optics and quasi-phase matching, comparing it with the birefringent phase matching.

Chapter 3 will describe the fabrication of the optical waveguides, starting with 4 inch wafers, available on the market. Each state will be discussed here step by step. Fabricated Ti:PPLN sample first of all has to be characterized for the optical losses. Waveguide inhomogeneities and damping are crucial points for an effective generation of new wavelengths, which may dramatically drop the efficiency of nonlinear processes. Used technique will be shortly presented here. Measured results will be discussed.

In chapter 4 Optical Parametric Generation will be discussed. It starts with coupled mode equations of the interacting waves and continues to describe the development of the power along the waveguide for the phase matching conditions for both generated signal and idler waves.

Experimental setup is quite similar for all experiments, described here, with some minor changes, which will be pointed out every time it is necessary.

These devices will find application in spectroscopy and therefore tunability is one of the main characteristics. Experimental results will be compared here with theoretical calculations.

Measured power characteristics, starting with few nW using lock-in technique, will be also presented. Continuous increase of the output power level by using more efficient and high power pumping and comparison with theory, where the pump depletion cannot be neglected any more, is also discussed.

Integrated OPOs are more complicated devices, consisting not only of a nonlinear medium, but also mirrors (external or deposited), will be discussed in chapter 5. Mirror characteristics will be compared for both cases. A major advantage of doubly resonant OPOs is their low threshold. Present status and future development will be given.

OPOs may be pumped not only in cw-mode, but also using a pulsed pump source.

In this case the generated pulses have to be synchronized with the pump pulses. Characteristics of this device, its unique properties as well as power levels will be shown.

Chapter 6 will summarize all achieved results. Also the main problems will be pointed out once again and possible future activities will be discussed.

In appendices some additional information will be given, which extends measured results or some attempt, which were done, but did not get at the moment any results to be discussed inside the relevant chapter.

# Chapter 2

# Theoretical Background

## 2.1 Waveguide Model

The theoretical description of the waveguide will be explained here. First investigations of an indiffusion of titanium into lithium niobate have been done in early seventieth. The diffusion kinetics and a waveguiding for a stripe waveguide can be found in [22, 23]. In Fig. 2.1 the sample orientation is shown in a laboratory coordinate system. The capital letters correspond to crystallographic axes of lithium niobate; small letters - to the laboratory coordinate system.

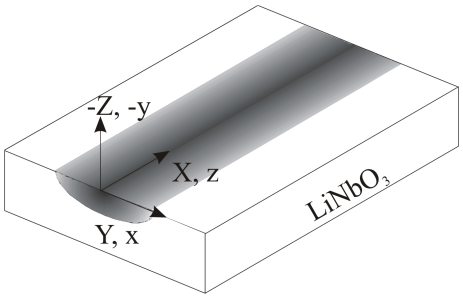


**Figure 2.1:** The orientation of Z-cut X-propagation stripe Ti:$LiNbO_3$ waveguide in laboratory coordinate system (small letters).

The indiffusion of a titanium layer in $LiNbO_3$ can be described by Fick's law of diffusion [24]:

$$c_{Ti}(x,y) = c_0 f(x) g(y) \tag{2.1}$$

with

$$f(x) = \frac{1}{2erf(\frac{W}{2D_x})}\left[erf\left(\frac{x+\frac{W}{2}}{D_x}\right) - erf\left(\frac{x-\frac{W}{2}}{D_x}\right)\right] \tag{2.2}$$

$$g(y) = exp\left(-\frac{y^2}{D_y^2}\right), \tag{2.3}$$

where $W$ is the width of the titanium stripe before indiffusion and $D_x, D_y$ are diffusion depths, which are related via

$$D_{x,y} = 2\sqrt{\tilde{D}_{x,y} t_D} \tag{2.4}$$

to the diffusion coefficients $\tilde{D}_{x,y}$ and to the diffusion time $t_D$. Diffusion coefficients in turn can be found from

$$\tilde{D}_{x,y} = \tilde{D}^0_{x,y} exp\left(-\frac{Q_{x,y}}{k_B T_D}\right), \tag{2.5}$$

where $\tilde{D}^0_{x,y}$ are the diffusion constants, $Q_{x,y}$ are the activation energies, $k_B$ is the Boltzmann constant and $T_D$ is the diffusion temperature [25]. $c_0$ in Eq. 2.1 is the $Ti$ concentration at the surface in the coordinate origin:

$$c_0 = \frac{2 d_{Ti} \rho_{Ti}}{\sqrt{\pi} D_y} erf\left(\frac{\omega_{Ti}}{2 D_x}\right), \tag{2.6}$$

where $d_{Ti}$ is the thickness of the deposited Ti-layer and $\rho_{Ti}$ - particle density of metallic Ti ($5.67 \times 10^{22}\ cm^{-3}$) [26].

The local increase of the extraordinary $\delta n_e(x, y, \lambda)$ and ordinary $\delta n_o(x, y, \lambda)$ refractive index with respect to the bulk value is related to $c_{Ti}(x, y)$ by [27]:

$$\begin{aligned} \delta n_e(x, y, \lambda) &= \frac{0.839 \cdot (\lambda/\mu m)^2}{(\lambda/\mu m)^2 - 0.0645} E\, c_{Ti}(x, y) \\ \delta n_o(x, y, \lambda) &= \frac{0.67 (\lambda/\mu m)^2}{(\lambda/\mu m)^2 - 0.13} (F\, c_{Ti}(x, y))^{\gamma} \end{aligned} \tag{2.7}$$

with

$$E = 1.2 \times 10^{-23}\,\mathrm{cm}^3$$

$$F = 1.3 \times 10^{-25}\,\mathrm{cm}^3$$

$$\gamma = 0.55$$

The starting point to describe propagation of an electromagnetic wave in a waveguide is the Maxwell's equations [1]. As in this work only lithium niobate is considered, which is a dielectric, nonmagnetic material ($\vec{j} = 0$, $\vec{\rho} = 0$, i.e. no free electron current and charge density) - these equations can be written in the form:

$$\begin{aligned} \nabla \times \vec{E}(\vec{r}, t) &= -\dot{\vec{B}}(\vec{r}, t) \\ \nabla \vec{D}(\vec{r}, t) &= 0 \\ \nabla \times \vec{B}(\vec{r}, t) &= \mu_0 \dot{\vec{D}}(\vec{r}, t) \\ \nabla \vec{B}(\vec{r}, t) &= 0, \end{aligned} \tag{2.8}$$

where $\nabla = (\partial/\partial x,\, \partial/\partial y,\, \partial/\partial z)$, and $\vec{E}, \vec{B}, \vec{D}$ are the time dependent vectors of the electric and magnetic field, and the electric displacement, respectively. Assuming the periodical time dependence, the electrical field, for example, is:

$$\vec{E}(\vec{r},t) = \frac{1}{2}\left[A_0(z)\,\vec{E_0}(x,y)\,\exp(i(\omega t - \beta z)) + \,c.c.\right]^{\,1} \tag{2.9}$$

where $\vec{E}(\vec{r},t)$ is divided into longitudinal component with the amplitude $A_0(z)$ along the z-axis and vector $\vec{E_0}(x,y)$, oriented perpendicular to the propagation direction; $\omega$ is the angular frequency and $\beta$ is the wave vector component along the z-axis. Inserting ( 2.9) into equations (2.8) and doing the time derivative the time independent equations can be written as:

$$\begin{array}{rcl} \nabla \times \vec{E}(\vec{r},t) &=& -i\,\omega\,\vec{B}(\vec{r},t) \\ \nabla\vec{D}(\vec{r},t) &=& 0 \\ \nabla \times \vec{B}(\vec{r},t) &=& i\,\omega\,\mu_0\vec{D}(\vec{r},t) \\ \nabla\vec{B}(\vec{r},t) &=& 0. \end{array} \tag{2.10}$$

After applying the rotation operator ($\nabla\times$) to the first and third equations in (2.10) and assuming an isotropic medium, completed vector form of equations (2.10) may be written as:

$$\begin{array}{c} \Delta\vec{E} + \varepsilon\frac{\omega^2}{c^2}\vec{E} + \nabla\left[\vec{E}\left(\frac{\nabla\varepsilon}{\varepsilon}\right)\right] = 0 \\ \\ \Delta\vec{B} + \varepsilon\frac{\omega^2}{c^2}\vec{B} + \left(\frac{\nabla\varepsilon}{\varepsilon}\right)\times\left(\nabla\times\vec{B}\right) = 0 \end{array} \tag{2.11}$$

with permittivity $\varepsilon$ and light velocity $c$.

This set of equations can be separated and solved independently for two different modes: TM[2] ($\vec{E} = (0, E_y, E_z)$, $\vec{B} = (B_x, 0, 0)$) and TE ($\vec{E} = (E_x, 0, 0)$, $\vec{B} = (0, B_y, B_z)$). All 3 components of one polarization are related to each other by Maxwell's equations. It is possible just to solve the problem for one component, and two the other components can be calculated from the first one. *Transverse* electric and magnetic fields without any $z$-component may be found in the slab waveguide. But the stripe one, which is described in this work, has also a nonzero $z$-component in the direction of propagation. Therefore, it will be correct to call these modes quasi-TM (QTM) and quasi-TE (QTE) modes.

If the change of the index of refraction in the transverse direction is relative small, then scalar waveguide equation can be derived as [28]:

$$\begin{array}{rl} \text{QTM}: & \left(\frac{\partial^2}{\partial x^2} + \frac{n_y^2}{n_z^2}\frac{\partial^2}{\partial y^2} + \beta_0^2(n_y^2 - n_{eff}^2)\right)B_x = 0 \\ \\ \text{QTE}: & \left(\frac{n_x^2}{n_z^2}\frac{\partial^2}{\partial x^2} + \frac{\partial^2}{\partial y^2} + \beta_0^2(n_x^2 - n_{eff}^2)\right)E_x = 0, \end{array} \tag{2.12}$$

[1] c.c. - complex conjugate

[2] TM - **T**ransverse **M**agnetic; TE - **T**ranverse **E**lectric

where $n_{eff}$ is the effective index of refraction of the mode and $\beta_0 = 2\pi/\lambda$ is the wave propagation constant in vacuum.

The set of equations has no analytical solution. Therefore numerical methods, for example the Finite Element Method (FEM), can be used. Another good and relative quick and appropriate method can be the Gauss-Hermite-Gauss (GHG) approximation [29], where the mode profile is presented as a product of Gauss distribution in the lateral direction and Hermite-Gauss in the vertical:

$$\tilde{\Phi}(x,y) = \psi(x)\phi(y) \tag{2.13}$$

with

$$\psi(x) = \sqrt{\frac{2}{\sqrt{\pi}\theta}}\, exp\left(-\frac{2x^2}{\theta^2}\right)$$
$$\phi(y) = \frac{2}{\sqrt{\sigma\sqrt{\pi}}}\,\frac{y}{\sigma}\, exp\left(-\frac{y^2}{2\sigma^2}\right)$$

and

$$\tilde{\Phi}(x,y) = \begin{cases} B_x \text{ for QTM} \\ E_x \text{ for QTE} \end{cases} \tag{2.14}$$

The coefficients $\theta$ and $\sigma$ are chosen in that way to get a normalized function in form:

$$\int_{-\infty}^{\infty}\int_{0}^{\infty} \left|\tilde{\Phi}(x,y)\right|^2 dx\, dy = 1 \tag{2.15}$$

## 2.2 Nonlinear Polarization

Up to that time then the lasers were discovered, the physical laws allow to describe reflection, refraction, scattering and so on. In this, so called, linear optics the induced polarization $P$ in matter is proportional to the electric field $E$ of an optical wave [30]:

$$\vec{P} = \epsilon_0 \chi \vec{E} \tag{2.16}$$

where $\epsilon_0$ is the free-space permittivity and $\chi$ is the susceptibility of a given medium, which is independent of the field. This is usually true for lower field intensities. First observations of nonlinear dependence of the polarization from the optical field are found in 1961, where for the first time Second Harmonic Generation (SHG) was observed in a quartz crystal using powerful for that time ruby laser [31]. This, and later some other frequency mixing effects like optical sum- and difference-frequency generation, have led to revise Eq. 2.16 and to rewrite it in terms of power series:

$$\vec{P} = \epsilon_0 \left[\chi^{(1)}\vec{E} + \chi^{(2)}\vec{E}\vec{E} + \chi^{(3)}\vec{E}\vec{E}\vec{E} + ...\right] \tag{2.17}$$

where $\chi^{(1)}$, $\chi^{(2)}$, $\chi^{(3)}$ are first- second- and third-order susceptibilities, respectively. These material coefficients are usually tensors. The first one is responsible for all linear optical processes and is 3×3 tensor for lithium niobate with nonzero diagonal elements [32].

Second and third order terms are responsible for the nonlinear polarization, where electrical fields $E$ of the same or different frequencies might be involved into the interaction.

The response of the media is shown schematically in Fig. 2.2. If low field amplitudes are applied, then the induced polarization in the medium is proportional to the electrical field (Fig. 2.2 left). In the case of a nonlinear response, by applying a higher periodical optical field, this deflection in one direction will have a larger amplitude, than in the other (Fig. 2.2 right). This polarization response may be represented by a Fourier series of periodic functions of different frequencies, coming finally to the result (Eq. 2.17).

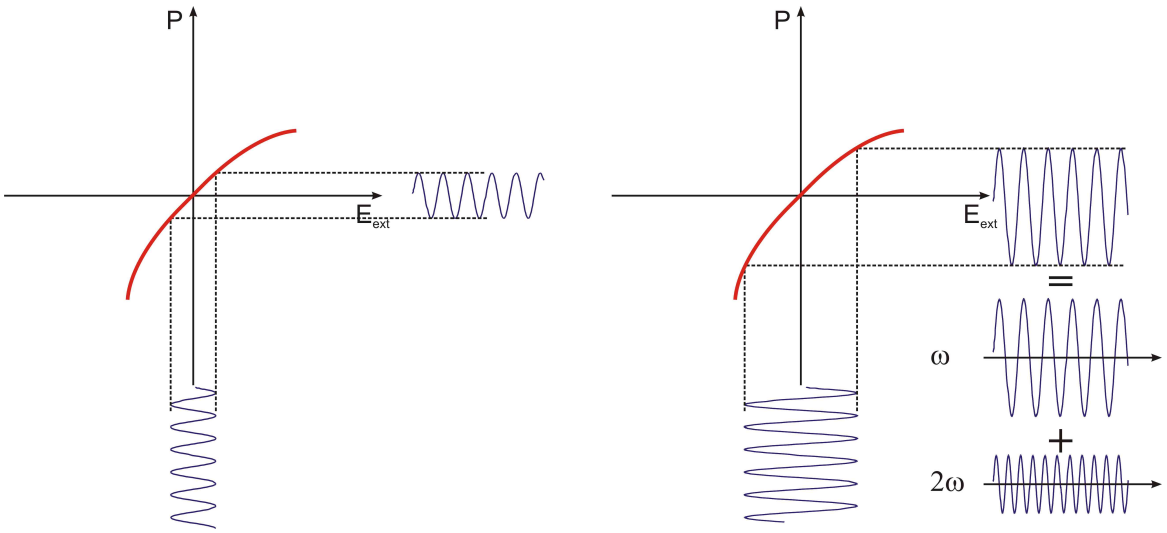


**Figure 2.2:** Relation between induced polarization of the medium on the electrical field in the case of linear (left) and nonlinear (right) interaction.

With the help of the $\chi^{(2)}$ tensor three-wave mixing in the following processes can be explained:

- Optical Rectification
- Second Harmonic Generation (SHG)
- Difference Frequency Generation (DFG)
- Sum Frequency Generation (SFG)
- Optical Parametric Generation (OPG)
- Optical Parametric Oscillators (OPO)

| $\lambda$ [nm] | $d_{ki}$ [pm/V] | | |
|---|---|---|---|
| | $d_{33}$ | $d_{31}$ | $d_{22}$ |
| 1313 | 19.5 | 3.2 | - |
| 1064 | 25.2 | 4.6 | 2.1 |
| 852 | 25.7 | 4.8 | - |

**Table 2.1:** Nonliear coefficients $d_{22}$, $d_{31}$ and $d_{33}$ for three different wavelengths, calculated from SHG process in bulk $LiNbO_3$.

- etc.

$\chi^{(3)}$ is responsible for so called four-wave mixing. This tensor can describe for example Kerr-effect, Brillouin- and Raman-scattering and so on.

All processes, described in this work, are based on $\chi^{(2)}$ tensor. Higher order susceptibilities will not be taken here any more into account. Therefore, second-order nonlinear polarization can be written as

$$P(\omega_3 = \omega_1 \pm \omega_2) \;=\; \epsilon_0 \chi^{(2)}(\omega_1, \omega_2)\, E(\omega_1)\, E(\omega_2) \tag{2.18}$$

This equation means, that the generation of a new frequency $\omega_3$ can be induced by two incident waves at frequencies $\omega_1$ and $\omega_2$. The $\chi^{(2)}$ tensor is a third order tensor, which has $3{\times}9 = 27$ elements. As lithium niobate is a non centro-symmetrical material of the 3m point group, some of those 27 components vanish and some of them are equal or have opposite signs. This leads to the tensor with only 3 independent components; it can be written as $d^{(2)} = \frac{1}{2}\chi^{(2)}$ [33]:

$$d^{(2)} = \begin{pmatrix} 0 & 0 & 0 & 0 & d_{31} & -d_{22} \\ -d_{22} & d_{22} & 0 & d_{31} & 0 & 0 \\ d_{31} & d_{31} & d_{33} & 0 & 0 & 0 \end{pmatrix} \tag{2.19}$$

These coefficients have been experimentally determined. They are strong frequency dependent. Using SHG processes in bulk $LiNbO_3$ $d_{31}$, $d_{33}$ [34] and $d_{22}$ [35] coefficients for different frequencies are shown in Table 2.1.

## 2.3 Quasi-Phase Matching

In any nonlinear optical process the energy and momentum conservations are automatically fulfilled. For three wave mixing processes the conditions correspondingly are:

$$\omega_p = \omega_s + \omega_i \tag{2.20}$$

$$\vec{\beta}_p = \vec{\beta}_s + \vec{\beta}_i \tag{2.21}$$

[3]Nonlinear devices, described in this work, are pumped at the wavelength around 1550 nm. High energy pump photons decay in the medium into two photons of lower energy, so called signal and idler. Here and later indices „$p$, $s$, $i$“ will be used instead of „1, 2, 3“.

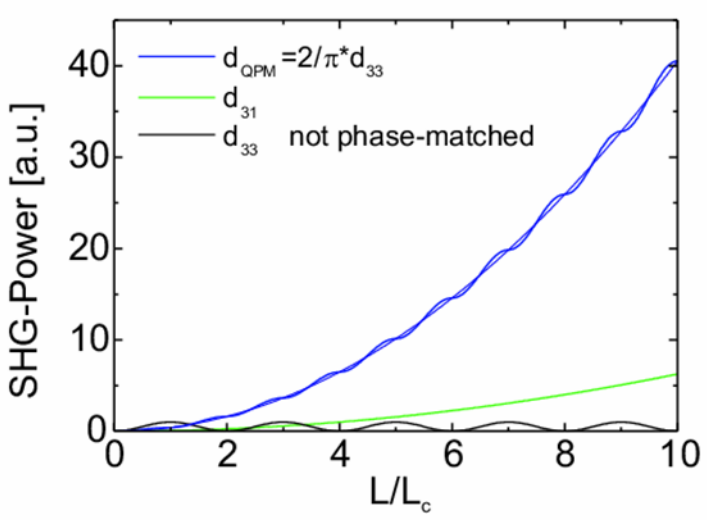


**Figure 2.3:** SHG generation over 10 periods for three different conditions: QPM case with the largest $d_{33}$ coefficient (blue); phase matching utilizing birefringence (green) and without phase matching (black).

where $\omega_j = \frac{2\pi c}{\lambda_j}$ is an angular frequency and $\vec{\beta}_j$ is the wave vector of the pump, signal or idler field, respectively.

Material dispersion leads to the different phase relation between interacting waves and that in turn - to the periodic energy transfer: energy will always flow from pump to new generated waves as long as the phase between the optical waves is less than 180 degrees. For the phase difference between them more than 180 degree - energy transfer will start in the back direction (Fig. 2.3 (black curve)). Efficiency of such process is very low.

If phase relation between the waves would be constant, then the new wave would be generated continuously along the whole interaction length. This means, that the waves should have equal phase velocity, which is defined by:

$$\upsilon_{phase} = \frac{c}{n_{eff}} \tag{2.22}$$

where $c$ is the speed of light in vacuum and $n_{eff}$ the effective index of refraction. If the wave mixing process has this condition, then the power of the generated waves will be increased continuously (Fig. 2.3 (green curve)). This condition is called the *phase matching* condition. Usually, nonlinear crystals (and $LiNbO_3$ as well) have material dispersion. Their index of refraction is frequency dependent. The true phase matching condition can be realized for two orthogonal polarizations, where the interaction takes place between ordinary and extraordinary waves or two waves of the same polarization (for example [36]) under particular angle relative to the crystal at particular temperature. $n_{eff}$ is influenced also by the mode distribution. This effect is called *mode dispersion*. All these conditions limit the tunability of the device and, as a consequence, possible area of application.

To adjust artificially the phase velocities of interacting waves and, therefore, to enlarge the tunability of such devices a following method has been applied. A quasi-phase matching (QPM) technique was proposed for the first time by Armstrong et al. [17] in 1962.

The idea to reduce the dispersion effect was to modulate periodically the nonlinear coefficient and to compensate in that way phase mismatch (Fig. 2.4). Quasi-phase-matching ensures that there is a positive energy flow from the pump frequency to signal and idler frequencies even though all the frequencies involved are not phase locked with each other. The coherence length is the length in the medium in which the phase of pump and induced polarization is less than 180 degrees from each other. At each coherence length the crystal axis is flipped, that leads to the change of sign of a nonlinear coefficient and allows the energy to continue positively to flow from the pump to signal and idler frequencies. To generate MIR radiation in the wavelength range $2 < \lambda < 4$ $\mu$m coherence length $l$ of about 15 $\mu$m is necessary.

Nowadays, this technique finds very wide application in many nonlinear devices. It allows to compensate phase velocity dispersion for the frequency conversion and the largest nonlinear coefficient of the material can be utilized. For $LiNbO_3$ utilizing the largest $d_{33}$ coefficient with waves polarization oriented parallel to the crystallographic $Z$-axis, a gain enhancement over the birefringently phase-matched process is about factor of 20 larger [35].

This technique is applicable in the whole transparency range of the material. The wavelength tuning can be adjusted by changing the temperature of the sample, wavelength of the pump or changing the grating period of modulated nonlinear coefficients. The recently developed electrical poling method is able to fabricate the domain structures even on the submicrometer scale [37].

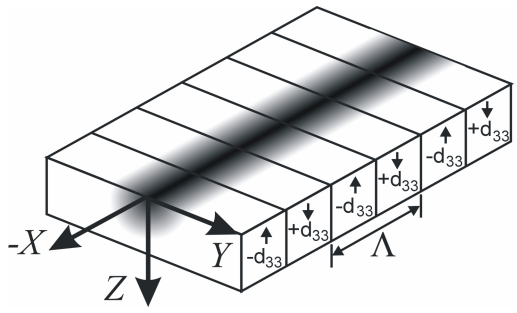


**Figure 2.4:** Periodically poled Ti:$LiNbO_3$ with crystal coordinate system

The periodically modulated nonlinear coefficient can be written in form of a Fourier series:

$$d(z) = d_{eff} \sum_{m=-\infty}^{\infty} G_m \exp(-i\beta_m z) \tag{2.23}$$

where $d_{eff}$ is an effective nonlinear coefficient, m - an order of Fourier series and $\beta_m = \frac{2\pi}{\Lambda}$ is the grating wave number with domain periodicity $\Lambda$. $G_m$ is a Fourier

coefficient, defined by

$$G_m = \frac{2}{m\pi}\sin(m\pi D). \tag{2.24}$$

$D = \frac{\Lambda}{l}$ is a duty cycle of the grating.

The effective nonlinear coefficient is largest for the 1st order Fourier series with a duty cycle 50%[4]:

$$d_{\text{eff}} = \frac{2}{\pi}d \tag{2.25}$$

The wave mismatch factor can be written in the form:

$$\Delta\beta = \beta_p - \beta_s - \beta_i - \frac{2\pi}{\Lambda} \tag{2.26}$$

An example of the advantage using QPM is presented in Fig. 2.3. Three different cases of SHG generation over 10 periods are shown [26]. QPM condition with $d_{33}$ coefficient has the highest efficiency ($d_{eff} = \frac{2}{\pi}d_{33}$). Birefringent phase matching condition in lithium niobate allows to utilize only the $d_{31}$ nonlinear coefficient, which is about 5 times smaller, than $d_{33}$. In this case fundamental wave, polarized perpendicular to the crystallographic $Z$-axis will have the same phase velocity as the SHG-wave, polarized parallel to it ($d_{eff} = d_{31}$; $n_f^o = n_{SHG}^e$). Non phase matching condition shows periodic power transfer between fundamental and generated second harmonic waves and low efficiency even by utilizing the largest nonlinear coefficient ($d_{eff} = d_{33}$).

Optical Parametric Generators (OPGs) and Oscillators (OPOs) are attractive sources of coherent radiation in comparison with conventional lasers. They are broadly tunable and applicable in the wavelength range where no laser emission is found up to now. But there are still some limitations of implementation of such devices due to conventional birefringent phase matching, walk-off, relative small nonlinear coefficients and angular tuning.

According to the relative orientation of polarizations for the mixing process, OPOs and OPGs are classified as the following: If three interacting waves have the same polarization orientation, then this is so called Type-I phase matching. If new generated waves have an orthogonal polarization, then this is Type-II phase matching condition.

In this work OPGs and OPOs of only Type-I will be discussed.

[4]These conditions are taken into account for all nonlinear interactions described in the work.

# Chapter 3

# Sample Fabrication and Characterization

## 3.1 Ti:PPLN Waveguide Fabrication

### 3.1.1 Fabrication of Straight Waveguides

The sample fabrication scheme is shown in Fig. 3.1. The waveguide fabrication starts with an indiffusion of a photolithographically defined Ti-stripe (Fig. 3.1a). To get single mode waveguides in the mid infrared Ti-stripes of 18, 20, 22 $\mu$m width and 162 nm thickness are used. The waveguides of this width will be automatically multimode for the pump radiation near 1550 nm.

Having $QTM_{00}$ spatial distribution of the excited MIR waves, $QTM_{00}$ mode of the pump wave is necessary. In this case the largest overlap and therefore the most efficient energy transfer between interacting waves would be achieved. This can be realized, for instance, by using a taper structure at the input side of the waveguide. Such a structure has been realized experimentally. The pump wave is coupled to a 7 $\mu$m wide waveguide. Here only fundamental wave propagation at the pump wavelength is allowed and higher order modes are under cutoff (see for example [13]). This automatically leads to the excitation of the fundamental mode only. Starting from 7 $\mu$m width, the waveguide is expanding to above mentioned $\sim$ 20 $\mu$m at 3 mm length[1]. Experimentally, it was found later, that a taper is not necessary to excite the fundamental mode selectively. Much more critical are the waveguide inhomogeneity itself and proper coupling (which can be controlled by using a camera and appropriate optics). Later on, taper structure has not been used nor for OPG processes nor for OPOs.

The typical steps of fabrication of the titanium indifussed waveguides in periodically poled lithium niobate will be described briefly in the following: indiffusion of titanium is performed into the -Z face at 1060 °C over 31 hours in an argon atmosphere (Fig. 3.1b); subsequently, a post diffusion follows at the same temperature in oxygen to reoxidize the material. We found that a subsequent electric field poling is not pos-

[1] See mask 'MIR-Taper'

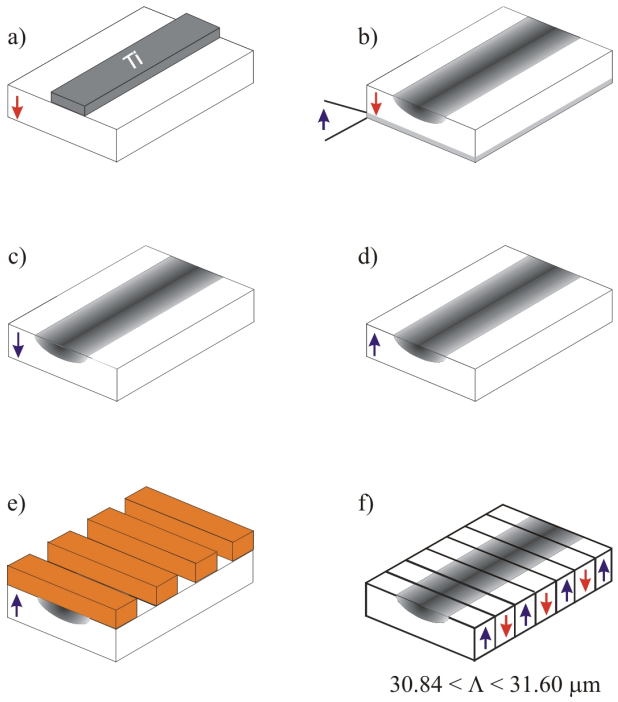


**Figure 3.1:** Fabrication of periodically poled Ti:$LiNbO_3$ waveguides

sible due to a shallow domain inverted layer on the +Z side of the sample. To obtain a single domain sample again this layer is removed by careful grinding (Fig. 3.1c). In order to get a periodic microdomain structure of excellent homogeneity a two step electric field poling technique has been developed. By a first poling step the spontaneous polarization of the whole substrate is reversed (Fig. 3.1d). In this way the waveguides come to the +Z-face preferred for periodic poling. As the growth of the microdomains always starts from the +Z-face the periodic electrodes are fabricated here on top of the waveguides (Fig. 3.1e). In this way the domains become more precisely defined in a surface layer including the waveguide. A periodic photoresist structure is formed on the sample surface and then immersed in LiCl dissolved in isopropylalcohol used as liquid electrode. Subsequently, periodic poling is accomplished by application of a high voltage to exceed the coercitive field strength of $LiNbO_3$ of about 21 kV/mm. The poling process is controlled by monitoring the current flow through the crystal. Poling is stopped, when the charge corresponds to an empirically determined value to get a 50 % duty cycle of the domain pattern (Fig. 3.1f). The total length of the periodically poled region is up to 95 mm. Finally, thermal annealing at $> 120\,°C$ over 2 hours is performed to reduce the optical losses induced by mechanical stress.

Several masks with grating structures of periodicities from 30.84 - 31.60 $\mu$m in steps of 0.08 $\mu$m have been designed. This freedom in choosing periodical poling allows to cover continuously large range of MIR radiation starting from about 2500 nm and up to about 3700 nm.

After polishing the end faces, the samples were transferred from technology to the

laboratory. Waveguides losses have to be investigated.

### 3.1.2 Fabrication of Periodically Poled Bent Waveguides

As will be shown later, the parametric gain strongly depends on the interaction length and therefore on the waveguide length. Samples used in our group are made from 4 inch wafers. And after cutting and polishing the maximum interaction length, they can have, is about 96 mm, which is much larger in comparison with bulk optics. Having longer waveguides would allow to fabricate even more efficient integrated structures.

Recent research activities in our group have shown promising results in the fabrication of bent waveguides of a length twice as large as that of straight waveguides. The whole wafer has been used for waveguide fabrication and the following profile was realized (Fig. 3.2 left): 17 waveguides are deposited parallel to each other. Every waveguide consists of a half curcuit of a "U" shape with two straight parts of 37 mm length and radius of curvature from 20 to 36 mm. The maximum overall length of the outer waveguide can be as large as 18.7 cm.

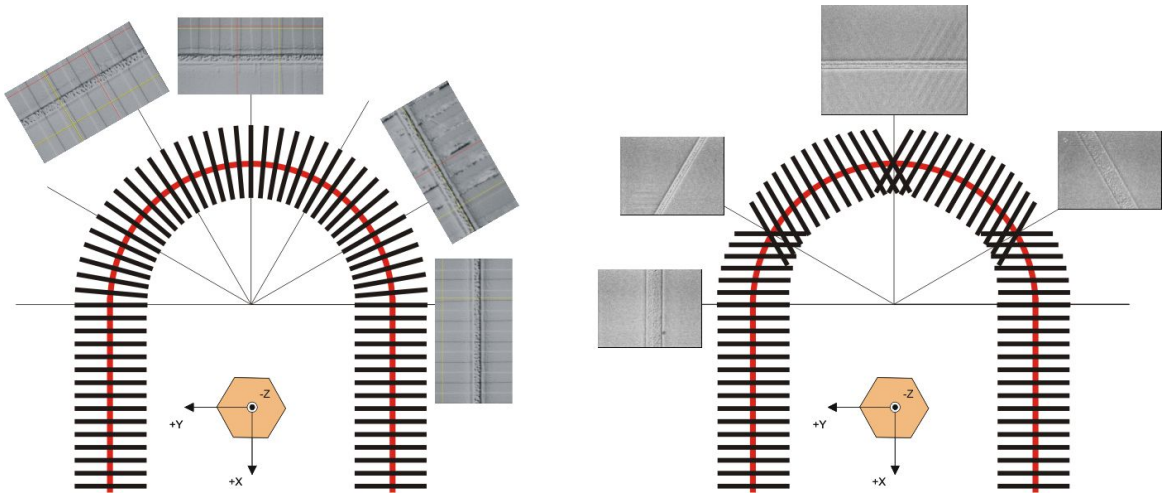


**Figure 3.2:** Schematic diagram of the waveguide and periodic poling orientation relative to the crystallographic axis: Periodic poling oriented perpendicular to the waveguide and corresponding picture after the poling as insets (left); Periodic poling oriented under angel to the waveguide parallel to the crystallographic axis and corresponding picture after the poling as insets(right).

First NIR samples were fabricated with periodic domains all the time perpendicular to the waveguide (Fig. 3.2 left). Etching afterwords (see insets) has shown burned areas near the domain walls in the bent part (Fig. 3.3 left). No poled domain through the 0.5 mm sample were found (Fig. 3.3 right). In this part of the sample only two domains are properly poled. It is clearly seen on the top as well as on the side view. Random zigzag profile of the walls on the surface do not allow to reach proper domain periodicity and therefore phase matching condition. Further work has shown, that the growth of domain with walls parallel to the crystallographic axis is preferred. Therefore, recent developments with periodical poling oriented all the time parallel to

the crystallographic axis was used for generation NIR and MIR. The correspondent domain orientation relative to the crystal is shown in Fig. 3.2 (right) with photos of etched domains of proper orientation.

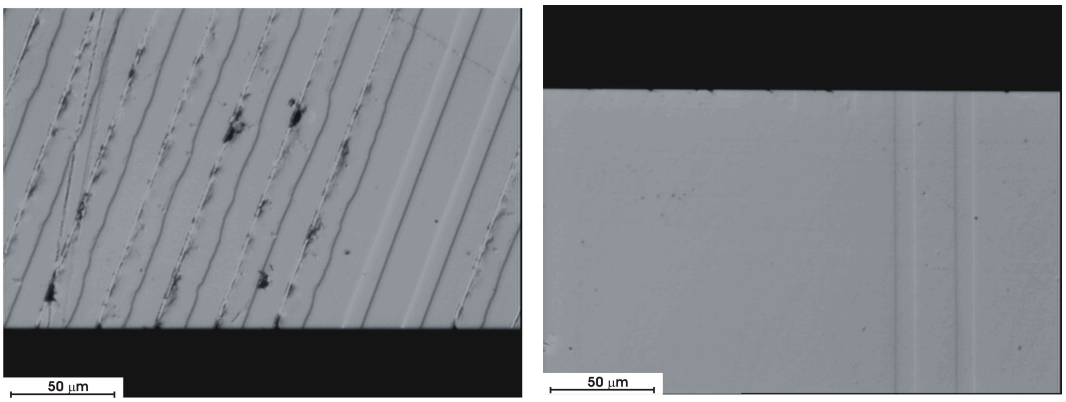


**Figure 3.3:** Top view of selectively etched domains with some burned out areas (left); Side view of the same area (right).

All the other technological steps for the fabrication of bent waveguides do not differ from the fabrication of straight guides.

## 3.2 Loss Measurements

### 3.2.1 Principle and Results for Straight Waveguides

When the sample is ready it is very important to measure the waveguides losses, which can significantly change the efficiency of parametric nonlinear devices. Low losses are not so much important for optical parametric generators, since pump and generated waves are passing the waveguide just once. However, low losses are essential for resonant devices like OPOs, where they are accumulated after each round trip time and affect a lot the Q-factor of the device.

There are several methods to measure the propagation losses of a waveguide [38–41]. Some of them are dependent on the coupling efficiency, some methods can be implemented only for pyroelectric materials etc.

An elegant method for measuring losses in low finesse Fabry-Perot cavities has been introduced for the first time by Kaminow and Stulz [42]. They used a $LiNbO_3$ cavity for the determination of waveguide losses. Regener and Sohler have elaborated this method to utilize it with Ti:$LiNbO_3$ waveguides of different cuts and lengths [43].

The method is based on measuring the intensity contrast

$$K = \frac{I_{max} - I_{min}}{I_{max} + I_{min}} \tag{3.1}$$

in low finesse Fabry-Perot cavities mainly for single mode waveguides by changing the optical path length (usually done by small changes of the sample temperature,

but wavelength tuning is also possible). Here $K$ is contrast between minimum and maximum of the transmitted signal; it is independent on beam intensity and coupling efficiency. After some transformations finally the loss coefficient in $dB/cm$ can be written as

$$\alpha \approx \frac{4.34}{L} \exp\left(\ln \frac{2R}{K}\right) \tag{3.2}$$

with $R$ is the reflectivity of the waveguide end faces; $L$ is the cavity length in $cm$. Here $\alpha$ determines the upper limit of the losses inside the cavity.

It is easy to show that the error of measuring the losses is the smaller, the lower the waveguide losses are. In other words, this method is giving a higher accuracy for low-loss waveguides.

Eq. 3.2 shows that small variations of the contrast are leading to large changes of the attenuation coefficient (Fig. 3.4).

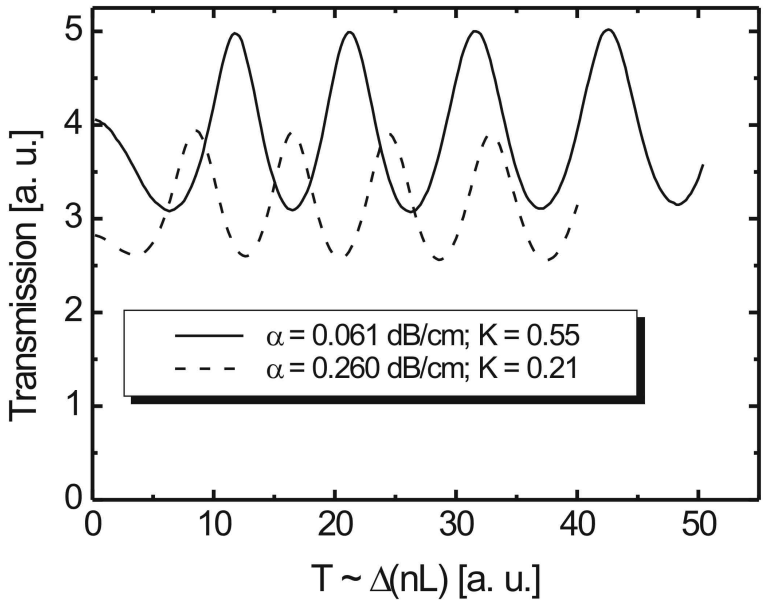


**Figure 3.4:** An example of loss measurements by changing the temperature of periodically poled Ti:$LiNbO_3$ single mode waveguide at 3394 nm for two straight waveguides of different losses: TM polarization; w = 20 $\mu$m.

As it was mentioned above, $\alpha$ is giving the upper limit for the losses. Experimentally, losses down to 0.03 dB/cm or even less for the straight waveguides of a length up to 95 mm have been measured.

Loss measurements in the MIR range have been done with a He-Ne laser at $\lambda = 3394\,\text{nm}$ with TM polarized light, which can only excite transverse $QTM_{00}$ in

the waveguide of the width about 20 $\mu$m. Excitation of higher modes at $\lambda \approx 1550\,\text{nm}$ is also possible.

Coupling losses into a waveguide can be estimated if propagation losses are known.

### 3.2.2 Results for Bent Waveguides

The same technique of loss measurements was also used for bent waveguides. The optical waveguide length was changed by heating up the sample in the range 23 - 27°C. Losses versus the radius of the curvature of the waveguides are shown in Fig. 3.5. The

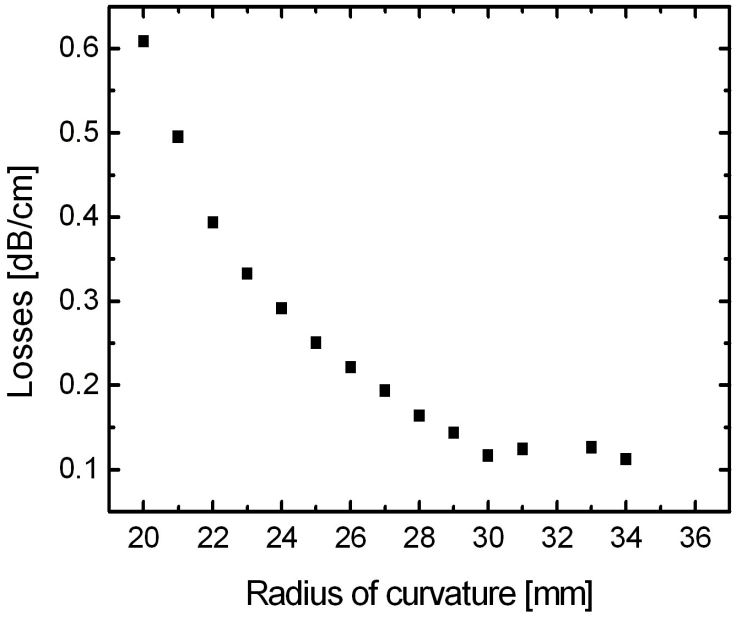


**Figure 3.5:** Losses in the bent waveguides vs. radius of curvature: $\lambda = 3394$ nm; TM polarization; w = 18 $\mu$m.

innermost waveguides have the largest damping coefficient close to 0.6 dB/cm. It becomes smaller for the outer waveguides, approaching the losses of straight waveguides at radius more than 30 mm. Fig. 3.5 shows results for the inner 15 of 17 waveguides on the whole wafer. Two outer ones could not be characterized due to some damage during the fabrication of the sample.

## 3.3 Near Field Intensity Profile

Another important method for the waveguide characterization is to measure the near field of the mode. It allows easily to check the homogeneity of the waveguide[2], qual-

[2]As the experiments show, waveguide, which are able easily to excite $\text{QTM}_{00}$, have low inhomogeneity.

itatively estimate the losses and scattering of the light into the substrate, calculate FWHM of the mode (and compare it with expected theoretical results) and predict the refractive index profile.

This technique is not only important to characterize the fabricated waveguides for some further applications, but also gives a tool to optimize the technology of fabrication allowing to improve the parameters of fabrication processes.

Such intensity distribution profiles can be measured in the near- [44, 45] and far-field [46, 47]. In practice the far-field mode is used mainly for the characterization of the optical fiber, where fully symmetrical profiles allow to simplify the mathematical background. For nonsymmetrical waveguides the near-field mode is a more simple and direct method for the characterization.

This method allows to get immediately a full picture of the intensity distribution digitized for further analysis. This technique is preferred in our laboratory and routinely used for the characterization of waveguides for near infrared application.

To get good results, the intensity profile has to be magnified with high resolution. Conventional lenses do not allow to realize both simultaneously, while small mode size (usually in the range of several $\mu$m) is lower then the optical resolution of the lens. For example, to couple out the light from the waveguide for MIR applications usually the $CaF_2$-lens is used. It has a focal length of 8.3 mm. NA in this case will be $\approx 0.38$. The optical resolution by using a He-Ne laser ($\lambda = 3394$ nm) of this lens will be:

$$\delta r = 1.22 \frac{\lambda}{NA} = 1.22 \frac{3.4}{0.38} \approx 10.9\,\mu m \tag{3.3}$$

If the same measurement would be done in the NIR-range, a resolution of more than a factor of two better might be achieved (less then 5 $\mu$m). Instead of low NA lenses microscope objectives are used in the NIR, providing high resolution and magnification simultaneously (NA = 0.9; m = 100×). The resolution in this case is 2.1 $\mu$m which is sufficient to resolve the mode profile of the fundamental waveguide mode.

Such microscope objective are very complex system of different lenses made for the applications in the visible and the near infrared range, but are not transparent for the MIR radiation and therefore cannot be used.

In the NIR above mentioned objective in combination with a CCD[3] camera successfully fulfill this task (Fig. 3.6 (a)). FWHM of the pump mode about 5.6 × 3.3 $\mu$m is measured.

There were several problems, which did not allow for a long time to implement the same type of measurements in the MIR spectral range: standard microscope objectives are not transparent at all for this wavelength range. Alternatively reflective objectives have been found on the market: their two golden coaxial mirrors are making an imaging. An advantage of this type of objective is a wavelength insensitivity[4]. It has a magnification of 74× and a NA = 0.65. Due to the design of the device, some central part of the image will be blocked[5]. According to our tests with this objective, no good

[3]CCD - **C**oupled **C**harge **D**evice

[4]Golden mirrors allow to reflect the light in the large spectral range

[5]Obscuration of 13.3 % was specified

transmission of the MIR radiation, coupled out of the waveguide was observed. The whole waveguide illumination is mainly blocked by the first mirror and the objective could not be used for this application.

Second main problem was a sensitive camera for the MIR range, which may properly work with a coherent radiation. Two cameras have been tested in our laboratory. One, kindly borrowed from Heinz Nixdorf Institut, could not show any good results due to window in front of the sensitive elements, which worked as a good Fabry-Perot filter, generating patterned image. Incoherent sources, like EDFAs without any pump can eliminate this problem and, therefore, are ideal candidates used to illuminate the waveguide near 1550 nm. For MIR only coherent laser source at $\lambda = 3394$ nm is available in our laboratory. The other MIR camera, consisting of InSb detector array ($320 \times 256$ pixels), could provide good image quality even for the coherent radiation and might be implemented for NIR as well as for MIR radiation (extended camera range 1 - 5 $\mu$m).

Alternatively two types of ZnSe meniscus lenses (focal length 10 and 20 mm) have been used to image the near field intensity profile on the camera array. Using a meniscus lens, specially designed for the wavelength $\lambda = 3394$ nm allows to avoid the spherical aberrations.

Measured intensity profile in the waveguide of the width w = 20 $\mu$m is shown in Fig. 3.6 (c). Correspondent FWHM of the MIR mode are about $12.0 \times 9.2$ $\mu$m. Theoretical calculations (Fig. 3.6 (b)) predicts a bit larger mode profile in the transverse direction of about 14 $\mu$m. Therefore good agreement between calculated and measured results lies in the confidence interval.

The mode profile measurements have been presented for the first time in the MIR spectral range and can also be routinely used to characterize the waveguides.

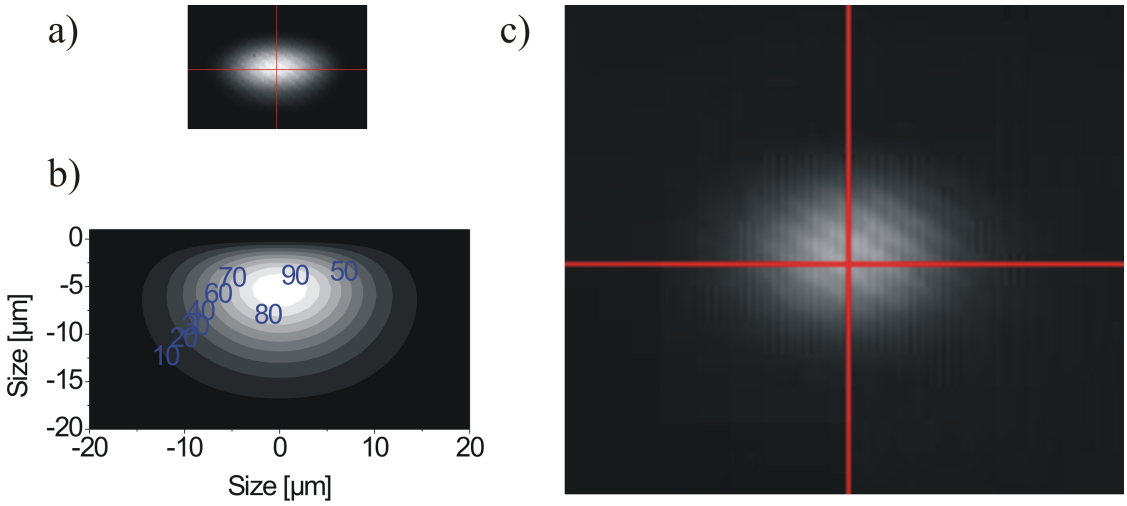


**Figure 3.6:** Measured intensity profile for the pump wavelength at $\lambda = 1550$ nm in the MIR waveguide (a); calculated at $\lambda = 3000$ nm (b) and measured (c) intensity profiles at $\lambda = 3394$ nm: w = 20 $\mu$m; f = 10 mm.

# Chapter 4

# Optical Parametric Generators

## 4.1 Theoretical Background

The term Optical Parametric Generation (OPG) means a spontaneous or stimulated decay of a pump photon into two photons of different frequencies ($\omega_s \neq \omega_i$; nondegenerated case) or the same frequencies ($\omega_s = \omega_i = \omega = \frac{\omega_p}{2}$; in degeneracy point), which is defined by power and momentum conservation (see Eq. 2.20-2.21). This process can be described semi-classically, where one pump photon decays and signal and idler are generated from vacuum fluctuation of the electromagnetic field and amplified according to the gain.

First reports of OPG can be found in [48]. Using an argon laser at 488 nm as a pump, tunable in the range from 540 - 660 nm OPG in bulk $LiNbO_3$ was observed. Generated power of several pW was reported. First experiments using Ti:indiffused waveguides in $LiNbO_3$ have been reported in [49, 50].

Solving Maxwell's equation (Eq. 2.10) and taking into account terms for nonlinear polarization (Eq. 2.17) under the assumption of a slowly varying amplitude and neglecting the pump deplection the system of coupled mode equations will look as [26]:

$$\begin{aligned}
\frac{\partial A_p}{\partial z} &= -\alpha_p A_p + i\frac{d_{eff}\tilde{\kappa}}{c}\frac{\omega_p}{n_p}A_s A_i \exp\left(-i\Delta\beta z\right) \\
\frac{\partial A_s}{\partial z} &= -\alpha_s A_s + i\frac{d_{eff}\tilde{\kappa}}{c}\frac{\omega_s}{n_s}A_p A_i^* \exp\left(+i\Delta\beta z\right) \\
\frac{\partial A_i}{\partial z} &= -\alpha_i A_i + i\frac{d_{eff}\tilde{\kappa}}{c}\frac{\omega_i}{n_i}A_p A_s^* \exp\left(+i\Delta\beta z\right)
\end{aligned} \tag{4.1}$$

with

$$\Delta\beta = \beta_p - \beta_s - \beta_i$$

$$\tilde{\kappa} = \int_0^\infty \int_{-\infty}^\infty E_p(x,y)E_s(x,y)E_i(x,y)dxdy$$

$$1 = \int_0^\infty \int_{-\infty}^\infty E_j^2(x,y)dxdy, \quad j = p,s,i$$

Here $\alpha_j$ are waveguide loss coefficients for pump, signal and idler amplitudes, respectively; $d_{eff}$ is an effective nonlinear coefficient, determined by the sample orientation and polarization of the interacting waves (Eq.2.19), $\tilde{\kappa}$ is the normalized overlap integral of the field distributions of all three waves involved in the interaction, having dimensions [$m^{-1}$]; $c$ is speed of light in vacuum.

Usually such equations do not have any analytical solution and have to be solved numerically using for example the above mentioned FEM [27] or be approximated by the GHG [51] function.

Signal and idler power depend very strongly on the pump power. Neglecting any pump depletion, the evolution of the pump power can be written as:

$$P_p(L) = P_{p,0} e^{-2\alpha_p L} \tag{4.2}$$

For the *phase-matched* case, i. e. $\Delta\beta = 0$, the set of equations (4.1) can be solved by integration over the length and leads to:

$$\begin{aligned} P_s(L) = e^{-2\alpha L} \Bigg[ & P_{s,0} \cosh^2 G(L) + \frac{\omega_s}{\omega_i} P_{i,0} \sinh^2 G(L) \\ & -2\sqrt{\frac{\omega_s}{\omega_i} P_{s,0} P_{i,0}} \sinh G(L) \cdot \cosh G(L) \cdot \sin(\phi_s + \phi_i) \Bigg] \\ P_i(L) = e^{-2\alpha L} \Bigg[ & P_{i,0} \cosh^2 G(L) + \frac{\omega_i}{\omega_s} P_{s,0} \sinh^2 G(L) \\ & -2\sqrt{\frac{\omega_i}{\omega_s} P_{s,0} P_{i,0}} \sinh G(L) \cdot \cosh G(L) \cdot \sin(\phi_s + \phi_i) \Bigg] \end{aligned} \tag{4.3}$$

with the gain function for the phase matched interaction

$$G(L) = \frac{g}{\alpha_p}(1 - e^{-\alpha_p L}) \tag{4.4}$$

and the gain constant

$$g = d_{eff} \epsilon_0 \tilde{\kappa} \sqrt{\frac{2}{(\epsilon_0 c)^3} \frac{\omega_s \omega_i}{n_p n_s n_i} P_{p,0}} \tag{4.5}$$

$\omega_s$ and $\omega_i$ are the angular frequencies for the ideal phase matching; $P_{s,0}$ and $P_{i,0}$ the signal and idler input power levels and $\phi_s$ and $\phi_i$ are the phase of signal and idler constants respectively.

For a *phase-mismatched* interaction ($\Delta\beta \neq 0$) Eq.4.1 does not have any analytical solution and has to be solved numerically. Nevertheless, an analytical solution can be found if we assume no losses for the pump ($\alpha_p = 0$). Of course, it does not describe

the real situation, but any way allows to see the behavior of the nonlinear interaction:

$$P_s(L) = e^{-2\alpha L}\left[P_{s,0}\left\{\cosh^2(\Gamma L) + \left(\frac{\Delta\beta}{2\Gamma}\right)^2 \sinh^2(\Gamma L)\right\} + \frac{\omega_s}{\omega_i}\left(\frac{g}{\Gamma}\right)^2 P_{i,0}\sinh^2(\Gamma L) - 2\frac{g}{\Gamma}\sqrt{\frac{\omega_s}{\omega_i}P_{s,0}P_{i,0}}\sinh(\Gamma L)\cdot \left\{\cosh(\Gamma L)\sin(\phi_s+\phi_i) + \frac{\Delta\beta}{2\Gamma}\sinh(\Gamma L)\cos(\phi_s+\phi_i)\right\}\right] \tag{4.6}$$

$$P_i(L) = e^{-2\alpha L}\left[P_{i,0}\left\{\cosh^2(\Gamma L) + \left(\frac{\Delta\beta}{2\Gamma}\right)^2 \sinh^2(\Gamma L)\right\} + \frac{\omega_i}{\omega_s}\left(\frac{g}{\Gamma}\right)^2 P_{s,0}\sinh^2(\Gamma L) - 2\frac{g}{\Gamma}\sqrt{\frac{\omega_s}{\omega_i}P_{s,0}P_{i,0}}\sinh(\Gamma L)\cdot \left\{\cosh(\Gamma L)\sin(\phi_s+\phi_i) + \frac{\Delta\beta}{2\Gamma}\sinh(\Gamma L)\cos(\phi_s+\phi_i)\right\}\right]$$

with a gain factor $\Gamma$ defined as

$$\Gamma^2 = g^2 - \left(\frac{\Delta\beta}{2}\right)^2 \tag{4.7}$$

The phase terms $\phi_s$ and $\phi_i$ are not fixed to the pump and an argument $\cos(\phi_s+\phi_i)$ and $\sin(\phi_s+\phi_i)$ can be canceled by averaging, what simplify these equations.

In both equations (4.3 and 4.6) are existing terms $P_{s,0}$ and $P_{i,0}$, which mean an input power level of signal and idler waves. But for OPGs there is no input of those two waves and only power of the pump is not equal to zero. Signal and idler are growing from the quantum fluctuations. Considering very high pump photon rate in compare with the rate of generated signal and idler photons and semi-classical description, it will be sufficient to „inject“„one photon per mode“ of the signal or idler. The equations for the output MIR radiations are mathematically symmetrical for both waves; therefore it make sense to solve 4.3 and 4.6 just for one wave, for instance, signal.

Taking into account only an interaction between fundamental modes, the „injected“ idler power in the frequency interval $[\omega_i + d\omega_i]$ can be written as

$$dP_{i,0} = 1 \times \hbar\omega_i \times \frac{d\omega_i}{2\pi} \tag{4.8}$$

For $P_{s,0} = 0$ equation 4.6 will be

$$P_s(L) = e^{-2\alpha L}\left(\frac{g}{\Gamma}\right)^2 \frac{\omega_s}{\omega_i} dP_{i,0}\sinh^2(\Gamma L) \tag{4.9}$$

In the case if the gain constant is low, i. e. $g^2 \ll \Delta\beta/2$, then $\Gamma$ became equal to $i\sqrt{(\Delta\beta/2)^2 - g^2}$ and Eq. 4.9 may be written as

$$P_s(L) = e^{-2\alpha L} g^2 L^2 \frac{\omega_s}{\omega_i} dP_{i,0} \cdot \mathrm{sinc}^2\left(\sqrt{\left(\frac{\Delta\beta}{2}\right)^2 - g^2}L\right) \tag{4.10}$$

Now combining 4.8 and 4.10 and integrating over all idler frequencies we get

$$P_s(L) = e^{-2\alpha L}\frac{\hbar\omega_s}{2\pi}g^2L^2\int_{-\infty}^{+\infty}\mathrm{sinc}^2\left[\sqrt{\left(\frac{\Delta\beta}{2}\right)^2 - g^2}L\right]d\omega_i \tag{4.11}$$

After integration and taking into account, that $g^2 \ll \Delta\beta/2$ is obtained on the almost whole integration range, except phase matching, where $\Delta\beta \approx 0$, which does not have significant influence on the Eq. (4.11). This inequality can be implemented only for low gain, that means, for parametric fluorescence, where this is still a spontaneous process and $g$ is relative low. Including pump losses in the waveguide (see Eq.(4.4)) and solving Eq. (4.11) finally

$$P_s(L) = e^{-2\alpha L}\hbar\omega_{s,0}\frac{c}{|b|}\left(\frac{1-e^{-\alpha_p L}}{\alpha_p L}\right)^2 g^2 L \tag{4.12}$$

where

$$|b| = \frac{2\pi c}{\Delta\omega_s L} \tag{4.13}$$

with signal linewidth $\Delta\omega_s$ (see Eq. 4.15).

## 4.2 Experimental Setup

To investigate spectral and power properties of Ti:indiffused periodically poled lithium niobate waveguides for the generation of the MIR radiation the following setup has been built up (Fig. 4.1). A schematic diagram of a typical experimental layout is presented in Fig. 4.2.

As pump different lasers can be used. External Cavity Lasers (ECL) for C- and L - bands[1] allow to tune the pump in the range 1520 - 1620 nm. They emit up to 5 mW output power in a cw-mode of operation and have a linewidth about 100 kHz. The advantage of high output power stability and no mode hopping made these laser preferable. The L-band laser was used for longer wavelengths in combination with a L-band amplifier, which consists of polarization maintaining fibers. In this case the polarization does not have to be adjusted between them and changing of the pump wavelength does not have any influence on the output polarization state of the amplifier.

A Distributed FeedBack (DFB) laser ($\lambda$=1552 nm) in combination with a lithium niobate intensity modulator has been used for the generation of nanosecond pulses (see section „Experimantal results“).

To produce pulses of high peak power levels a Mode Locked Fiber Laser (MLL) has been used. It can be tuned in the range 1541 - 1565 nm and emits 6.4 psec pulses with an adjustable repetition rate near 10 GHz, emitting up to 20 mW average power.

[1] **C-band** - Wavelength in the range 1530 - 1565 nm; **L-band** - in the range 1565 - 1625 nm [52].

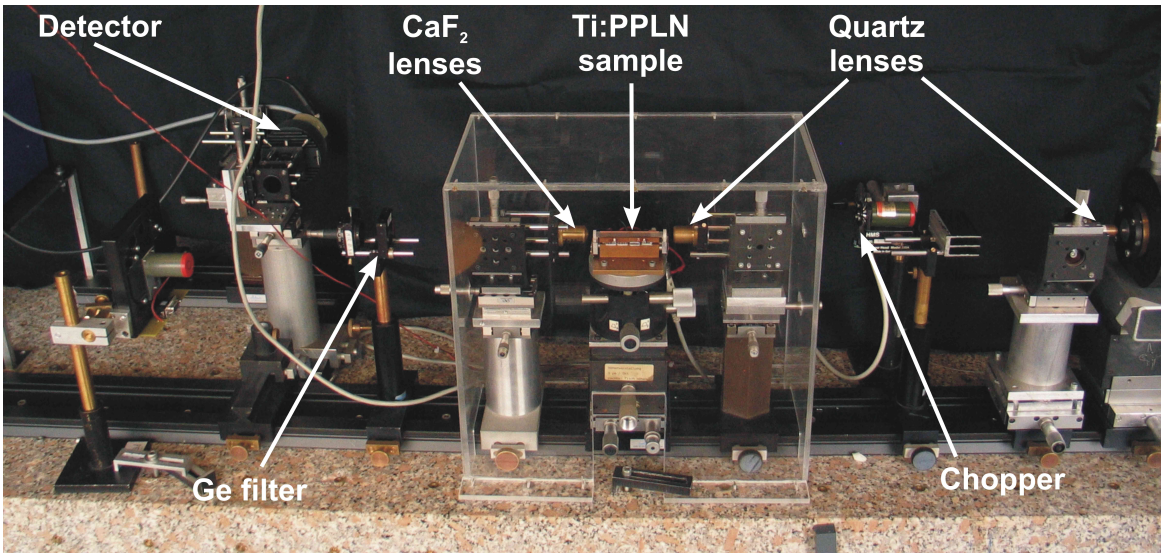


**Figure 4.1:** A photograph of the experimental setup to investigate OPGs.

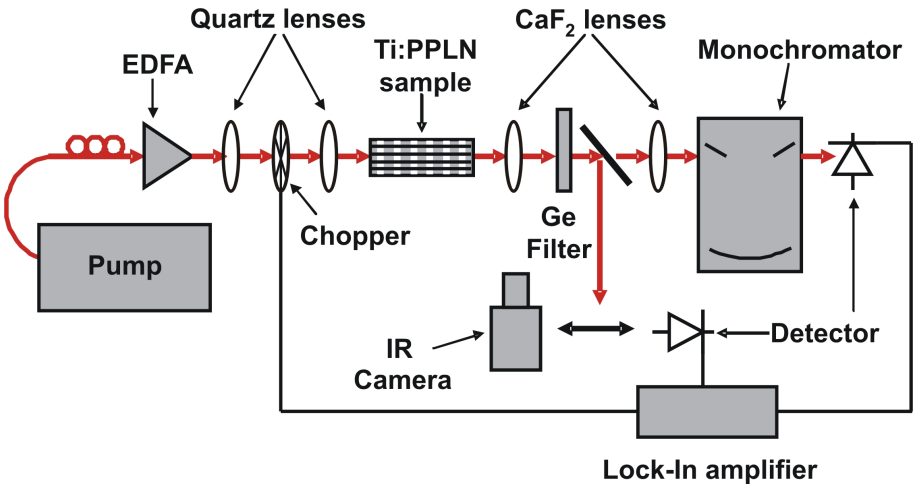


**Figure 4.2:** Schematical diagramm of the experimental setup.

For high power experiment a femtosecond laser in combination with femtosecond amplifier was taken. It could produce pulses of about 1 psec length at 80 MHz repetition rate leading to the peak power level of several hundred Watt.

The polarization controller was used to adjust the TM polarization of the pump radiation to exploit the strongest nonlinear coefficient $d_{33}$ of lithium niobate.

The pump wave was amplified in an Erbium Doped Fiber Amplifiers (EDFA) to get an average output power up to 1.5 W. In a case of the femtosecond laser a femtosecond EDFA has been used with the maximum output average power of 100 mW. Different amplifiers for C- and L-bands were used. Coupling of the pump was realized mainly via free space optics, using quartz lenses. Behind the sample $CaF_2$ lenses were taken due to absorption of quartz in the MIR. The generated signal and idler radiations were measured with a HgCdTe IR detector. With its sensitivity peak at 4 $\mu$m this detector has a good signal-to-noise ratio. The resulting electrical signals were amplified by a lock-in amplifier. For this purpose a mechanical chopper was inserted in the pump beam. A Germanium filter aligned under the Brewster angle or perpendicular to the incident beam with an AR coating for the MIR radiation was used to reflect and absorb unused pump radiation. MIR spectra were taken using a grating monochromator with a grating of 4 $\mu$m blade wavelength and 300 lines/mm.

## 4.3 Tuning Characteristics

One big advantage of quasi-phasematching is that the output wavelength is mainly defined by the periodic poling and the temperature of the nonlinear crystal. Of course, this wavelength has to be in the transparency range of the material, which for LN is from about 400 nm to 4 $\mu$m.

A measured tuning characteristics for the sample Pb403z[2] is shown in Fig. 4.3. The waveguide is 20 $\mu$m wide and 94.4 cm long. The operation temperature is 34.5 °C; domain periodicity - 31.44 $\mu$m; losses - 0.131 dB/cm. The incident pump power, measured in front of the focussing lens, was between 800 and 900 mW.

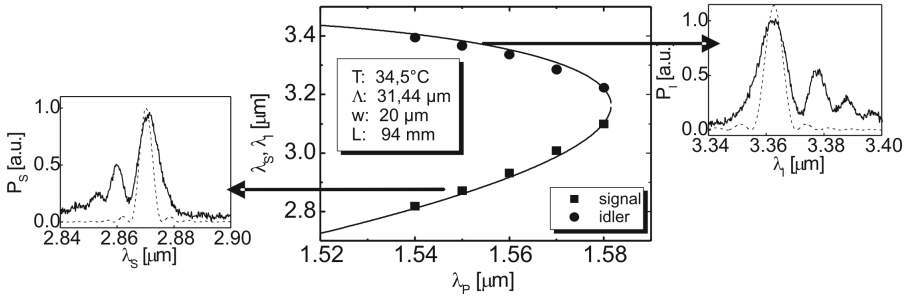


**Figure 4.3:** Measured and calculated tuning characteristics of OPF as signal and idler wavelengths versus the pump wavelength in cw-operation (middle diagram) and signal (left graph) and idler (right graph) spectra for the pump wavelength 1548.5 nm as an example.

[2]Internal numeration of samples in AG Sohler. Here "z" means Z-cut sample.

The MIR tuning range extends from 2819 nm to 3394 nm by changing the pump wavelength in the range 1540 - 1580 nm. A calculated tuning curve has an excellent agreement with the measured results.

An example of measured spectra of signal and idler are shown on the left and right sides for the pump wavelength 1548.5 nm. The dotted line shows the modelling results for the spectral response calculated with the same parameters. The experimental result differs from the theoretical "$\mathrm{sinc}^2(\Delta\beta L)$-function" by additional peaks on the short (long) wavelength side of the signal (idler) spectra. They can be explained by an inhomogeneous waveguide profile. To prove it another sample holder with independent 3-zone heating was taken and spectra were measured for different temperature profiles. By on-line monitoring of the signal (or idler) spectrum it was possible to set the temperature gradient in such way, that additional asymmetrical peak were reduced or vanished.

The FWHM for these examples was 8 nm for the signal wave and 12 nm for the idler wave, which is slightly broadener as the calculation predicts. This can also be due to an inhomogeneous structure of the waveguide. Theoretically, the FWHM can be found from Eq. 4.11 by defining [26, 53]:

$$\mathrm{sinc}^2\left(\sqrt{\left(\frac{\Delta\beta}{2}\right)^2 - G^2}L\right) = \frac{1}{2} \tag{4.14}$$

Due to energy conservation, the linewidth of the signal should be equal to the linewidth of the idler, and finally:

$$\Delta\omega_s = \Delta\omega_i = \frac{2\pi c}{L(n_i - n_s + \omega_i(\partial n_i/\partial\omega) - \omega_s(\partial n_s/\partial\omega)} \tag{4.15}$$

The tuning curve can be shifted to the left as a whole by increasing the domain periodicity. The same happens if larger waveguides or higher temperatures are used.

## 4.4 Power Characteristics

The power characteristics of OPG can be split into two parts:

- *Spontaneous Process*, where the generated MIR radiation is proportional to the pump power;
- *Stimulated Process*, where the generated MIR radiation grows exponentially with the pump power; the depletion of the pump cannot be neglected any more. This happens at relative high power levels and depends strongly on the sample length and pump power.

A comparison between cw and pulsed pump laser shows spontaneous and beginning of stimulated parametric generation (Fig. 4.4).

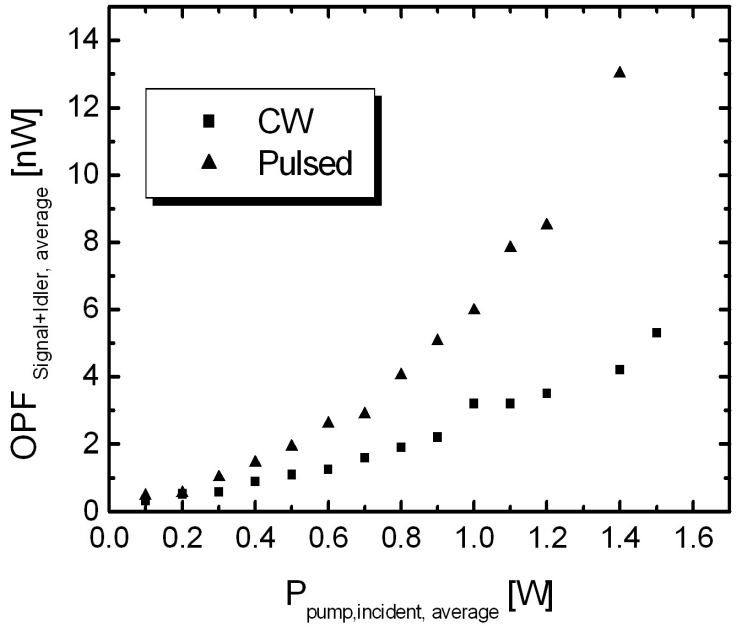


**Figure 4.4:** Total OPF power versus incident pump power for two different lasers: cw and pulsed MLL (pulse length 6.4 psec; repetition rate 10 GHz). Other parameters: $\lambda_{pump} = 1550$ nm; sample length - 94 mm; waveguide width 20 $\mu$m; $\Lambda = 31.28$ $\mu$m.

Here almost a linear dependence with a slight curvature of the MIR power versus pump power for the cw-regime is clearly observed. In the pulsed mode of operation with the same average pump power level higher fluorescence power has been measured. Due to the higher power levels in the pulse of about 15.6 times (1/[Rep. rate $\times$ pulse length]) stimulated behavior is easily to achieve.

OPGs are good sources of tunable infrared radiation for the spectroscopic application. They are single-path devices without any complicated cavity mirrors and sensitive adjustments of its components. It makes their using much easy. Their few $\mu$W of generated MIR radiation will be already sufficient for some spectroscopic application. It makes using of OPGs as very attractive devices.

For this purpose another approach of achieving higher power levels was implemented and is discussed in details in the next section.

## 4.5 Stimulated OPG Using Nanosecond Pump Pulses

### 4.5.1 Experimental Setup

A schematic diagram of the experimental setup for the generation and investigation of nanosecond MIR-pulses is shown in Fig 4.5. As laser source a semiconductor distributed feedback laser (DFB) at 1552.7 nm was used emitting up to 6 mW output

power in cw-operation. A commercial lithium niobate Mach-Zehnder modulator in combination with a pulse generator were used to generate pulses of 25, 50, and 100 ns duration from cw light with a repetition rate of 1 MHz. The polarization controllers P1 and P2 were used to adjust the proper polarization for the MZ modulator utilizing the largest $d_{33}$ nonlinear coefficient of lithium niobate. The generated pulses were amplified in two steps. The reason of choosing a preamplifier is that the standard EDFAs we have in the laboratory are used only for cw applications. Due to the relatively low saturation level at the input of an EDFA spontaneous emission will be also amplified and the signal to noise ratio will be worse. Therefore, a preamplifier was used. In this configuration average power levels of 1.5 W behind the EDFA were achieved. Launching of the light into the waveguide was done via fiber butt coupling. $CaF_2$ lenses of 8.3 and 16 mm focal length, which are transparent in the MIR, were used for collimating and focusing the beam on the InSb detector. The MIR power has been measured by using the loch-in technique: the MIR signal has been chopped and together with a reference signal sent to the lock-in amplifier. To block the pump a dichroic mirror „M“ was introduced: it has a reflectivity of 80% for the pump radiation. The rest of the transmitted pump radiation was absorbed in the germanium filter „F“.

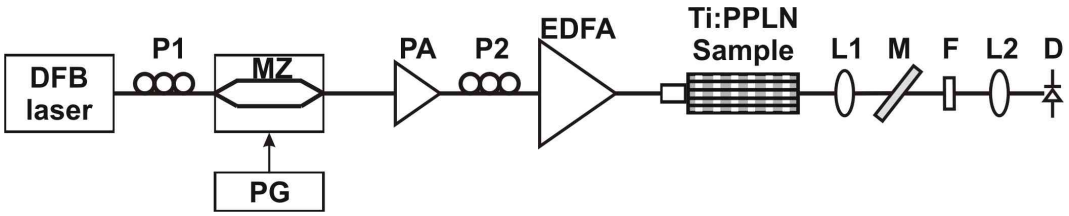


**Figure 4.5:** Experimental setup for the investigation of nanosecond OPGs: P1, P2 - Polarization controller; MZ - Mach-Zehnder integrated optical modulator; PG - radio frequency Pulse Generator; PA - Erbium doped fiber PreAmplifier; EDFA - Erbium doped fiber power amplifier; L1, L2 - $CaF_2$ Lenses; M - high reflection Mirror at 1552 nm; F - germanium Filter; D - detector (InSb).

This scheme should allow to reach peak power levels up to 60 W with 25 ns pulses[3] according to the corresponding duty cycles. This concept worked reasonablly and 25 ns pulses of up to 10 W peak power could be coupled to the PPLN waveguide.

### 4.5.2 Results

Measured and calculated data of the total OPF power (signal and ilder) are shown in Fig. 4.6a. The left diagram shows the total averaged OPF power (signal and idler measured together with one detector) for different pulse lengths and the same repetition rate as a function of the coupled pump power using the DFB-Laser as pump source ($\lambda_p = 1552$ nm, $\lambda_s = 2850$ nm, $\lambda_i = 3400$ nm). The transition to a strong exponential rise (corresponding to high parametric amplification) at high pump power

[3]Peak power calculations are based on the ratio $P_{peak} = P_{average} * T/\tau$ where $T$ is the time between two neighbouring pulses and $\tau$ is the pulse width.

levels for different duty cycles can be clearly observed. The shorter the pulses are and the higher the peak power of the pump is the early starts the transition to the stimulated process. A comparison with the cw results clearly shows, that if the same average power level is used then lower efficiency of the process under the same other parameter can be achieved. Fit functions are used to show an exponential rise of experiments with different duty cycles.

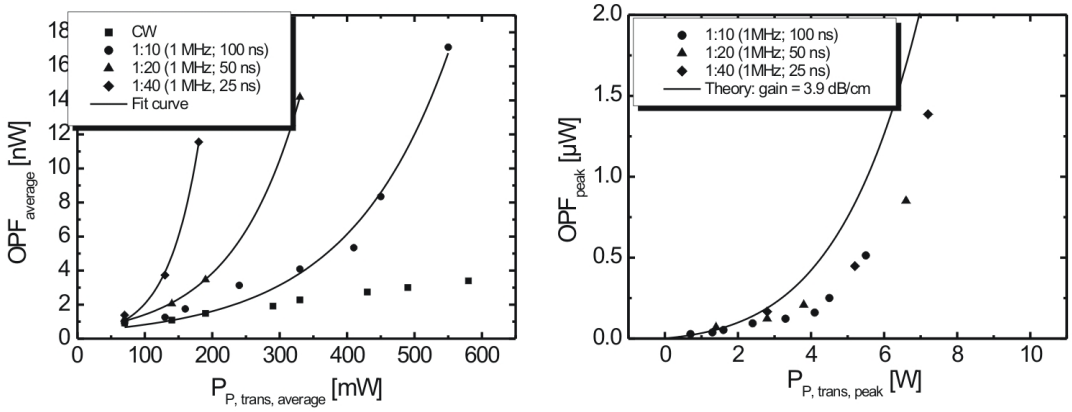


**Figure 4.6:** a) Average total OPF power (signal + idler) versus average transmitted pump power for different duty cycles compared with cw-result; b) Total OPF output peak power versus coupled pump power in a pulsed mode of operation for different pulse width (dots) compared with a theoretical calculation (solid line). Parameters: DFB laser, 1 MHz repetition rate, $\lambda_p$=1552 nm; $\lambda_s$ = 2850 nm, $\lambda_i$ = 3400 nm.

Fig. 4.6(b) shows the peak power characteristics. Calculation of the peak power levels was done by assuming that the duty cycle of MIR pulses is equal to that of the pump pulses. As expected, higher pump peak power level leads to the increase of the generated MIR power. The theoretical response, which has been calculated without any fit parameter, predicts an even higher efficiency [54]. As only the fraction of the pump power, which is coupled to the fundamental mode, is responsible for phase matched OPG an even better agreement of experiment and theory can be expected by improving the mode selective coupling.

However, an improvement of the output power level by three orders of magnitude in comparison with the cw-regime was achieved, where MIR output power level of only several nW has been observed by pumping in the watt range.

## 4.6 Generation of High Power Pump Pulses

### 4.6.1 Experimental Setup

The previous results with nanosecond pulses have shown a large potential to achieve higher OPF peak power levels in the MIR without complicated cavities as for an OPO.

Using the same technique, as described in chapter 4.5 but wih a MLL laser instead of a DFB laser should increase the peak power levels and, therefore, an even higher efficiency can be expected. A schematic diagram of the setup with the MLL as a pump is shown in Fig. 4.7.

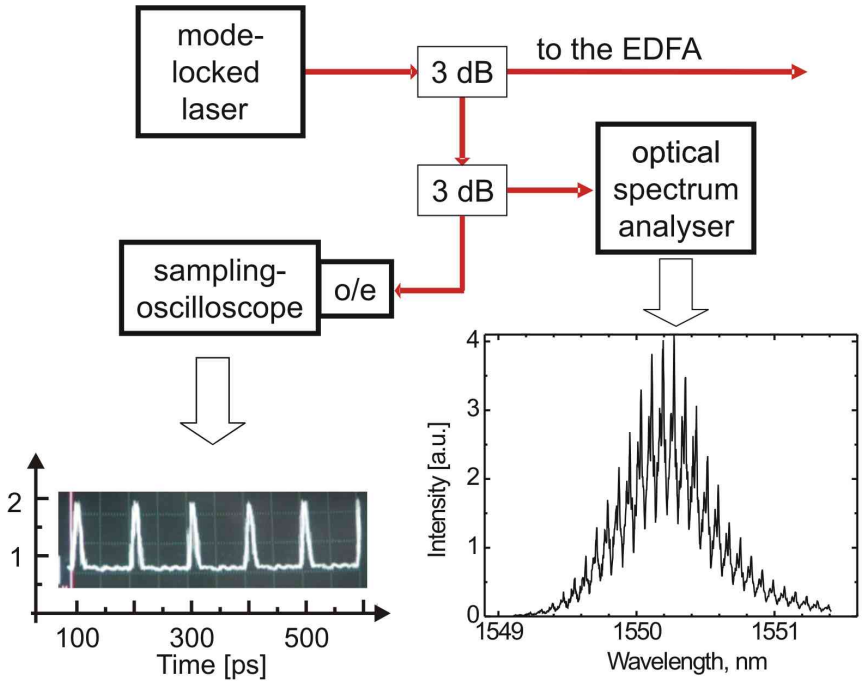


**Figure 4.7:** Schematic diagram of the experimental setup with the Mode Locked Laser as a pump.

As a laser source the MLL has been used (repetition rate - 10 GHz, pulse width - 6.4 ps). It was operated by high frequency generator, which is able to contiunously generate signals in the range 10 kHz - 5 GHz. One part of the optical signal was coupled to the optical spectrum analyzer to control the spectral properties; the other via 50 GHz fast photo detector to the communication spectrum analyzer to control the pulse train in the time domain (see Fig. 4.7).

The experimental setup for slicing the pulses is presented in Fig. 4.8. The MLL was producing pulses of about 10 GHz repetition rate and 6.4 ps length. A polarization controller is used to set the proper polarization in front of the Mach-Zehnder modulator, which was controlled by a pulse generator and it was adjusted in such way, that only every 2nd, 4th, 8th etc. pulse pass through. As an example the time domain slicing of every 16th pulse is shown in the Fig. 4.8. EDFAs, which are mainly used and designed for cw-mode, could not provide in this configuration sufficient amplification without ASE. Preamplifier in this case was necessary to amplify the sliced pulses and, therefore, saturate the buster amplifier.This setup should allow to achieve peak power levels up to 720 W according to the duty cycle by having the same average power level.

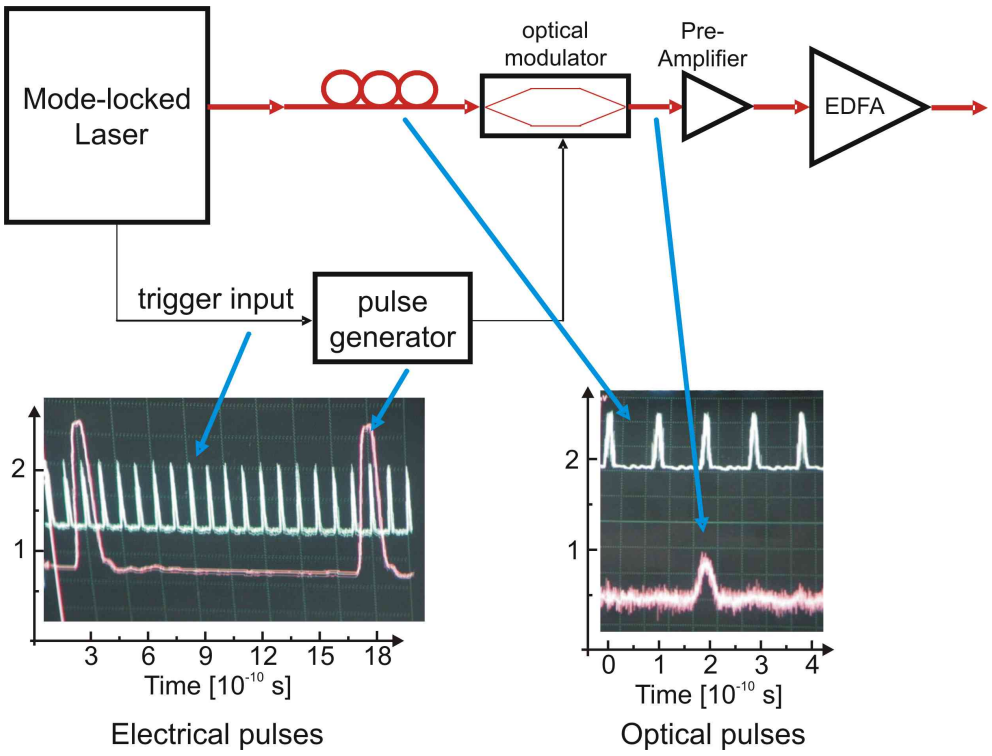


**Figure 4.8:** Experimental setup for the slicing of pulses from the MML

### 4.6.2 Results and Discussions

The power characteristics for different duty cycles has been measured. Experimental results are shown in Fig. 4.9. The pulse generator was set to pass every 8th, 16th and 32nd pulse. The average MIR power versus the average pump power has been plotted in Fig. 4.9 (left). Some MIR power fluctuations for high pump power levels were observed. It indicates that a photorefractive effects may be presented. They may reduced by increasing the sample temperature to 150 - 200 °C. In this case more complicated temperature stabilization is necessary. Additionally green luminescence at the high power levels has been seen. Measured spectra have shown the peak at 514 nm, which may come from the SFG[4].

Transition to the exponential rise at high pump power levels (stimulated OPG) depending on the duty cycle was clearly observed. Average power levels of a few $\mu$W have been achieved.

The peak power characteristics was calculated from the characteristics for the average power level according to the duty cycle of the mode lock laser and the frequency of the function generator assuming no pulse broadening of MIR pulses due to dispersion (details will be discussed in chapter 5.4). The peak power characteristics is presented in Fig. 4.9 (right). Here is clearly observed, that measured results for the different

[4]Sum frequency generation between the nonphasematched SHG generation of the pump with the pump itself.

duty cycles are not following the same curve according to Eq. 4.12: experiments with the different duty cycles, but the same peak pump power have different levels of the generated MIR power. One possible reason may be an incorrectly calculated peak power, which was calculated according to the duty cycle of the pump pulses. This may be considered only in case, when no pump pulse transformations and no MIR pulse broadening or narrowing happen due to the dispersion. To prove it an autocorrelator is necessary to investigate the MIR pulses in the time domain. The MIR autocorrelator, which would provide us with an information and is available in the laboratory, does not have a sufficient efficiency to resolve nW or $\mu$W pulses. Therefore, at the moment only theoretical calculations may predict pulse shape broadening at this wavelength (see chapter 5.4). High speed detectors and a near infrared autocorrelator (available in the laboratory) allow to have a full information about the pump pulses.

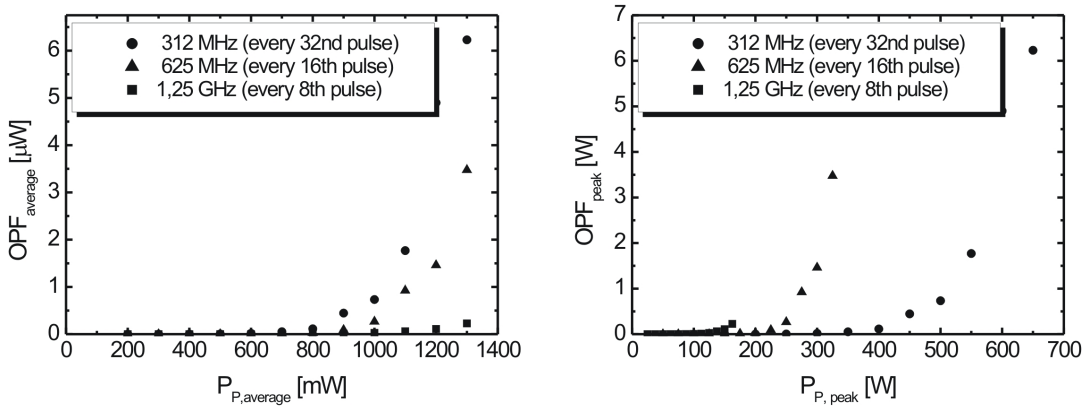


**Figure 4.9:** Power characteristics as average MIR-OPF for different duty cycles of the pump pulses versus average pump power (left); peak OPF power versus peak pump power for different duty cycle of the pump (right). Parameters: T=30 ℃; $\Lambda$=31.28 $\mu$m; $\lambda_p$=1550 nm; w=20 $\mu$m.

On the other hand, as mentioned, it is possible to investigate the pump pulses after any element in the experimental setup (Fig. 4.10). Pulses of about 6.4 ps length and 0.7 nm spectral width are generated by the MLL. Corresponding results in time and frequency domain are shown as inset. The same has been done behind the Mach-Zehnder modulator. In the time domain the pulse broadening is observed, but this is only due to the slow detector, which was used for the measurements. But in the frequency domain the pulse envelope differs from that measured in front of the modulator. Spectra of attenuated pulses were also measured behind the pre- and main amplifiers and shown as well as insets in Fig. 4.10. Behind the preamplifier only minor changes can be observed. The main difference is seen behind the EDFA: the pulse shape is strongly modulated and the signal level relative to the ASE background became worse.

The reason for this behavior is a pulsed operation of the EDFA, where the incoming pulses are amplified during a very short time. For the rest of the time without any

pump the EDFA produces only ASE, leading to the deterioration of the SNR. These types of EDFAs are designed mainly to be used with cw radiation, but not for the pulsed application where the main time the EDFA is in idle[5].

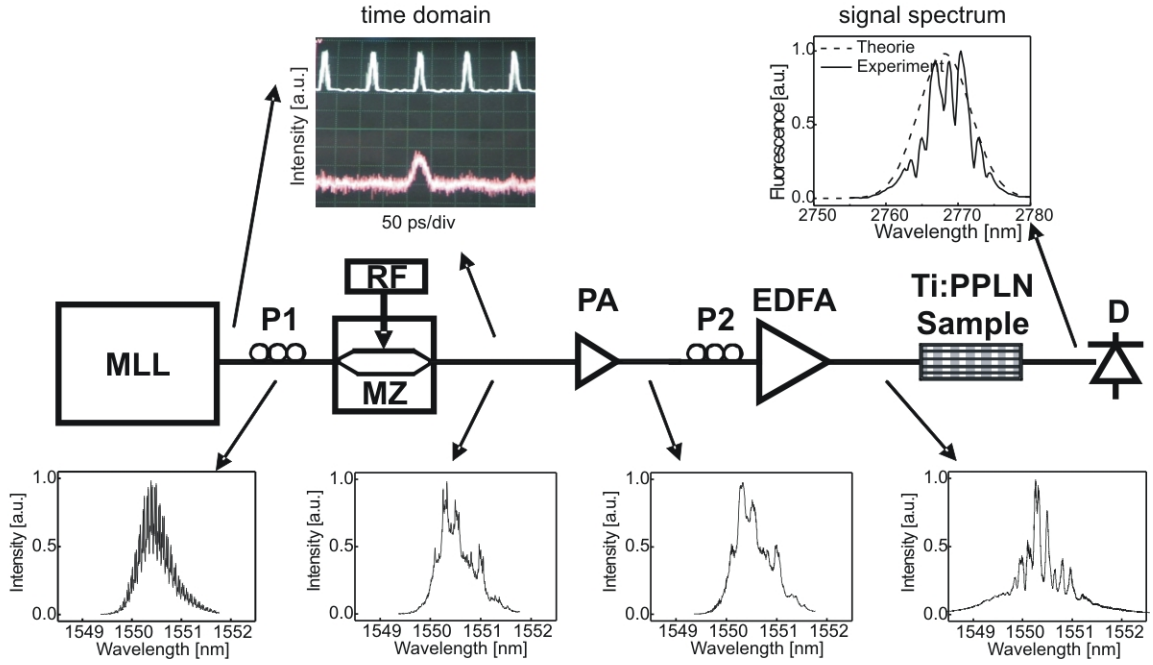


**Figure 4.10:** MLL-pulses before and after pulse picking by the modulator are presented in the time domain in the upper left part. Corresponding spectra are displayed in the lower row of diagrams. A typical measured (solid line) and calculated (dashed line) signal spectrum is shown in the right upper part.

A second possible reason for the pulse distortion is the high peak power in the fiber itself. It can reach several hundred W or even kW, depending on the duty cycle to be used. This leads to an increase of nonlinear effect in the standard telecommunication fiber and therefore - pulse distortion.

Such pump pulse behavior should be transferred to the MIR pulses. The spectral properties of the signal pulses, taken with the monochromator (resolution 2 nm) are also shown as inset in the figure. The measured linewidth corresponds to the calculated one of the undisturbed pump pulse (shown in inset as dashed line) and is 8.5 nm. Similar results are also found at the idler wavelength (not shown in the figure).

[5]Unofficial information from the company: in the pulsed mode of operations duty cycles up to 40 % are allowed.

## 4.7 Stretching and Compressing of Pump Pulses

### 4.7.1 Motivation

Fig. 4.11 shows the calculated OPG power versus the pump power in double logarithmic scale, calculated by Dr. W. Grundkötter [54]. Optical parametric generation starts with spontaneous decay of a pump photon generating two MIR photons. By increasing the pump power level the process is transformed from the spontaneous to the stimulated emission, as it was described before; this leads to the highly nonlinear dependence of the output power characteristics. At some high pump power levels oscillations near saturation is predicted by the theory. This happens due to back conversion processes (Sum Frequency Generation) of generated signal and idler (for detailed explanation see [54]). Idler spectra for the different pump powers are also shown in Fig. 4.11 as insets: no pulse broadening is observed, if relative low pump power (1 W) is used and pump depletion and SFG may be neglected. After some pump power level it cannot be neglected any more. Back conversion processes lead to the broadening of the „pump“ and MIR spectrum.

Generation of pump pulses of even higher power would allow to reach back conversion processes and, therefore, to check the theoretical calculation. Additionally this would allow to fabricate nonlinear devices of high power for spectroscopic applications.

### 4.7.2 Idea and Experimental Setup

The technique for a Chirped-Pulse Amplification (CPA) was proposed by D. Strickland and G. Mourou [55] and used for the first time for radar pulses. The following idea has been implemented: to avoid high peak powers inside the amplifiers (and fibers), short pulses first of all have to be stretched using a dispersive fiber, or a Bragg grating etc., afterwords amplified (in this case no high peak power is achieved due to the pulse broadening in the time and no idle time of the amplifier itself), and later compressed. Using free space optics allows to avoid problems like pulse distortions, which for example took place, as it was mentioned in the previous section.

An experimental setup[6] to use even higher peak power levels and therefore even stronger stimulated emission in the infrared is shown in Fig. 4.12.

As a laser source ps fiber laser has been used. Output wavelength was selected to be 1548 nm; modulation frequency was 20 MHz. FWHM of the pulses were 5.4 ps (Fig. 4.13). Standart telecommunication fiber (500 m long) was utilized to produce a pulse stretching. Amplification was done in the erbium doped fiber amplifier. A pair of gratings was used to compress the amplified pulses again. The „Time bandwidth product“ in front of the sample was 1.3. Behind the sample following equipment was used: Lenses for collimating and focusing the MIR output, a germanium filter to block unused pump radiation and a HgCdTe detector for measuring output power levels of signal and idler. Polarization controllers before EDFA and sample are not shown in

[6]The work has been done in collaboration with the group of Dr. V. Couderc (Limoges, France)

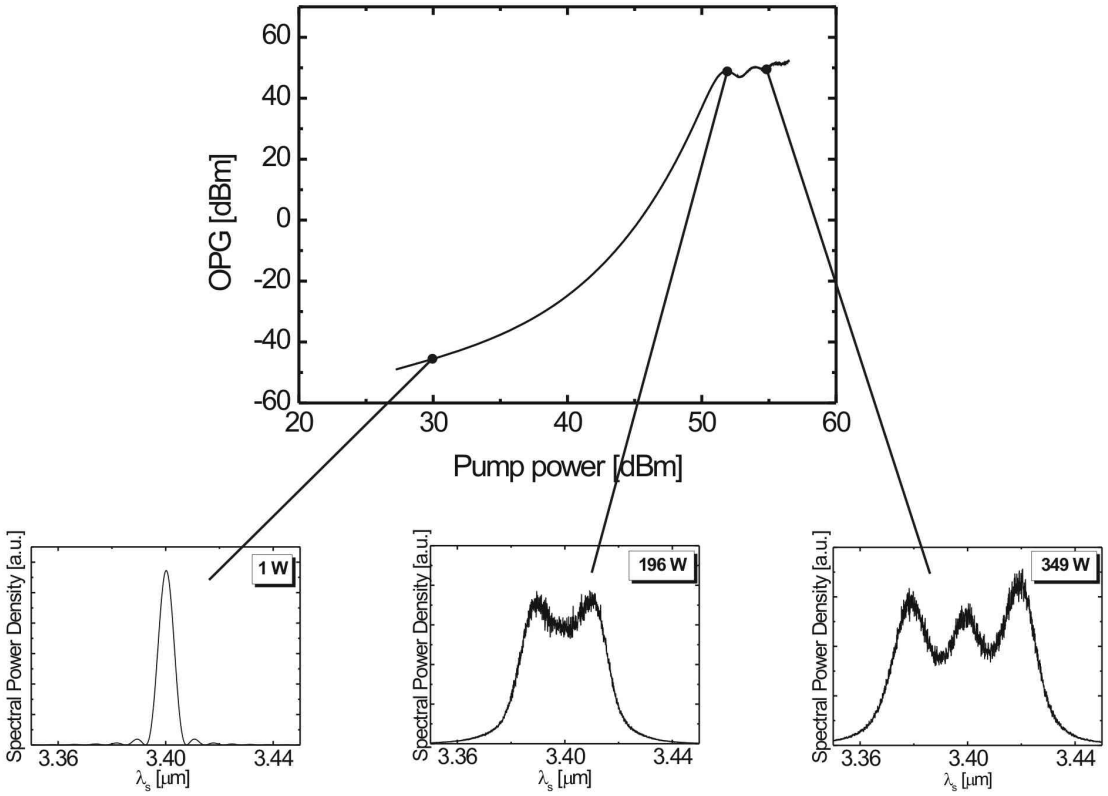


**Figure 4.11:** Total OPF power vs. pump power for continuous pumping; idler spectra for the different pump power are shown in insets. Parameters: $\lambda_p = 1550$ nm; $\lambda_s = 2849$ nm; $\lambda_i = 3400$ nm; L = 94 mm.

the picture. The pulse length behind the laser and in front of the sample has been measured with the help of an autocorrelator.

For power investigations sample with following parameters was used: $\Lambda = 31.44$ $\mu$m; w = 20 $\mu$m, T = 25 ℃; losses 0.131 dB/cm; TM polarization.

### 4.7.3 Results and Discussion

The output peak power of the MIR fluorescence versus the output peak pump power is shown in Fig. 4.14 (left). Here signal and idler pulses are measured together with one detector. The peak power levels were calculated by measuring the average power levels and taking into account measured with the autocorrelator pump pulse duration (5 ps). According to the repetition rate of 20 MHz the duty cycle should be 1/10000 for pump and for the MIR radiation as well by neglecting the dispersion properties of the media.

The linear dependence of the MIR power versus the pump power corresponds to the theoretical results for the power levels close to saturation, where back conversion

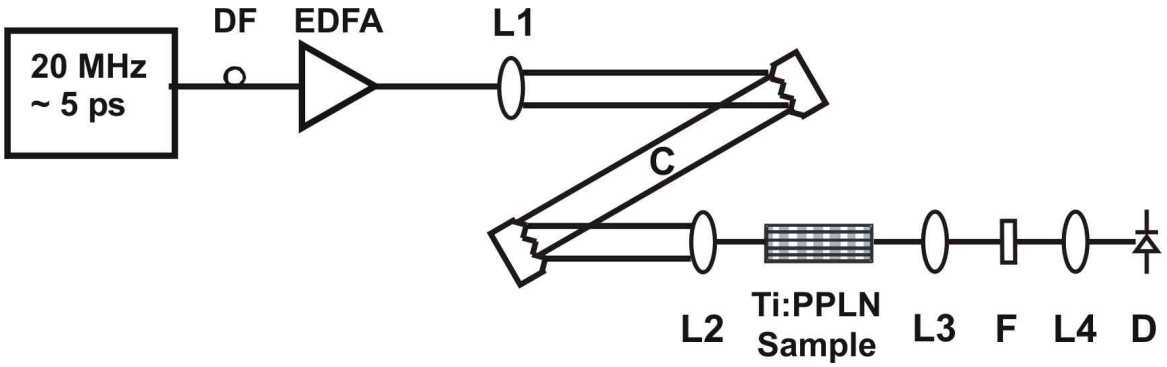


**Figure 4.12:** Schematic diagramm of experimental setup for stretching and compressing the pump pulses: DF - Dispersive Fiber; EDFA - Erbium Doped Fiber Amplifier; L1 - Collimating lens; C - grating pulse compressor; L2 - focussing lens; L3 and L4 - collimating and focussing lens; F - germanium filter; D - HgCdTe detector.

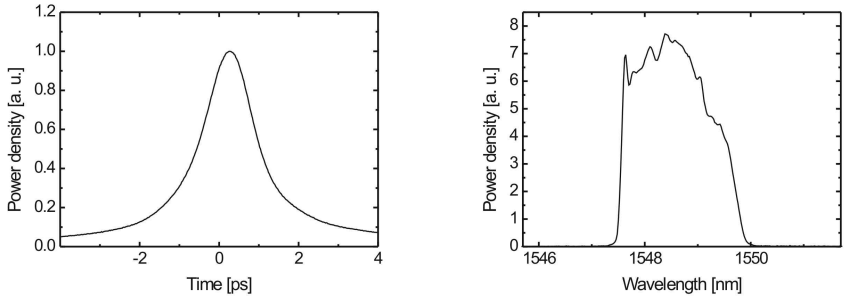


**Figure 4.13:** Pump pulses in the time (left) and frequency (right) domains, used for the generation of the MIR radiation with high duty cycles.

processes have already to be taken into account. Measured results are compared with theoretical (Fig. 4.14 right) and large discrepancy of about 3 order of magnitude between calculated and measured output power levels is found. Several possible reasons can lead to such large difference: a non transform limited pulse was used to realize a pumping. A time-Bandwidth Product (TBP) of 1.3 has been calculated from the measured characteristics in time (with a autocorrelator) and frequency (with a spectrum analyzer) domains. For comparison - the MLL system in our laboratory (see section 4.6) has TBP of 0.55. The second important reason is the probable photorefrective effect, which also can significantly modify the output characteristics. This might be avoided by increasing the temperature above 150 °C. Also a strong green luminescence inside the waveguide was easily observed.

Experimental results as a whole can be shifted to the left if coupling losses would be estimated more precisely. At the moment they were calculated from the transmitted pump power.

These experiments were done in a laboratory of the University of Limoges, therefore spectral characteristics of MIR radiation were not taken, which are for the great

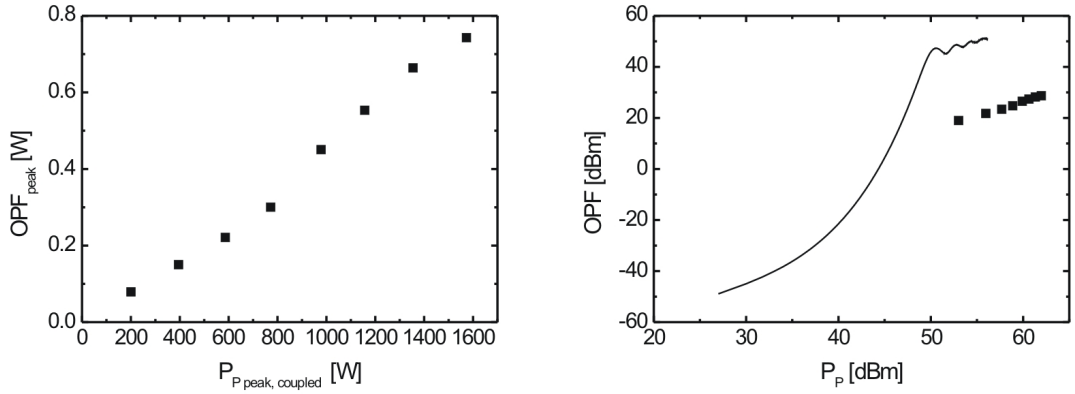


**Figure 4.14:** Total OPF peak power vs. coupled peak pump power for the chirped-pulse amplification technique (left); Comparison between calculated (solid line) OPF power and experimental results (dots) for the high power levels (right).

interest for understanding the behavior of power characteristics at these power levels.

Power oscillations near saturation level were not observed. But this can have the same origin as another discrepancy in results: the power level of the generated MIR radiation was very low in comparison with the expected results and proper pump pulse generation is necessary.

## 4.8 OPG in Bent Waveguides

Bent waveguides are promising candidates for OPG due to the doubled waveguide length in comparison with straight ones. Simultaneously they have the losses as low as in the straight waveguides. Therefore such structures were also characterized for their spectral and power characteristics.

The experimental setup for the spectroscopic investigations is quite similar to that one used for the straight waveguide. Coupling of the pump radiation has been realized in this case via fiber butt coupling. The orientation of the pump polarization was checked behind the sample [7]. Tuning characteristics taken at a temperature of 30℃ is shown in Fig. 4.15.

The tuning characteristics measured by changing the pump wavelength in the range 1535 - 1545 is shown in the middle. This leads to the tuning of the MIR radiation in the range 2900 - 3250 nm. Examples of spectra at several different pump wavelengths are shown as insets. A linewidth of about 15 nm was measured far from degeneracy. Near degeneracy a linewidth of about 72 nm was observed[8]. The experimental results are with excellent agreement with theoretical calculations. Despite the same domain

[7]Using a polarization maintaining fiber will provide a stable polarization state without later control.

[8]The horizontal scale is two time larger in this case to have an option to see the whole spectrum.

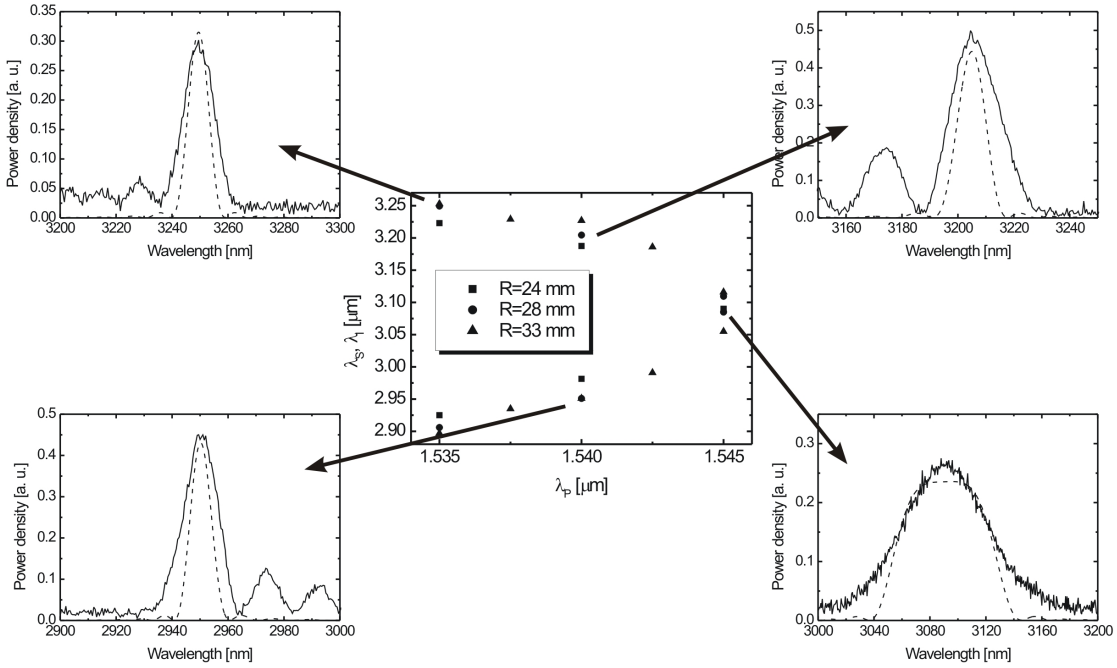


**Figure 4.15:** Measured (solid line) tuning characteristics of OPG in different bent waveguides as signal and idler wavelengths versus the pump wavelength in cw-operation (middle diagram) and corresponding measured and calculated (dashed line) signal and idler spectra for different pump wavelengths as an example: T = 30 °C; straight part of the waveguides is 24 mm.

periodicity has been used for the whole sample ($\Lambda = 31.60$ $\mu$m) discrepancy of several nanometers of each particular MIR radiation for different waveguides is observed. The reason for such behavior can be some effects which have place only by fabricating bent waveguides. The main one - is thermal expansion of the sample in the different crystallographic directions. During the fabrication the sample at different steps has different temperature and therefore not all the time coaxial overlap of waveguides and domains is possible. By having domains oriented under a certain angel to each other at conjugation points some displacements in the phase matching condition can happen.

Efficiency of OPG in bent waveguide structures has been investigated (Fig. 4.16). The power characteristics was measured for waveguides of different radius of curvature and therefore different length. Spontaneous emission of the MIR radiation in the longest waveguide starting at about 400 - 500 mW of the coupled pump power is clearly observed. MIR power level of two inner bent waveguides, differ from the longest one, show the output power characteristics of the same level. To compare an efficiency of the bent to the straight waveguides power characteristics of the straight sample is shown as an example in Fig. 4.16 as well. MIR power level of the straight sample (L = 94 mm) showing the same results as two inner waveguides with radiuses of curvature 24 and 28 mm.

The following conclusions can be drown at this point: the bent waveguides are

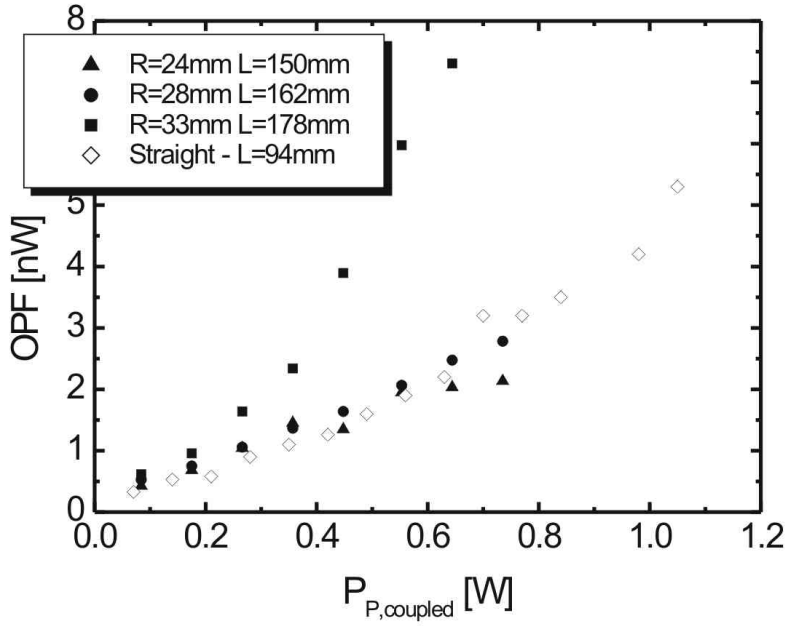


**Figure 4.16:** Measured OPG power characteristics for bent waveguides of different radius of curvature (filled dots) and for a shorter straight waveguide (unfilled dots) for comparison vs. coupled pump power: T = 30 °C; $\lambda_p$ = 1544 nm; $\lambda_s$ = 3000 nm; $\lambda_i$ = 3181 nm; straight sample: L = 94 mm.

showing the same power characteristics as the straight waveguide which is shorter by 60 - 70 %. Here one has to take into account that losses of such sample are rising nonlinear towards middle of the wafer. In this case overall losses for the bent waveguides were 0.291, 0.163 and 0.126 dB/cm correspondingly. The losses of the straight waveguide are about 0.1 dB/cm. These parameters in combination with the waveguide length give higher losses for the bent structure. Anyway, these bent waveguide are showing a power characteristics, comparable with the straight one. If losses for all bent waveguide would be comparable with that one with the radius of 33 mm, than an even larger output power may be expected. Earlier stimulated emission in the bent waveguide in comparison with the straight one is a good example for that.

## 4.9 Conclusion

The optical Parametric Generation in Ti:PPLN waveguides was reported. Fig. 4.17 shows in double logarithmic scale the total power characteristics of experiments with different peak power levels in combination with a calculated dependence for comparison. The process starts with spontaneous emission having a linear dependence of OPG power versus pump up to 35 dBm for the particular parameters (sample length 94 mm;

$\lambda_p = 1550$ nm; $\lambda_s = 2849$ nm; $\lambda_i = 3400$ nm). Experimental results with cw-radiation from an ECL laser in combination with an EDFA are in a good agreement with the theoretical prediction.

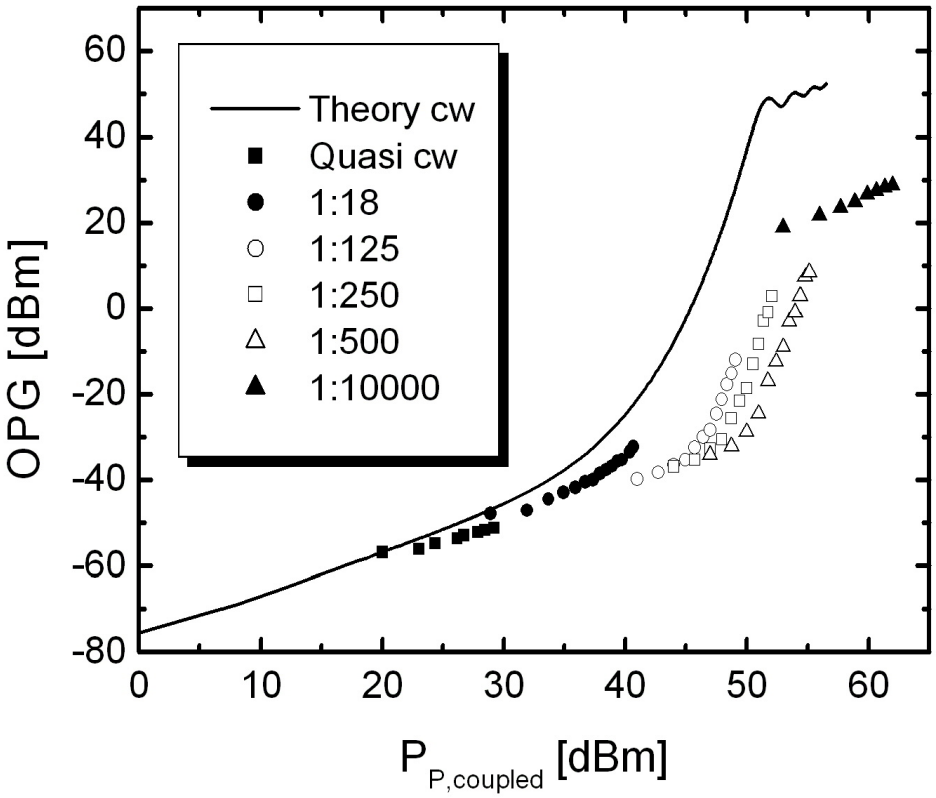


**Figure 4.17:** Total OPF output (peak) power versus coupled pump (peak) power in a pulsed mode of operation (6.4 ps pulses of different duty cycles as given in the inset) compared with results of a theoretical analysis (dotted line).

Nonlinear rise of theoretical curve starting at about 35 - 40 dBm is showing the stimulated part of the nonlinear interaction going up to levels of 50 dBm. Experimental results are following the same dependence, which gives a sign, that stimulated emission of MIR radiation may also be observed. Nevertheless, the overall power level of MIR radiation is lower than the theory predicts. As it has been described before, not transform limited pulses have been used to pump efficiently the nonlinear device. Pump pulse distortion and as a consequence MIR pulse distortion have been observed, which was not taken into account by the theoretical modelling, describing the real case of interaction. Pump pulses can be easily characterized in time- as well in frequency domains and therefore pulse peak energy is possible to estimated very precisely at intermediate power levels. In contrary to this MIR pulses could be characterized only in the frequency domain with a help of monochromator. Real powers can only be

calculated by concerning GVM[9] at particular pump and MIR wavelengths. Despite small difference in GVM (detailed description may be found in chapter 5.4) still some corrections for the duty cycle are necessary. Pulse broadening cannot be measured at the moment to estimate the real duty cycle and therefore real peak power level of MIR pulses.

As results have shown, by slicing the pulses from the pulse train signal-to-noise ratio became worse and therefore the calculated peak power level and part, involved into the interaction, may differ. That means, that the overall pump power level has to be reduced and experimental results can be corrected and moved as a whole to the lower pump power, approaching theoretical modelling.

Additionally, at high power levels no direct measurements of pump pulse power were possible. The average power level has been measured. Pulses were attenuated and according to the duty cycle peak power level was recalculated, which may differ from original pulses due to the different fiber components used at such high power levels. For the slicing of picosecond pulses nonlinear properties of the fiber seems to become the main limiting factor for the generation high power pulses using this technique. Therefore, MIR power level may be even higher if proper pump pulses would be used.

The average propagation losses in the MIR range in the waveguide have been used for the modelling. The pump propagation losses have not been measured. By taking into account these parameters the output characteristics also can be shifted as a whole to the left.

Due to the photorefractive effect, which also was observed with increasing pump power levels, reduction in efficient generation of the MIR radiation has to be considered. High MIR power fluctuations in this case were observed. Generation of the third harmonic of the pump (green fluorescence), but also the SFG (yellow and red) was observed very clearly and spectrally resolved. Non stable intensity of this radiation could give a sign about some temperature fluctuation inside the waveguide, as well as instability in polarization of the pump. Heating up the sample to temperatures above 150 °C could reduce the photorefractive effect and therefore increase the MIR power level. Good isolation of the device itself from the environment has to be provided. Otherwise a temperature gradient would produce undesirable air convection and inhomogeneity inside the waveguide.

Despite all of the reasons, which have been listed before and might lead to reduced output power level, a behavior of measured data follows the theoretical modelling also for the stimulated fluorescence emission. If all the mentioned problems would be eliminated, it gives a good chance to approach mathematical model.

At pump power levels (Fig. 4.17 above 50 dBm, theoretical curve changes its slope and periodical output power behavior is predicted. This effect happens due to the back conversion process and generating pump from signal and idler [10]. In this case also MIR power level could not achieve theoretical modelling due to similar reasons as

[9]GVM - **G**roup **V**elocity **M**ismatch

[10]Detailed explanation can be found in PhD thesis of Dr. W. Grundkötter [54]

it was mentioned before. The same behaviour in the experiment was not observed as well as no information about generated MIR pulses. Despite it, the same pump power levels of theoretical and experimental results without any fit parameters may give a sign, that we are on a right way, and, if an equipment would allow, even higher MIR power levels can be achieved.

Anyway, MIR radiation in the range of nine orders of magnitudes starting at nW and approaching 1 W of peak power level just for one throughput of the pump makes such type of devices preferred candidates for spectroscopic applications in comparison with similar bulk devices.

# Chapter 5

# Optical Parametric Oscillators

## 5.1 Introduction

Optical Parametric Oscillators (OPOs) are the light sources, similar to the lasers. Their gain is based on the parametric amplification in a nonlinear crystal. Emission wavelength of the most lasers may be tuned in the relative narrow range. OPOs, contrary to them, may be tuned in the whole transparency range of the material. OPGs may be also used for spectroscopic applications in the large wavelength range if sufficient output power is provided. But if the high spectral resolution is necessary, OPGs with relative large linewidth cannot be used any more. Optical Parametric Oscillators are the candidates for this type of applications. High cavity quality and therefore narrow linewidth going down to 100 kHz [56], which is comparable with available on the market ECL lasers and large tuning range makes these devices unique and irreplaceable.

As it has been shown before, OPF power grows in an OPG along the interaction length, if sufficient pump power is provided. At relatively low power levels the parametric gain compensates internal losses (scattering and absorption). But if nonlinear crystal, described in the previous section, would be placed between appropriate mirrors, building in this way an optical cavity, oscillation at two new frequencies $\omega_s$ and $\omega_i$ can be achieved. Their emission is defined by the phase-matching condition (Eq. 2.26). Above oscillation threshold a growth of signal and idler power continues with increasing pump power until depletion of the pump wave and resulting gain saturation set in.

Depending on the mirror configurations several types of Fabry-Perot resonators are possible:

- **SRO** - **S**ingly **R**esonant **O**PO: high reflectivity mirrors for one wavelength only (Fig. 5.1b). Tuning is possible[1];
- **DRO** - **D**oubly **R**esonant **O**PO: high reflectivity mirrors for two wavelengths,

[1]Here as well as for DRO and TRO a single cavity is considered.

usually for signal and idler (Fig. 5.1c). Single-step tuning is possible (see Chapter 5.3);

- **TRO** - **T**riply **R**esonant **O**PO: high reflectivity mirrors for all wavelengths involved in the interaction. No tuning is possible;

The generated resonant wave will be reflected from the outcoupling mirror and propagates back without any amplification. Only waveguide losses will determine the amplitude of this wave. In case of SRO low reflectivity of the nonresonant wave is desirable to minimize the feedback. Otherwise, the SFG may occur, leading to generation of new frequency at the pump wavelength. Efficiency of the device will be reduced in this case.

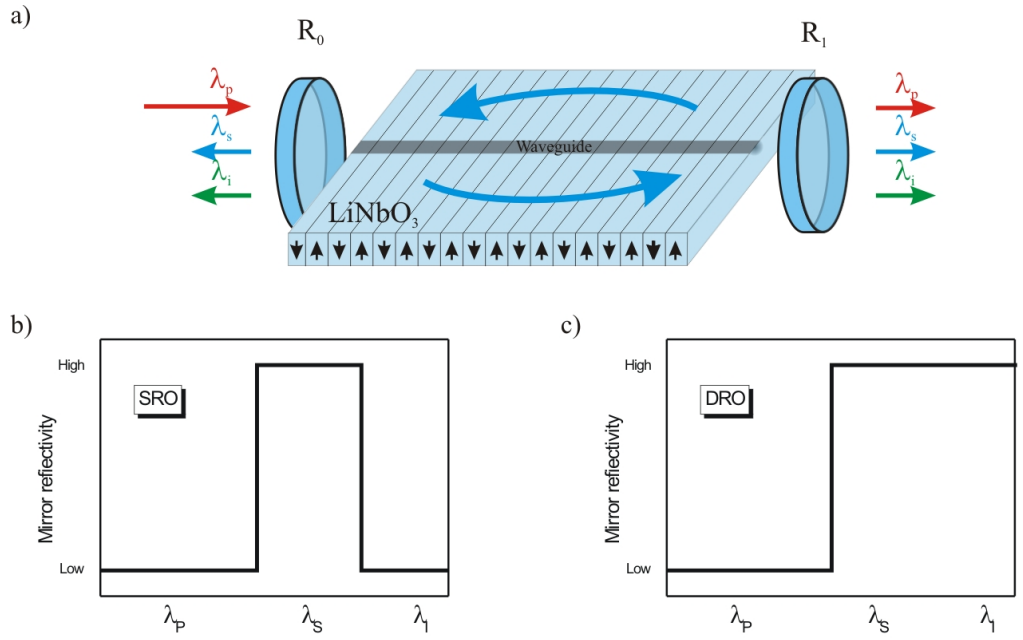


**Figure 5.1:** Schematic diagram of an OPO (a); mirror reflectivity for SRO (b) and DRO (c).

DRO devices will oscillate if $M \cdot n_j \lambda_j$ of both resonant wavelengths will be equal to the optical cavity length, where $M$ is an integer number and $n_j$ and $\lambda_j$ are the index of refraction and the wavelength.

OPOs can be classified by the state of polarization stand of all waves, involved in the interaction:

- **OPO type I** - all waves have the same polarization{eee}[2];
- **OPO type II** - the two generated waves are of orthogonal polarization{eoe}[3].

[2]{eee} - polarization all three waves is parallel to $n_e$.
[3]{eoe} - polarization of the pump and one generated wave is parallel to $n_e$, the other one - to $n_o$.

First publications on lithium niobate OPOs can be found in [57]. Tunable radiation in the range 0.97 to 1.15 $\mu$m has been reported. Nowadays, these devices are used mainly for spectroscopic applications (for example [56, 58–60]) due to the large tuning range, limited only by the crystal transparency. Gas sensing using OPOs as a pump is also used worldwide [61, 62].

First Integrated OPOs with a high finesse Ti:$LiNbO_3$ cavity has been demonstrated in 1981 [63, 64]. Generation of tunable radiation in the wavelength range 0.95 - 1.6 $\mu$m using a pump near 0.6 $\mu$m was demonstrated. In the meantime a lot of further work has been done to improve spectral properties, tunability and waveguide characteristics; the latest results will be shown below.

Optically induces damage of the index of refraction, which is already known since the early seventieth [65] is still playing an important role for the nonlinear interaction. In case of OPOs it may be even critical, while minor changes for the pump will lead to the large changes in the MIR output due to the cavity. In bulk a higher resistivity to photorefractive damage has been observed and magnesium doped periodically poled lithium niobate (MgO:LN) [66–71] has been used for many different experiments [72–76].

The same approach has been investigated in our group to reduce the photorefractive damage also in waveguides, but no significant improvement was observed [77].

## 5.2 Device Characteristics

### 5.2.1 Threshold Pump Power

The basic operational principle of OPOs is similar to that of lasers. The difference in the nature of the optical gain in the gain medium. In lasers amplification is achieved by stimulated emission and in OPOs by parametric amplification. Modeling of OPOs is based on the same principles as modeling of OPGs with the difference for the boundary conditions. As a basic system coupled equations (4.1) can be taken. As the boundary self-consisting of the wave has to be taken. The best way to organize such equations is using a matrix formalism [36], where the wave after the round trip will be described similarly to the input wave, multiplied with ABCD-matrices (two times propagation matrix and two times reflection matrix). This means that the determinant of the matrices have to be equal one.

According to this, the internal pump power threshold for DRO and Single Pump (SP) path with symmetric resonator mirrors for each wavelength ($R_{s0} = R_{s1} = R_s$ and $R_{i0} = R_{i1} = R_i$)[4] can be obtained [26, 78]:

$$P_{th} = \frac{\pi^2}{8} \frac{\epsilon_0 c^3}{d_{33}^2 \tilde{\kappa}^2} \frac{n_p n_s n_i}{\omega_s \omega_i} \left[ \frac{\alpha_p}{1 - e^{-\alpha_p L}} \ln\left(Q + \sqrt{Q^2 - 1}\right) \right]^2 \tag{5.1}$$

[4]Indices 0 and 1 correspond to the in- and outcoupling mirrors

and resonator $Q$-factor:

$$Q = \frac{1 + R_s R_i e^{-4\alpha L}}{(R_s + R_i) e^{-2\alpha L}} \tag{5.2}$$

Similarly, the internal pump threshold can be calculated for an SRO and SP ($R_{s0} = R_{s1} = R_s$ and $R_{i0} = R_{i1} = 0$):

$$P_{th} = \frac{\pi^2}{8} \frac{\epsilon_0 c^3}{d_{33}^2 \tilde{\kappa}^2} \frac{n_p n_s n_i}{\omega_s \omega_i} \left[ \frac{\alpha_p}{1 - e^{-\alpha_p L}} \operatorname{arccosh}\left( \frac{e^{2\alpha L}}{R_s} \right) \right]^2 \tag{5.3}$$

where $\alpha_p$ and $\alpha$ are the propagation losses for the pump and generated MIR radiation ($\alpha_s = \alpha_i = \alpha$) correspondingly and $\tilde{\kappa}$ is an overlap integral.

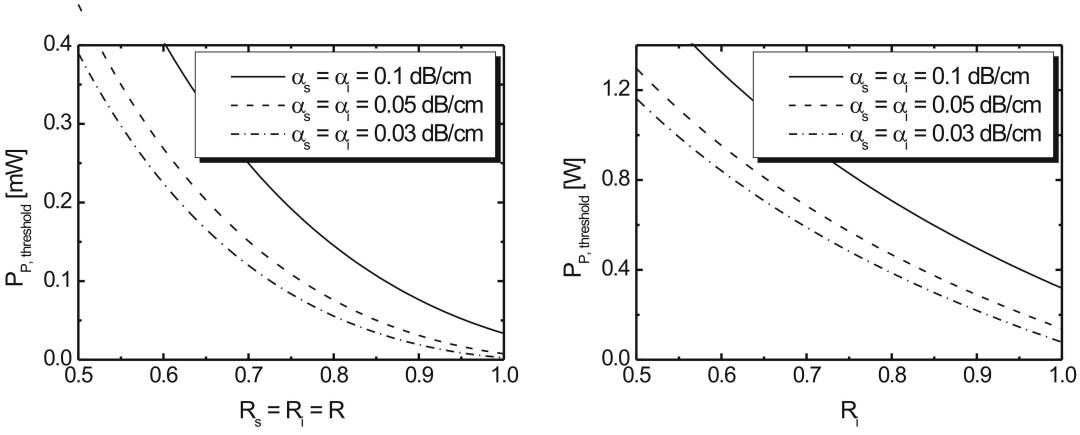


**Figure 5.2:** Calculated threshold pump power of a DR-OPO (left) and of a SR-OPO (right) as function of the reflectivity of the cavity mirrors: T = 50 ℃; $\lambda_p$ = 1565 nm; $\lambda_s$ = 2988 nm; $\lambda_i$ = 3286 nm; L = 89.5 mm; $\omega$ = 20 $\mu$m; for SRO $R_s$ = 5%.

Fig. 5.2 shows the calculated threshold characteristics for integrated SP- DRO and SRO. The losses for the MIR radiation are equal and shown in the legend. Losses for the pump wavelength are taken two times higher than for MIR radiation. Calculations for DR-OPOs show, that a threshold below 100 mW is possible, even if not the lowest possible waveguide losses have to be taken and mirror reflectivities just above 85 %. The mode profile along the whole interaction length cannot be achieved in bulk devices, and therefore threshold parameters are of the order of magnitude larger.

As it has been reported before, waveguides of the length of about 90 mm with propagation losses of about 0.03 dB/cm have been fabricated and reported. With mirrors of a reflectivity above 95 % for the resonant wavelengths it is possible to achieve experimentally threshold values of only 14 mW [26]. For such devices even no pump amplification is necessary and they can be pumped by a diode laser[5].

SP-SROs have a higher threshold than DROs, but can have better spectral properties; therefore, they are in general better suited for spectroscopic applications[6].

[5]Nowadays, diode lasers have a maximum output power level up to 80 mW

[6]Details will be described below

### 5.2.2 Cavity Characteristics

As it was mentioned above, OPOs in comparison with OPGs are much more sensitive to the different losses inside the cavity, which may significantly influence the power characteristics of the device. Therefore, propagation losses and mirror reflectivity have to be characterized and taken into account.

Fig. 5.1 shows the OPO with a Fabry-Perot cavity. The transmission of the cavity can be written in the form [79]:

$$\frac{P_t}{P_0} = \frac{(1-R_0)(1-R_1)\exp(-\alpha L)}{1+R_0R_1\exp(-2\alpha L) - 2\sqrt{R_0R_1}\exp(-\alpha L)\cos(2\beta L)} \tag{5.4}$$

where $P_0$ is the power in front of the cavity, $P_t$ - transmitted power; $R_0$ and $R_1$ are the reflectivities at in- and outcoupling mirrors and $\beta$ is a propagation constant inside the waveguide.

Similarly reflectivity can be written:

$$\frac{P_r}{P_0} = \frac{R_0 + R_1\exp(-2\alpha L) - 2\sqrt{R_0R_1}\exp(-\alpha L)\cos(2\beta L)}{1+R_0R_1\exp(-2\alpha L) - 2\sqrt{R_0R_1}\exp(-\alpha L)\cos(2\beta L)} \tag{5.5}$$

The maximum transmission is achieved in case, when the phase of the resonated wave after one round trip differs by a factor $N \times 2\pi$, where $N$ is an integer number. According to Eq. 5.4 transmission for different propagation losses at $\lambda = 3394$ nm ($\alpha = 0.03,\ 0.05$ and $0.10$ dB/cm) for a sample of 100 mm length and $R_0 = R_1 = 95$ % is shown in Fig. 5.3.

To characterize the cavity *finesse* $F$ has to be introduced, which is defined as a ratio:

$$F = \frac{\delta\lambda}{\Delta\lambda} = \frac{\pi}{\arccos\left(\frac{2\sqrt{R_0R_1}\exp(-\alpha L)}{1+R_0R_1\exp(-2\alpha L)}\right)} \tag{5.6}$$

where $\delta\lambda$ is the free spectral range and $\Delta\lambda$ is the linewidth.

The higher the finesse is, the lower will be the pump threshold. For integrated MIR OPOs, depending on the mirror reflectivity and waveguide losses finesse was measured in the range 20 - 27. According to the parameters for the Fig. 5.3 finesse will be 26, 19 and 11 for losses equal to 0.03, 0.05 and 0.1 dB/cm respectively.

### 5.2.3 Dielectric Mirror Coating

To build up the resonator mirrors are necessary, which will have a high reflectivity for one wavelength and a high transmission for another one. Metallic mirrors have a very high reflectivity (HR) for a large wavelength range and cannot be used. Additionally, high field intensities will lead to increase of the losses of these mirrors. Therefore, dielectric mirrors consisting of multiple thin layers of a transparent lossles material for this particular wavelength may be used [80]. Each layer may have relative small reflective coefficients due to low refractive indices contrast in between, but reflection

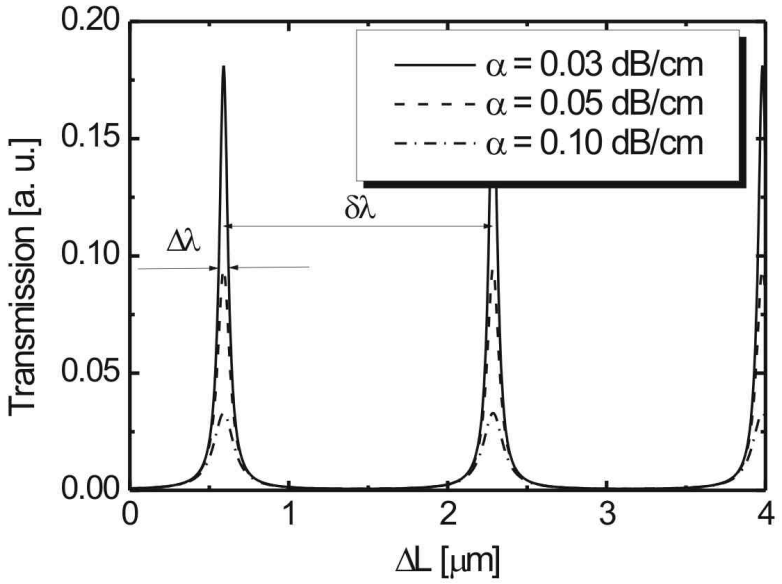


**Figure 5.3:** Calculated transmission of an integrated Fabri-Perot Interferometer as function of the optical path change for different damping coefficients: $\lambda = 3394$ nm; L = 100 mm; $R_0 = R_1 = 95\%$.

from many layers will lead to the constructive interference (at certain wavelength) and therefore very high reflectivity (up to 99.999 %).

This type of mirror has a *quarter wavelength* - condition, or in other words, thickness of each layer is equal to the quarter of the wavelength for which this particular mirror is designed.

Resonator cavities for integrated OPOs are formed by depositing $SiO_2$ and $TiO_2$ layers with index of refraction of about 1.4 and 2.4 correspondingly, which are transparent materials in the MIR range (0.2 - 3.5 $\mu$m for $SiO_2$ and 0.4 - 6.5 $\mu$m for $TiO_2$). Usually, 12-layers stack has been used and deposited either on external substrate of LN or sapphire, or deposited directly on the waveguide end face. Additionally, a test substrate of $CaF_2$ has been coated to measure the transmission properties with the help of spectrometer. Achieved results later have been corrected according to reflective coefficients of materials.

Deposition of the $SiO_2/TiO_2$ has been assisted by the *ion evaporation*. In this way additional energy is introduced into the deposited film and increases its adhesion, density and oxidization [81]. This also allows to do an evaporation at moderate substrate temperatures. In the previous years an ion energy of 130 eV has been used for the fabrication of HR and AR mirrors for near infrared. Due to the thick layers, needed for the MIR, this energy is not sufficient to provide a good mirror quality. Relative heavy titanium atoms produced a porous layer structure, if the same energy level of

130 eV was used as for silicium oxide. Therefore, the ion level was increased up to 250 eV. Comparison of single $TiO_2$ layer for different ion energies is shown in Fig. 5.4. A picture, taken by the electron microscope shows very porous structure if the ion energy of only 130 eV has been used (Fig. 5.4 left), and layer without any capillary structure on the right. These parameters will be used later on for the deposition of MIR mirrors.

An example of calculated for $\lambda/4$ at 3000 nm and deposited on a sample glass transmission spectra for DROs is shown in Fig. 5.5. The mirror consists of 12 alternate layers of $SiO_2$ and $TiO_2$ and has a reflectivity of about 98 % in the wavelength range 2700 - 3400 nm; the transmission at the pump wavelength is about 80 %. Experimental results agree well with calculated ones.

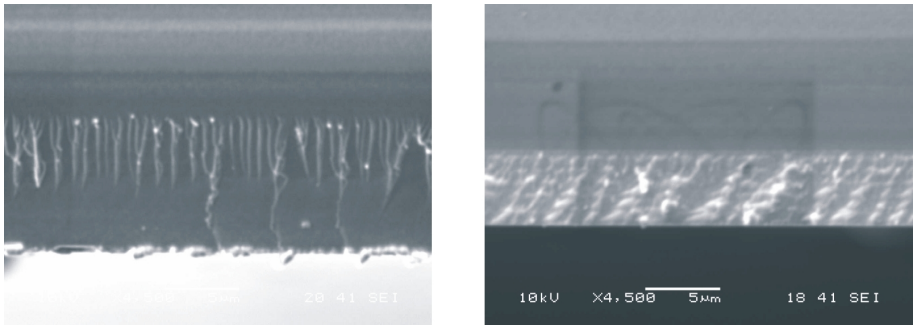


**Figure 5.4:** Pictures, taken by the electron microscope for a single $TiO_2$ layer with ion assisted evaporation of 130 eV (left) and 250 eV (right)[82].

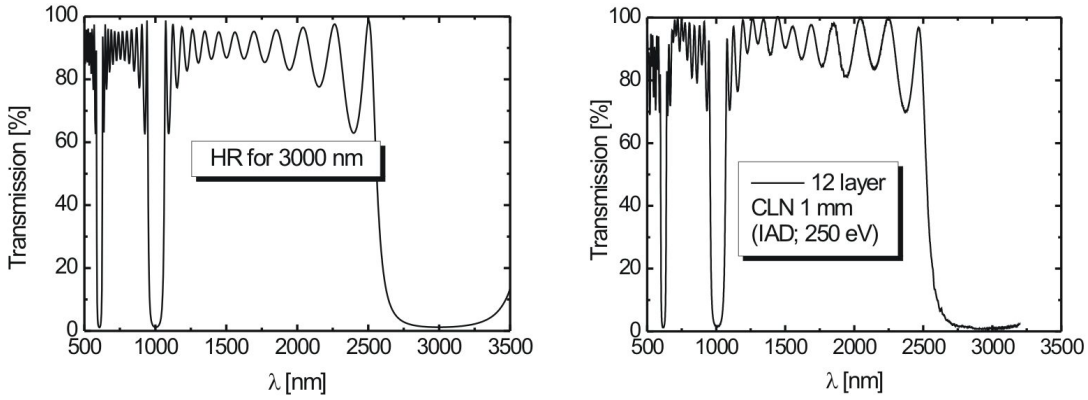


**Figure 5.5:** Calculated transmission for 12 layers of $SiO_2$ and $TiO_2$ (left) and deposited on a test substrate (right) for a Doubly Resonant OPO.

## 5.3 Doubly Resonant cw-Oscillators

The main advantage of DROs is a low pump threshold, necessary for the oscillation. Therefore, these devices have been investigated and characterized first. Spectral and power properties have been measured and will be presented in the following chapter. First integrated OPO with deposited dielectric mirrors will be shown.

### 5.3.1 Mirror Characteristics: External vs. Deposited

The resonant cavity can be formed using either commercial external dielectric mirrors (sapphire substrate, dimensions: 3 × Ø12 mm; AR coating for the pump on the back side) or directly deposited mirrors on the waveguide end face (Fig. 5.6). Both mirror configurations have advantages and disadvantages, but utilizing deposited mirrors is preferable.

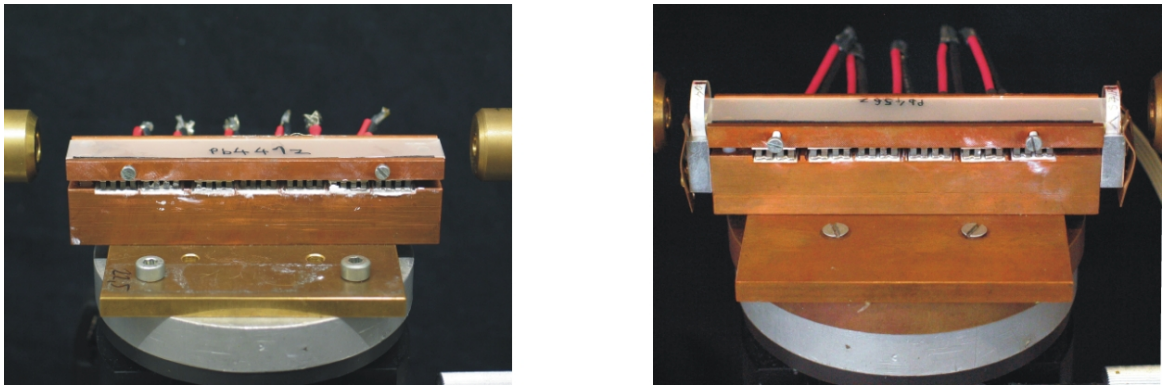

**Figure 5.6:** Integrated OPO with dielectric mirrors directly deposited on the waveguide end face (left); external dielectric mirrors, clamped to the waveguide end face (right).

Deposited mirrors have the same spectral properties as external ones. Most of bulk OPOs have only one or even no deposited mirror and relatively complex cavity configurations like „Bow-tie“ with 4 mirrors. They have to be properly aligned. The advantage of integrated OPOs with deposited mirrors is that no additional mirror adjustment necessary. This allows to fabricate very compact devices.

The main disadvantage of the deposited mirrors, especially for MIR radiation, is their relatively bad quality at the waveguide end face. Though test substrates are showing very good spectral properties (see Fig. 5.5), the deposition of relatively thick layers (each layer of $SiO_2$ has a thickness of about 500 nm and of $TiO_2$ about 350 nm) for MIR near 3000 nm on the edge of LN sample could not provide the same quality as the external commercial ones: some defects and bubbles are observed on the dielectric layers; also with time deposited mirrors are not stable[7]. Therefore, external clamped mirrors are at the moment still preferable for the integrated OPOs of the low threshold power in the MIR range, as will be shown later.

[7] A peeling of single dielectric layers sometimes has observed.

External mirrors have to be properly adjusted at both sides. No gap should exist between mirror and waveguide end face. Also no tilting of the mirror is acceptable. Relatively thick external mirrors (thickness 3 mm and larger) do not have such tilting problem (or the problem is not that much critical) and are relative easy to be installed and fixed perpendicular to the waveguide end face in sample holders, used in our laboratory. For thinner mirrors more precise adjustment is necessary.

To do a relative comparison of different dielectric mirrors, available for a building up of MIR resonators, Fabry-Perot interferometer setup has been used (Fig. 5.7). Each set of mirrors has been integrated and transmission versus change of the optical cavity length was measured. According to Eq. 5.6 finesse and correspondent reflectivity at 3394 nm for different sets of mirrors was calculated.

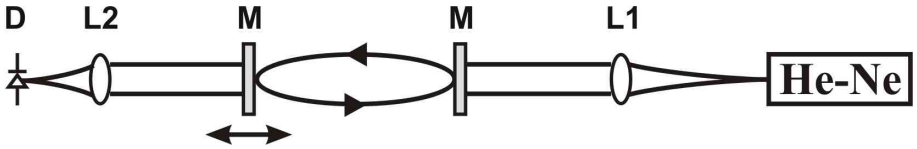


**Figure 5.7:** Experimental setup for finesse measurements using Fabry-Perot interferometer: HeNe - helium-neon laser at 3394 nm; L1, L2 - $CaF_2$ lens (f = 8.3 mm); M - mirror; D - HgCdTe detector.

The experiment has been done with commercial mirrors; with „home - made“ mirrors with 12 layers of $SiO_2/TiO_2$ deposition on a sapphire substrate (high polishing quality) of the same dimensions as the commercial one; 12 layers of $SiO_2/TiO_2$, deposited on $LiNbO_3$ substrate of 1 mm thick (without additional high quality surface polishing) and 10 layers of $SiO_2/Ta_2O_5$, also deposited on 1 mm thick $LiNbO_3$ substrate. Achieved results are shown in the table 5.1.

| Mirror | Substrate | Finesse | Reflectivity [%] | |
|---|---|---|---|---|
| | | Measured | Measured | Expected[a] |
| Commercial $SiO_2/Ta_2O_5$ | Sapphire | 57.0 | 97.2 | 97.0 |
| „Home - made“ $SiO_2/TiO_2$ | Sapphire | 62.5 | 97.5 | 96.7 |
| $SiO_2/TiO_2$ | $LiNbO_3$ | 12.2 | 87.5 | 97.3 |
| $SiO_2/Ta_2O_5$ | $LiNbO_3$ | 8.2 | 82.6 | 92.2 |

[a]Measured by the spectrometer

**Table 5.1:** Finesse measurements for different mirrors using a Fabry-Perot interferometer.

Sputtered commercial mirrors and deposited on a sapphire substrate[8] and „home - made“ mirrors (HR-MIR) are showing similar results. Minor changes can be explained

[8]wedge $< 5$ min

by a small inaccuracy of the measurements. Dielectric layers, deposited on 1 mm $LiNbO_3$ substrate are showing a very low finesse in comparison with the mirrors on the sapphire substrate. The reason might be a low surface quality of the substrate on one hand, and parallel surfaces of the substrate might result in undesirable back reflection of the light on the other.

As a conclusion, both coatings: commercial and „home - made“ are showing similar spectral properties and are the good candidates for the DR-OPOs. The substrate and its surface roughness are very critical in this case. Mirrors, deposited in our group, may also be used for an OPO, if substrate of a good surface polishing would be used.

### 5.3.2 Counter-Sample Approach

One disadvantage of the deposited mirrors, which has been already mentioned, is not a flat mirror surface at the sample edge, where the waveguides are located (Fig. 5.8 left). This is quite critical, especially for this wavelength range, where each dielectric layer is about 300 to 500 nm thick, depending on the material, which has been used[9]. For the near infrared this problem is not that strong: if the mirror has to have a high reflection at $\frac{1550}{2} = 775$ nm, then each layer (and overall thickness) will be already four times thinner.

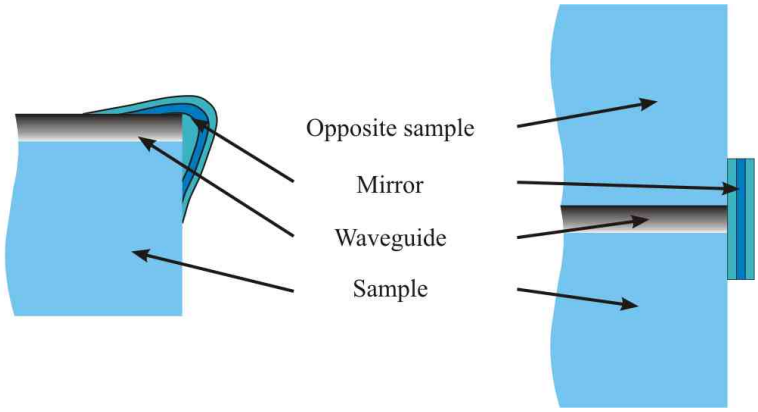


**Figure 5.8:** Schematic representation of the multilayer profile near the sample edge (left) and using a counter sample approach (right).

It has also to be taken into account, that MIR waveguides are larger and therefore a good mirror quality has to be provided for a larger area than for the NIR waveguides.

Directly deposited MIR mirrors have shown always worse characteristics as external ones (see chapter 5.3.1). Above mentioned problem on one hand may reduce the guiding inside the waveguide due to the periodic changes of the index of refraction of the single layer rests, deposited on the top of the waveguide (not the end face), on the other hand - curved mirror surface makes the coupling into the waveguide less efficient.

[9]Main application in our group has found deposition of $SiO_2$ and $TiO_2$.

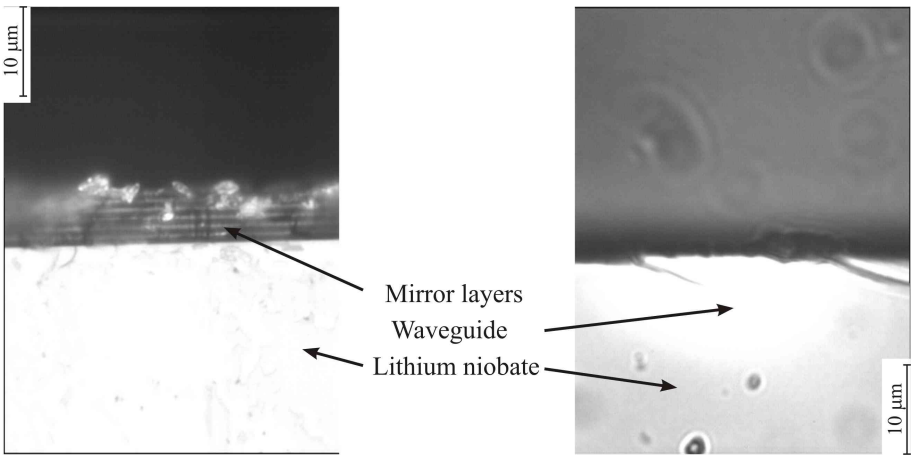


**Figure 5.9:** Top view of the multilayer dielectric mirror near the sample edge (left); the side view after removing the counter-sample (right).

As a possible solution getting a flat mirror surface may be the usage of the counter sample. To do this, the original sample with two small counter pieces of lithium niobate (with the same crystal orientation), located close to the edge, was fixed in a special sample holder and the end surfaces were repolished again being prepared for the further mirror deposition. Afterwards, mirrors have been deposited (Fig. 5.8 right). Later, both small pieces have been carefully removed and finesse measurements were done again.

Using the counter-sample approach no improvements have been observed. The measured finesse values show the same results[10] as without any counter-parts (in some cases even worse results). By investigating the sample surface under the microscope a lot of small mirror particles have been seen along the whole sample edge (Fig. 5.9 left). Also after removing the mirror, the end faces of some waveguides showed some damage (Fig. 5.9 right). To avoid this, as a next step was trying not to remove the counter-parts at all from the sample and repeat finesse measurements again to check, whether the mirror damages and layer particles were the reason for the bad results. For this purpose the sample of the length of 90 mm has been coated (before coating losses were below 0.1 dB/cm), left in the sample holder and the finesse was measured. A value of 4 has been observed.

After removing the counter-sample a finesse of factor 2 larger was observed, which is better than with counter-part. Better wave guiding condition might be the reason for this improvement. But these results still does not approach the calculated value.

As a conclusion, deposited mirrors for the MIR are remaining the crucial problem for the integrated OPOs. Dummy counter-sample as the one part of the same length as main sample, or as two shorter separated parts near the waveguide end face did not show any comparable or even better results than external commercial mirrors. On the other hand, output power characteristics of the OPOs with deposited mirrors is

[10]Finesse 4-9. Theoretically expected up to 27, depending on the losses.

comparable with calculated one, as it will be shown later. Deposited mirrors have a high advantage for the high temperature applications, where the homogeneous temperature profile in the waveguide is necessary. Using external mirrors it is difficult to realize flexibility in the mirror adjustment and good temperature isolation of the sample oven and mirrors from the environment.

### 5.3.3 Cavity Characterization

The same samples as for OPGs can be used to develop DROs. In this case end face polishing has to be checked once again and, if necessary, repolished again, while the device characteristics are strongly dependent on the cavity quality due to the multipath of the resonant wave in the cavity in comparison with OPGs.

Losses in the waveguides are measured by the same method, as described before.

The cavity is formed with external or deposited mirrors and finesse measurements have to be carried out. The setup, similar to Fig. 5.7 is used. For coupling a $CaF_2$ lens (f = 16.99 mm) is used. A tilted neutral density filter is installed between the pump laser and the coupling lens to avoid undesirable Fabry-Perot effects outside the optical cavity. For finesse measurements a He-Ne laser at 3394 nm has been used. The optical cavity length was changed by changing the temperature of the sample. Characteristic transmission versus temperature (equal to the path change) in the waveguide is shown in Fig. 5.10. Four main peaks are clearly observed. The sample has been heated up in

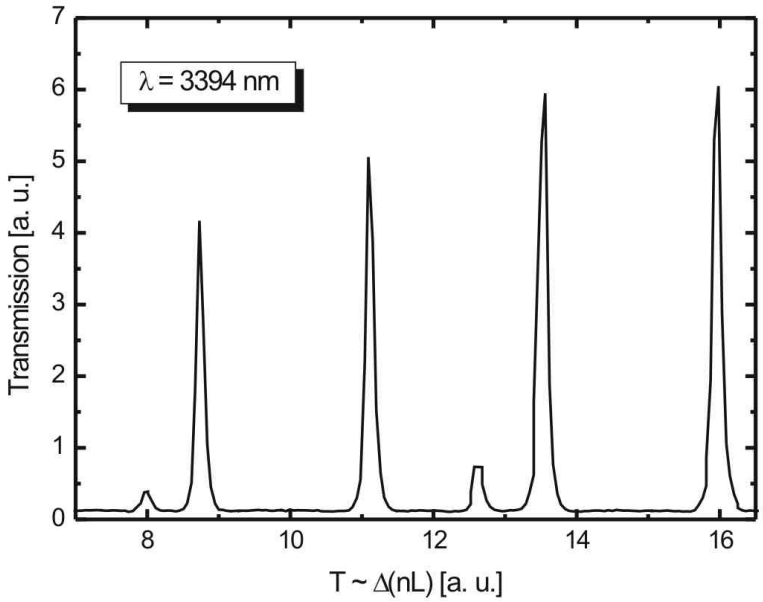


**Figure 5.10:** Experimental results for finesse measurements using external mirrors: L = 68 mm; $\alpha$ = 0.062 dB/cm; TM - polarized light.

the temperature range 24 - 30 ℃. For sufficient and proper peak resolution slow and linear temperature increase is necessary.

Besides the main peaks two additional peaks appear behind every second main peak. They belong to the TE-polarization of the light. This polarization component is very small in comparison with TM and could appear due to the imperfect orientation of the sapphire [11] substrate of the mirrors.

All peaks have a slightly different height. This effect is probably due to a small misalignment between the coupling lens and the waveguide, induced by the temperature change in the waveguide. This might be avoided, if the wavelength change would be used instead of the heating.

For this experiment a finesse of about 23.6 has been measured. According to the mirror reflectivity of 97.2 % finesse of 25.1 should be obtained. The small discrepancy between those results might arise from unperfect meusurements.

### 5.3.4 Power Characteristics

To measure the dependence of MIR signal and idler power versus pump power the setup similar to Fig. 4.2 has been used. The pump has been coupled into the sample using a free space optics. Behind the sample a plane germanium filter was set to block unused pump power. The generated MIR radiation was focused by a $CaF_2$ lens (f = 8.3 mm) on a liquid nitrogen cooled InSb detector[12].

Sample of the length 89.5 mm has been coated by 12 $SiO_2/TiO_2$ layers having the peak reflectivity at 3000 nm. Finesse measurements afterwords are showing results in the range from 8 to 10, which is laying close to the theoretically expected 10 to 13. The same reasons as described above can be implemented here to explain the discrepancy.

Experimetal and theoretical results are presented in Fig. 5.11. For power levels well above the threshold a very good agreement between theoretical and experimental results is observed. The calculated threshold is about 45 mW; the measured result (see Fig. 5.11) is 150 mW. Abrupt jumps in the power characteristics may come from small power or polarization fluctuations of the pump near the threshold. Generation of stable MIR radiation was observed for the pump power levels well above the threshold.

In addition, if some pump wavelength fluctuations happen, then *mode hopping* can drop the power levels. This might be described as follows (see Fig. 5.12). The couple of signal and idler wavelengths in the simple OPG is determined by the energy and momentum conservation, as it has been mentioned before. By continuous tuning of the pump wavelength the two output wavelengths will be determined according to those conservations. Low reflectivities at the end surface can be neglected. But if the reflectivity is high enough (like in the case of an OPO), then only the discrete values

[11] Sapphire is a birefringent material

[12] HgCdTe detector in combination with preamplifier and lock-in technique has been used to measure low intensity signals in the range up to several $\mu$W. Signals of higher powers are saturating the detector. An InSb detector allows to do the measurements in the range of several mW.

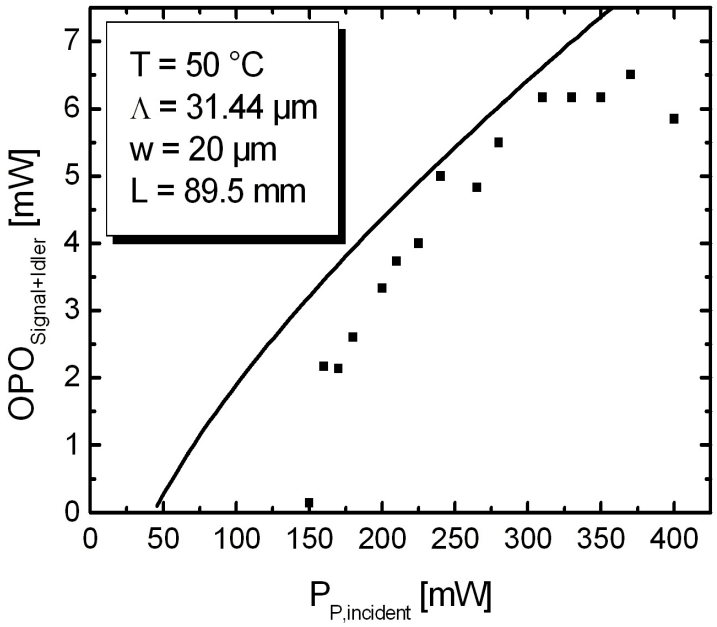


**Figure 5.11:** Theoretical (solid line) and experimental results (dots) power characteristics for the DRO using directly deposited on the end surface mirrors: L = 89.5 mm; T = 50℃; $\Lambda$ = 31.44 $\mu$m; w = 20 $\mu$m; $\lambda_p$ = 1550 nm; $\lambda_s$ = 2919 nm; $\lambda_i$ = 3277 nm.

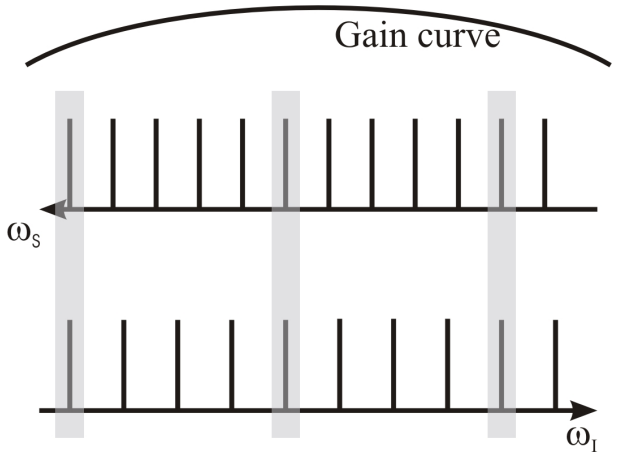


**Figure 5.12:** Schematic representation of the tunability of DRO.

of cavity modes are possible (see Fabry-Perot resonator). That means that continuous tuning of the pump wavelength in the simplest case will lead to the jumps at the output wavelengths. In case of a doubly resonant device the cavity length has to be a multiple number of the of the wavelength for both signal and idler simultaneously. Therefore, oscillations will happen only for the wavelength under the gain curve and only for the couple of signal and idler, where this condition is fulfilled for both wavelengths (shown as gray boxes in the figure).

## 5.4 Synchronously Pumped IOPOs

### 5.4.1 Introduction

Integrated OPOs were already demonstrated as promising devices for spectroscopic applications. As it has been shown, by pumping such devices with up to 1.5 - 2 W in cw-regime, a MIR power of several mW is possible to obtain. Pulsed pump sources instead would generate even higher peak power levels at the same average powers. Such pulsed OPOs [83–87] might be used for time-resolved spectroscopic applications [88–90]. Due to the absorption band of lithium niobate starting near 4 $\mu$m, there is not possible to have a resonant wave behind this wavelength because of the round trip losses. Increasing the pump power level would allow to get desirable radiation at these wavelengths as well [91].

If an OPO is pumped periodically by short pulses - shorter than the round trip time within the cavity - short signal and idler pulses are generated and resonantly amplified after each round trip. This mode of operation is called synchronous pumping, applicable to Singly Resonant SR-OPOs as well as to Doubly Resonant DR-OPOs. The conversion efficiency and therefore the output power level depend on the type of OPO used (SR or DR).

Precondition is that the reciprocal pump pulse repetition frequency $f$ is equal to the round trip time $T$ of the resonant pulses in the cavity. It can also be a multiple $N$ of the reciprocal repetition frequency generating in this way $N$ pulses propagating simultaneously in the cavity:

$$T = N\frac{1}{f} \tag{5.7}$$

This definition of synchronization works very well for SR-OPOs, where only one wave is resonant and its round trip time might be easily synchronized to the interval between two pump pulses. In case of DROs such a definition is not evident due to the dispersion properties of the crystal. Here two generated waves have different group velocities and synchronization might be fulfilled either for one or the other wave or none of the waves will be synchronized.

Due to the lower threshold power of DROs they have been investigated first. In this case under synchronization has been meant equality between reciprocal pump pulse repetition frequency $f$ and the mean value of round trip times for signal and

idler, determined by the group velocities:

$$\frac{T_S + T_I}{2} = N\frac{1}{f} \tag{5.8}$$

For the degeneracy point Eq. 5.8 became the form 5.7.

### 5.4.2 Sample Design

To be able to realize synchronous pumping a sample of precise length has to be fabricated. This can be done, if the optical properties of the material are known precisely. Lithium Niobate is a uniaxial negative [13] crystal with normal dispersion [14]. Ordinary and extraordinary index of refraction can be calculated using Sellmeier equations [92, 93]. Those equations are permanently corrected by different experiments and latest improvement for periodically poled LN crystal using mid-infrared DFG can be found in [94]. Indices of refraction and group indices for T = 40 ℃ are shown in Fig. 5.13, taken from [92, 94].

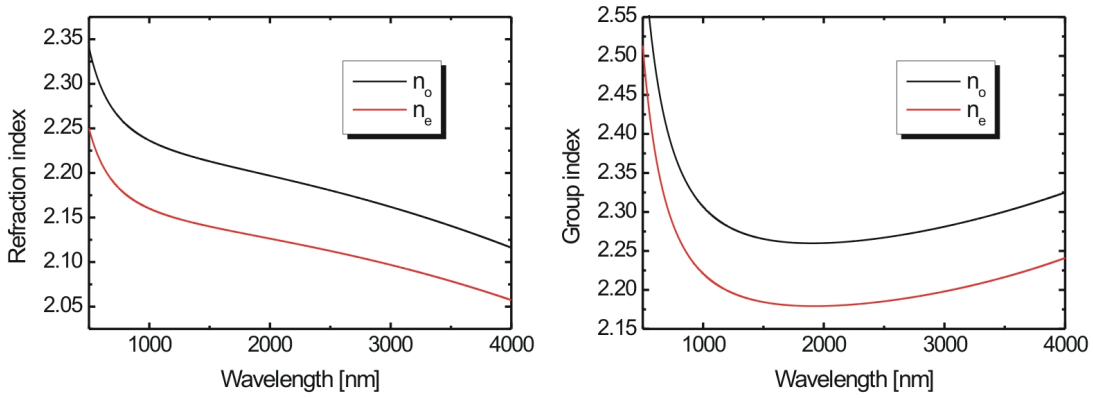


**Figure 5.13:** Extraordinary and ordinary index of refraction (left) versus the wavelength; correspondent group indices versus the wavelength(right).

The group index $n_g$ can be calculated directly from the index of refraction $n$ using the following relation:

$$n_g(\lambda_0) = n\left(\lambda_0\right) - \lambda_0 \left.\frac{\partial n}{\partial \lambda}\right|_{\lambda=\lambda_0} \tag{5.9}$$

From here the sample length for synchronous pumping can be defined. The group velocity for $\lambda_s = 2900\,\text{nm}$ is obtained by:

$$v_{g,2900} = \frac{c}{n_g} = \frac{3\times 10^8}{2.179} \approx 1.3768 \times 10^8\, m/s \tag{5.10}$$

[13] $n_e < n_o$

[14] $\frac{\partial n}{\partial \lambda} < 0$; for the anamolous dispersion will be $\frac{\partial n}{\partial \lambda} > 0$

where $c$ is the speed of light in vacuum and $n_g$ - group index. The necessary sample length for the pump repetition rate of 10 GHz will be:

$$L = \upsilon_{g,2900} \cdot T_S = 1.3768 \times 10^8 \cdot 100 \times 10^{-12} \approx 0.0136\, m \tag{5.11}$$

with $T_S$ - round trip time for the signal wave (equal to the reciprocal repetition rate of the MLL). By traveling forth and back the sample length for this particular wavelength at T = 40 ℃ should be 0.68 cm. If 10 pulses will be traveling inside the cavity simultaneously then a sample of a length of 6.8 cm is necessary. Round trip time matching for other temperatures and wavelengths for a fixed sample length might be realized by changing the repetition rate of the laser.

The dispersion of the round trip time for a sample of a length of 6.8 cm is shown in Fig. 5.14. Arrows are showing the times for a set of three particular wavelengths. Near 1900 nm this curve has a minimum. In other words, this will be the fastest propagating wave. Pump, signal and idler are traveling with a bit different to each other velocity, which is not much different. The following relation holds:

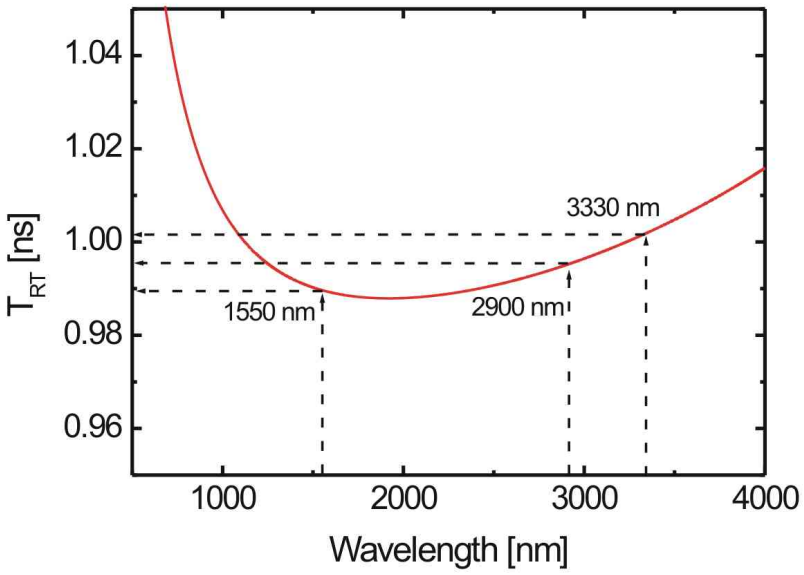


**Figure 5.14:** Calculated round trip time for TM-polarized light and the sample length L = 6.8 cm versus wavelength.

$$\upsilon_p > \upsilon_s > \upsilon_i \tag{5.12}$$

Pump pulse in the range of interest ($1520 < \lambda_p < 1620$ nm) is always faster, than the generated signal and idler pulses. This has a consequence, that even in the nonsynchronous case, when pump pulse will be injected into the crystal a bit later, than the

generated pulses start to travel from the sample end, generated signals will produce even higher gain, than exact matched pumping. This happens, while the pump pulse has to overtake signal and idler pulses [54].

For the synchronously pumped OPOs samples of the exact length have to be fabricated. Fabrication process and sample characterization for these samples is similar to another MIR samples, having the same domain periodicity ($31.10 < \Lambda < 31.60$ $\mu$m) and waveguide width (18, 20, 22 $\mu$m).

Propagation losses have been calculated by measuring the transmission versus change of the optical length in the waveguide, as described before. They are below 0.1 dB/cm.

### 5.4.3 Experimental Setup

The sample of the precise length of 6.8 cm has been fabricated. Measured propagation losses at $\lambda = 3394$ nm are below 0.1 dB/cm. External dielectric mirrors (for DRO) have been clamped to the end surface of the waveguide (Fig. 5.15 right). Finesse measurements are showing values up to 20, in good agreement with expected values, calculated according to the waveguide losses and mirror reflectivity at this wavelength (Fig. 5.15 left).

The experimental setup for the synchronously pumped DR-OPO is shown in Fig. 5.16. The MLL was operated in the wavelength range $1536.9 < \lambda_p < 1563$ nm. The repetition rate has been adjusted to be synchronized with signal wave, according to the calculations of the round trip time, described above. The pump pulses were controlled in time and frequency domains using a fast oscilloscope and an optical spectrum analyzer. The MLL pulses were boosted by the EDFA; TM polarization has been set to utilize $d_{33}$ coefficient.

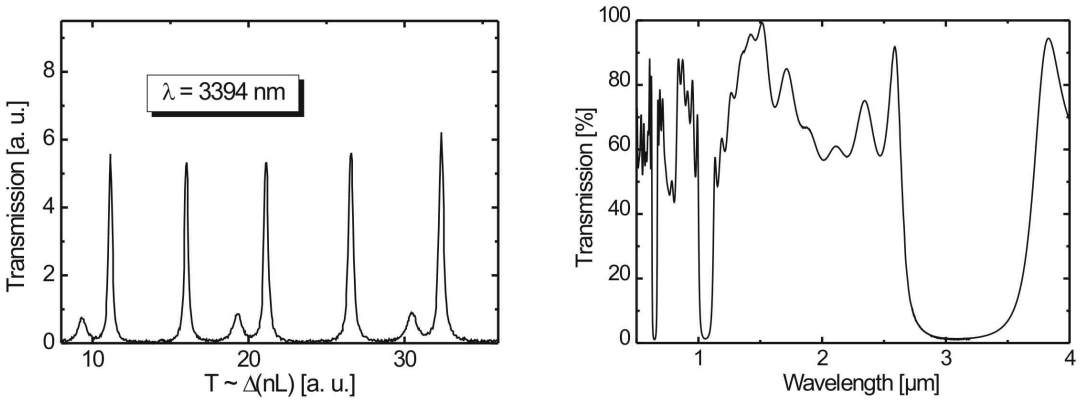


**Figure 5.15:** Transmission of the synchronously pumped OPO with external dielectric mirrors versus change of the optical cavity length (left); transmission of HR mirrors for DR-OPOs versus wavelength taken by transmission (up to 3.2 $\mu$m) and Fourier (3.2 - 5 $\mu$m) spectrometers (right).

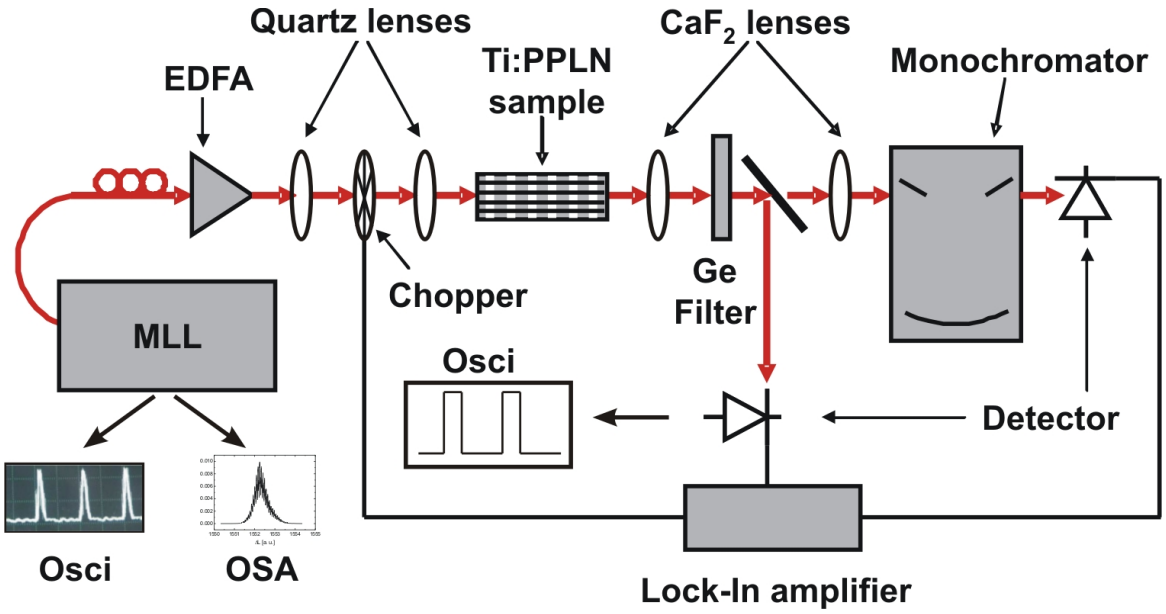


**Figure 5.16:** Schematic diagram of the experimental setup for the synchronously pumped DR-OPO.

A fraction of the generated output MIR radiation has been constantly monitored with a InSb detector and a fast oscilloscope. The other one has been coupled via a $CaF_2$ lens (f = 25 mm) to the monochromator. The slits of the monochromator have a width of 50 $\mu$m, which corresponds to a spectral resolution of the device of about 2 nm. HgCdTe detector has been placed directly behind the output slit of the monochromator.

### 5.4.4 Tuning Characteristics

The measured tuning characteristics of the synchronously pumped OPO is presented in Fig. 5.17 together with theoretical results. The signal has been observed in the range from 2700 to 2800 nm, and the idler about 3600 nm by the continuous tuning the pump wavelength from 1539 to 1563 nm. Measured and calculated results are in the good agreement.

The measured spectra for signal and idler wavelengths are shown in Fig. 5.18. The linewidth of the generated emission is in the range from 2 - 7.4 nm. Idler pulses are larger than signal in the frequency domain. Nonsymmetrical slope at signal wavelength is observed and clearly depicted at idler wavelength, what should have a consequences of the dispersion in the material. Calculated results for the same parameters are also shown in Fig. 5.18. Measured spectral characteristics of the signal is with a very good agreement with the theory. The spectrum of the idler is more complicated and has two neighboring peaks. This happens, while the frequency of the MLL is synchronized with

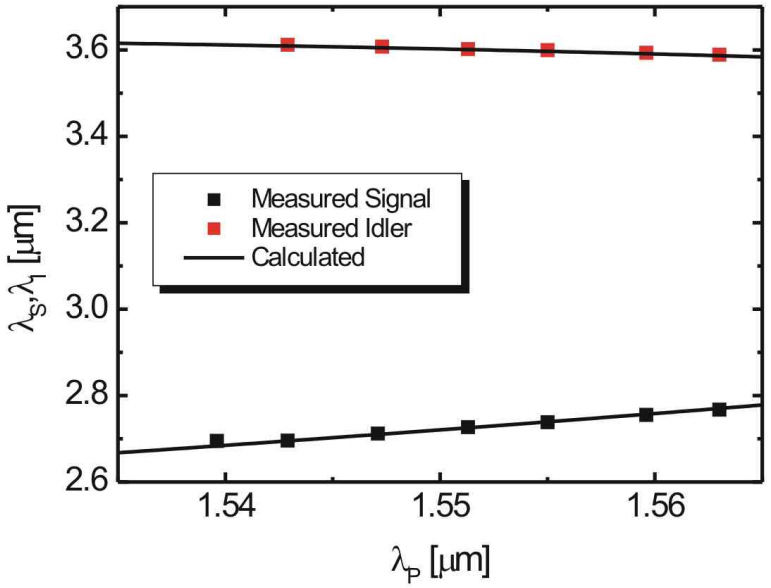


**Figure 5.17:** Measured (dots) and calculated (solid) tuning characteristics of a synchronously pumped DR-OPO as signal and idler wavelengths versus the pump wavelength: L = 68 mm; T = 40 °C; Λ = 31.10 $\mu$m; w = 18 $\mu$m.

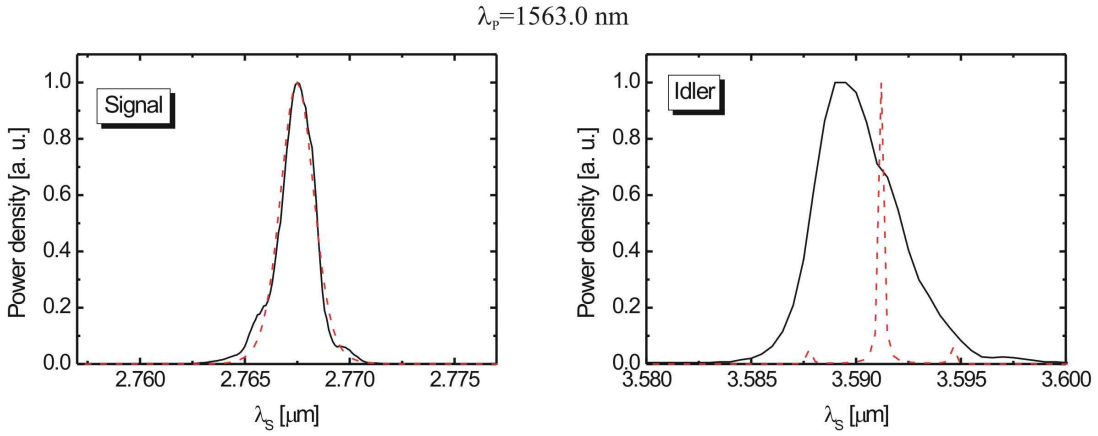


**Figure 5.18:** Measured (solid line) and calculated (dashed line) signal and idler spectra as examples for operation with the pump wavelengths 1563.0 nm. Parameters: L = 68 mm; T = 40 °C; Λ = 31.10 $\mu$m; w = 18 $\mu$m.

the signal[15]. Idler pulse after one round trip will be delayed relative to the signal pulse, according to the dispersion. Therefore several idler pulses will travel simultaneously. Those results will also be reflected on the idler pulse shape (see chapter 5.4.7). The neighboring peaks cannot be resolved with the monochromator. But the measured envelope of the idler spectrum and the separation between calculated neighboring peaks are equivalent.

### 5.4.5 Temporal Detuning Characteristics

One important characteristics of such type of devices is the so called *temporal detuning*, or change of the temporal interval between two pump pulses relative to the round trip time of the generated MIR pulses, which leads to a change in the OPO output power.

The experimental setup for these measurements is similar to the one, described to measure the spectral properties. The whole generated MIR power was collected by an InSb detector. Detuning has been realized by changing the modulation frequency of the mode-locked laser in the range 8.98553 - 10.00753 GHz, that corresponds to a time interval between two pump pulses of 99.9 - 111.2 psec. Such relative large interval is selected due to the large separation between signal and idler wavelengths for this particular configuration (see Fig. 5.17).

The experiment has been realized in the following manner: above mentioned frequency was set; parameters of the MLL were adjusted to generate optimized pump pulses (in this case $\lambda_p = 1552.20\,\text{nm}$ and spectral width of 0.7 nm) afterwords polarization was checked again and generated MIR power was measured. The whole procedure was repeated for another frequency.

The experimental results, together with appropriate calculations are shown in Fig. 5.19. The two peaks in the figure correspond to the condition, where the propagation of the pump pulse starts simultaneously with the signal (left) or the idler (right) pulse. The minimum in the middle, where pump pulses are synchronized neither with signal nor idler pulses (see the definition of the synchronization). If the point of operation would be selected close to the degeneracy, then two peaks will approach *zero detuning* point[16], finally combine in one peak.

According to the dispersion properties of lithium niobate (see Fig. 5.14) after one round trip the delay between signal and idler at these wavelengths will be about 11 psec, what is also nicely observed in experiment. Experimental results have proofed theoretical calculations and two synchronization regimes for signal and idler are clearly observed. The measured FWHM of the peak is 0.2 psec, that corresponds to changes of about 16.2 MHz in the frequency region of the MLL.

The average incident pump power level was about 1.2 W, resulting in a maximum pulse energy of 120 pJ. The calculated characteristics has as maximum pump energy of only 10 pJ[17]. Factor 12 larger powers might lead to peak narrowing.

[15] For detailed explanation see [54]

[16] see Fig. 5.20

[17] SynchOPO - program to calculate power- spectral- and time properties of integrated OPOs (created by Dr. W. Grundkötter)

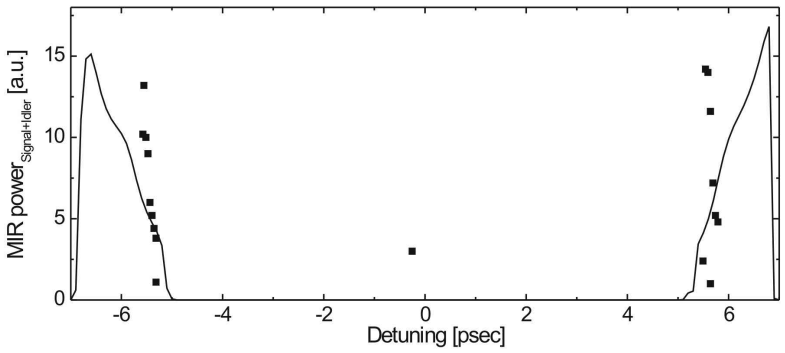


**Figure 5.19:** Calculated (solid line) and experimental (dots) power characteristics of a synchronously pumped DR-OPO with external mirrors as MIR output power versus temporal interval of pump pulses adjusted by the repetition rate of the mode locked pump laser: L = 68 mm; T = 40 °C; $\Lambda$ = 31.10 $\mu$m; w = 18 $\mu$m; $\lambda_p$ = 1552.20 nm; $\lambda_s$ = 2723 nm; $\lambda_i$ = 3608 nm.

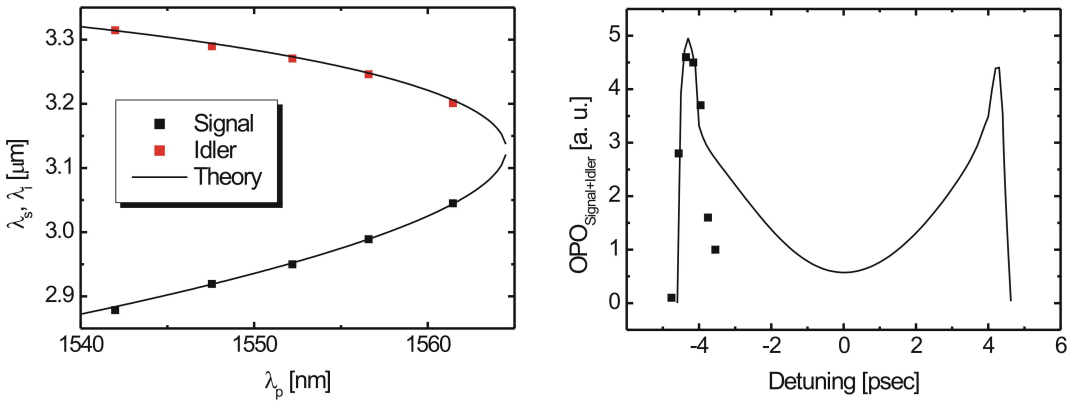


**Figure 5.20:** Measured (dots) and calculated (solid line) tuning characteristics of a synchronously pumped DR-OPO as signal and idler wavelengths versus the pump wavelength (left); calculated (solid line) and experimental (dots) power characteristics of a synchronously pumped DR-OPO with external mirrors as MIR output power versus temporal interval of pump pulses adjusted by the repetition rate of the mode locked pump laser (right): L = 68 mm; T = 40 °C; $\lambda_p$ = 1552.20 nm; $\lambda_s$ = 2948.1 nm; $\lambda_i$ = 3267.8 nm (relevant to the right diagram).

Additionally, OPO oscillation near detuning $\approx 0$ has also been observed and cannot be described according to the calculations of the detuning curve.

The other sample with the periodic polling from $31.20 < \Lambda < 31.60$ $\mu$m has been fabricated. The higher periodicity will allow to have for the signal and idler smaller group velocity mismatch. Phase matching and detuning characteristics are shown for this sample in Fig. 5.20.

Due to the smaller GVM the calculations are showing a generation of the MIR radiation in the whole range of 9 psec between the signal and idler peaks. In this case the theoretical power characteristics does not go down to zero and the MIR radiation will be generated even for non ideal synchronization. Experimentally, the power characteristics near the peak, where the signal round trip time matched to the pump pulses, has been investigated. The width of this characteristics is with a good agreement with the theory. The same results are expected for the synchronization with the idler.

### 5.4.6 Power Characteristics

The output power properties of the synchronously pumped DR-OPO has also been investigated. In this case an experimental setup similar to that of Fig. 5.16 has been used. The generated MIR radiation was collected by one $CaF_2$ lens on liquid nitrogen cooled InSb detector. Measured and calculated results are shown in Fig. 5.21 for comparison. Optical parametric oscillation has been observed above a threshold of about 80 mW coupled average power with pulse length 6.4 psec at $\lambda_p = 1552.20\,\text{nm}$. Above 400 mW of the average pump power a MIR output power of more than 10 mW (average) was generated.

Theoretical calculations (Fig. 5.21 right) predict a lower threshold of only 62 mW and even higher output power levels by taking into account the same duty cycle for MIR radiations as for the pump.

Despite experimental and theoretical results have the same threshold, such relative large discrepancy in the results might come from non ideal parameters match to generate pulses, which are really synchronized with the pump pulses. The laser setup does not allow to continuously change one parameter (for example, pump wavelength) without additional adjustment of other parameters like, polarization, pulse shape and modulation frequency. Taking into account very sensitive detuning characteristics (see Fig. 5.20) it might be possible that the condition to generate the maximum output power according to the calculated dispersion characteristics was not achieved.

Stable operation of such devices is expected for pump power levels significantly above the threshold. Any minor fluctuations of any parameter in the pump chain will result in dramatic changes in the output power levels of the IOPO. As well as proper mechanical and thermal insulation of the experimental setup from the surroundings.

In the insets of Fig. 5.21 (right) pump, signal and idler pulses after one round trip are shown. Due to the properties of lithium niobate at these wavelengths (low dispersion) Gaussian shape of the pump pulse will almost remain without any changes and be transmitted to signal and idler according to the calculations. This allows

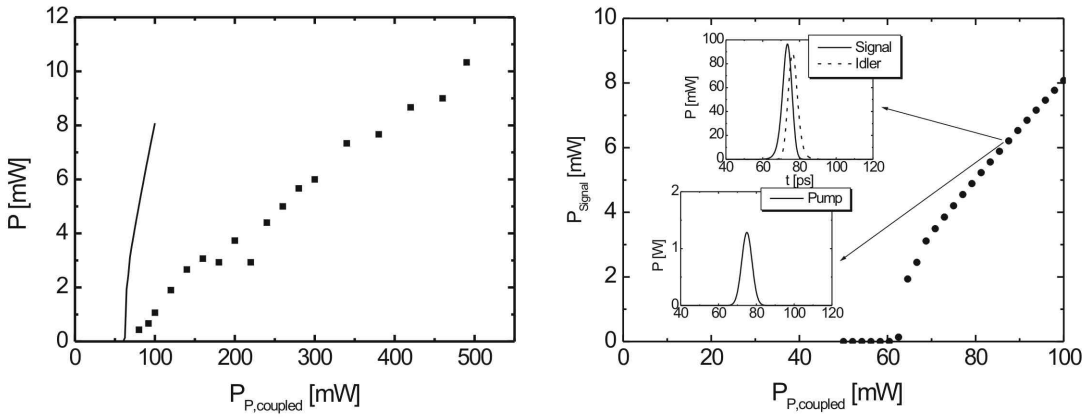


**Figure 5.21:** Measured (dots) and calculated (solid line) power characteristics of the synchronously pumped integrated OPO as average MIR output power versus average pump power (left); calculated power characteristics with output pulses of pump, signal and idler given in the insets (right): L = 68 mm; T = 40 ℃; $\Lambda$ = 31.44 $\mu$m; w = 18 $\mu$m; $\lambda_p$ = 1552.20 nm; $\lambda_s$ = 2948 nm; $\lambda_i$ = 3268 nm; f = 9.956408 GHz.

us to assume, that the generated pulses will also have almost the same duty cycle. Pulse energy of the generated MIR radiation are calculated by taking into account low dispersion.

### 5.4.7 Autocorrelation Function of MIR Pulses

To have a full information about the generated MIR pulses measurements in the time domain are also necessary. While fast MIR detectors are not available, measurements of the autocorrelation function remains at the moment the only possible solution[18].

The schematic diagram of the autocorrelator for the measurements of the generated MIR pulses is shown in Fig. 5.22. The collimated beam (red line) from the OPO is reflected by the coupling mirror $M$ on the beam splitter $BS$. A part of the radiation is reflected on the fixed retroreflector $R1$. The other part is transmitted through the beam splitter and achieves the movable in the direction of the beam propagation retroreflector $R2$. The MIR pulse in this arm can be delayed relative to the pulse of the other arm. Reflected pulses go once again through the beam splitter $BS$ parallel (noncoaxial case)[19] and the same way (coaxial case) towards the nonlinear crystal $C$. The transparent in the MIR Lithium-Gallium-Selenide crystal is placed in the holder, which can be rotated to achieve a phase matching. The generated SHG signal (green line) is focused on the detector $D$.

For this measurements a setup similar to Fig. 5.16 has been built up. A generated MIR signal has been collimated with a $CaF_2$ lens in front of the input mirror of the

[18]Upconversion of generated MIR pulses would be also possible.

[19]Shown in the Fig. 5.22

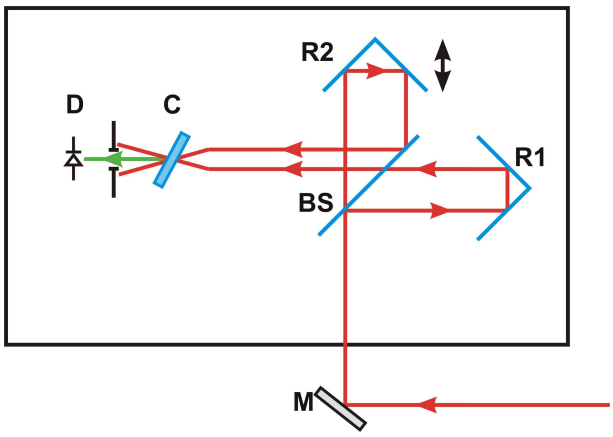


**Figure 5.22:** Schematic diagram of the autocorrelator: M - coupling mirror; BS - beam splitter; R1 - retroreflector; R2 - movable retroreflector; C - LiGaSe crystal; D - detector.

autocorrelator.

The frequency of MLL has been adjusted according to the detuning curve (Fig. 5.20) to measure the MIR pulses at the peak of the signal. The scan range of the autocorrelator was 50 ps. Measured results for the signal and idler pulses together with fitted gaussian distributions at the point of operation, where the temporal interval between two pump pulses is equal to the signal round trip time, are shown in Fig.5.23.

A multipeak structure of the autocorrelation function of the idler pulse is clearly observed. This means, that a more complicated pulse structure has to be taken into account. Thus, at least two idler pulses, traveling close to each other, are involved in the interaction. Similar multipeak structure has been also observed for the signal pulse, though the detection efficiency in this case is lower. Therefore, fitting the gaussian distribution to calculate the pulse width and the duty cycle may give only approximate results to compare them with the theory. For the central peak of the idler an evaluated width of about 0.6 ps has been measured. For the envelope it gives 9.8 ps. Complicated idler structure for the signal synchronization has already been predicted in [54] and now got the experimental proof. The origin of this behavior can be easily understood: after one round trip the signal and idler pulses will be separated according to the dispersion. During the next round trip a new idler pulse will be generated and the previous one attenuated because of the losses and so on.

The nonsymmetrical background of the signal pulse comes from the autocorrelator itself, where the detection efficiency is lower. Anyway, a width of the signal central peak of 3.7 ps has been measured. Similar multipeak structure for the signal pulse may be also observed.

Autocorrelation functions have also been taken near the maximum of the signal power (see Fig. 5.20) in the frequency range 9.956644 - 9.968644 GHz. No significant pulse broadening or narrowing has been observed.

To see an influence of the detuning on the MIR pulses, the round trip time of the pump pulses has been changed to get zero detuning (see Fig. 5.20). Measured results

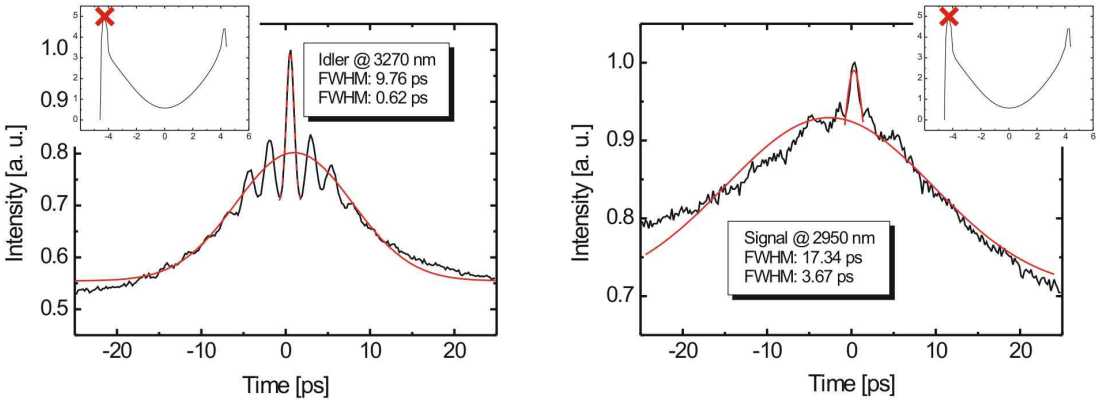


**Figure 5.23:** Measured autocorrelation function for the idler (left) and the signal (right) together with the fitted gaussian profile at the point, where the MLL is synchronized with the signal (see insets). Parameters: L = 68 mm; T = 40 ℃; $\lambda_p$ = 1552.20 nm; $\lambda_s$ = 2950 nm; $\lambda_i$ = 3270 nm; $f_{MLL}$ = 9.968644 GHz.

together with the fitted gaussian distribution are shown in Fig. 5.24. Neighbouring peaks for the idler as well as for the signal are also observed. The width of the central peaks were 1.86 and 3.17 ps for idler and signal respectively. The peak envelope narrowing is observed. In this case the new pump pulse will not start propagating together with the signal pulse, but behind the signal pulse. It has to overtake the signal pulse and therefore the interaction length will be large. Because of the energy conservation this will also impact the idler pulse. A higher efficiency for the desynchronization of the pump and generated MIR pulses has also been reported in [54].

For the first time MIR pulses, generated in TI:PPLN waveguides, have been investigated experimentally. The calculated complicated idler pulse form was also observed by the experiment. Further investigations for the complete description and influence of the different factors on the pulse shape are necessary.

## 5.5 Conclusion

A family of doubly resonant integrated optical parametric oscillators has been reviewed. Devices have been characterized with external and deposited dielectric mirrors. For the first time integrated OPOs with deposited mirrors has been presented. By showing the same experimental and theoretical results for the powers above the threshold they are comparable and integrated OPOs with deposited mirrors are preferable candidates to realize compact devices for spectroscopic applications. Overall threshold power in this case is still higher than for external mirrors, which are made by the spattering technique in comparison with deposition on our equipment. As it has been mentioned above, near the threshold minor changes in the stand of the pump will be

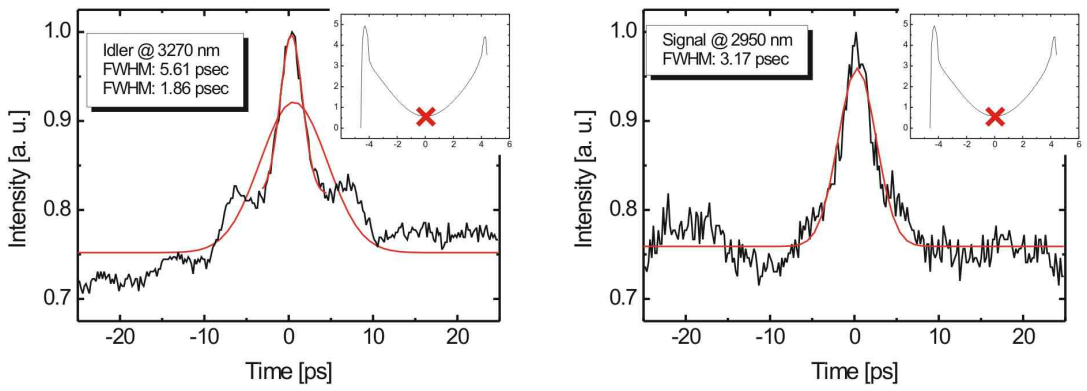


**Figure 5.24:** Measured autocorrelation function for the idler (left) and the signal (right) together with the fitted gaussian profile at zero detuning point (see insets). Parameters: L = 68 mm; T = 40 ℃; $\lambda_p$ = 1552.20 nm; $\lambda_s$ = 2950 nm; $\lambda_i$ = 3270 nm; $f_{MLL}$ = 10.416666 GHz.

right now observed in the generation of MIR radiation. But if sufficient pump power is provided then stable output power is observed.

Even if deposited mirrors have the same transmitting properties (or in some cases even better) as the mirrors from the company in the wavelength of interest, with a time adhesion of separate layers did not allow to utilize these devices very long period of time (weeks) without worsening the optical properties and as a consequences - power characteristics.

For MIR mirrors all the time in the separate layers some bubbles-like defects have been observed. The origin of them is still unknown. Taking into account low dimensions of the waveguide, these defects might be responsible for the lack of generation of MIR signals in some waveguides.

Heating up the sample to the temperature above 100 - 150 ℃ should reduce an effect of photorefractive damage and in this way also improve an output signal. This is easy to realize with deposited mirrors, but above mentioned peeling of separate mirrors did not allow to do it.

The setup with external mirrors could not be operated at such high temperatures due to the construction of the mirror and sample holder. Temperature gradient from the middle towards the end of the sample would be in this case unavoidable, what will have an influence on the power and spectral properties of the integrated OPO.

Additionally, thick mirror stack (each layer of 300 to 500 $\mu$m thick and mirror has usually 8 to 12 layers) and not really plane at the edge of the sample, what is definitely critical for the resonator cavities and looking worser in compare with external plane mirrors. An attempt to improve the flatness of these mirrors have been reported. Due to the fabrication of such sandwich, where the end face surface has to be polished for both samples simultaneously, as a suggestion, particles of the polishing powder could penetrate between two lithium niobate pieces and land near the waveguide and

in this way cause worsening of the optical properties. If the opposite sample will be removed, than no good quality and sharp edge of the mirror is possible to obtain. The particles of the dielectric layers are reducing the optical properties of the mirror. Proper cleaning of the mirror surface is not possible without any mechanical damage of the mirror surface.

Additional stabilization of the bulk OPO using lock-in technique helps to provide constant output power of the device. At the moment this was not possible to realize in the integrated devices (discussion will take place in appendix).

For the first time integrated OPOs have been fully investigated in the time and frequency domains. Knowing the proper MIR pulse shape would allow to calculate precisely the peak power.

Despite of all mentioned reasons integrated OPOs in MIR are remaining high efficient and potential devices for different applications, mainly for (time resolved) spectroscopy, providing high power levels. Compact design and simple use with deposited mirrors make these devices preferable candidates in compare with bulk OPOs, where usually several mirrors have to be properly adjusted. High field confinement along the whole waveguide length and low losses allow to fabricate waveguides of a high quality and low threshold and in this way generate MIR radiation without any high power amplifiers.

Potential of the bent waveguide structure, showing very low losses for the waveguide length as double as for the straight waveguides makes use of them even more attractive for the further investigations.

# Chapter 6

# Conclusion and Outlook

## 6.1 Summary

Within the framework of this project the generation of the tunable coherent mid-infrared radiation in the wavelength range between 2 and 4 $\mu$m and fabrication of the compact and highly efficient optical parametric generators and oscillators has been described.

Low loss titanium indiffused waveguides provide the basement for the fabrication of above mentioned nonlinear devices. Losses for the straight waveguides of the maximum length about 95 mm (limited by 4 inch lithium niobate wafer) are going down to 0.03 dB/cm (more than 99.3 %/cm is transmitted) have been measured, showing an excellent guiding properties.

Bent waveguides, which can have twice the length of straight ones, have also been investigated. Their advantage is the possibility to increase the interaction length by a factor of two. The generated MIR radiation in above mentioned nonlinear processes is proportional to the squared interaction length and therefore at some point output radiation will be strongly increased by the minor change of the length. In such waveguides the limiting point is the bending loss, which happens due to the phase difference in the inner and outer part of the bent waveguide. If the bent radius is sufficiently large (larger than 30 mm), then such waveguides may be considered as the straight ones. Losses for the bent waveguide of the length of 18 cm were comparable here with the straight waveguides and are below 0.1 dB/cm.

Using the crowning technique [95] or depositing of the optical waveguide using the gradient concentration of titanium or using the ridge waveguides can solve this problem and reduce propagation losses even more. In this case a higher efficiency for the bent waveguide structure in comparison with the straight one can be expected.

2D mode distribution in the MIR waveguide at $\lambda = 3394$ nm for the first time has been directly measured by using correspondent MIR camera.

Initial point for the investigation of nonlinear devices for the MIR spectral range was Optical Parametric Generator, where the pump photon of high energy decays into two photons (namely signal and idler) of lower energy under the conditions of

conservation of energy and momentum.

Generation of signal and idler waves has been demonstrated in the continuously tunable wavelength range from 2.8 to 3.4 $\mu$m. Changing the temperature, domain periodicities and the pump wavelength enables the output wavelength tuning and extends this range to the whole transparency region of the material.

Using a cw pump laser spontaneous OPF of several nW after single pump pass was generated. If pulsed pumping with the MLL is used instead with the pulses of 6.4 ps pulse length and the peak power level up to 40 W, then transition from spontaneous to stimulated emission was clearly observed. In this case the output power dependence versus the input pump power is not linear any more and has a pronounced exponential rise. At an average power level of 1.4 - 1.5 W the generated MIR signal was than 2 times larger compared to cw-pumping at the same average power level.

If the output power of the continuous wave DFB laser is modulated, even with a relative low frequency in the range of 1 MHz and different duty cycles, then so called *quasi* cw regime is used. It can neither be considered as pulsed (due to relative long pulses up to 100 nsec), nor as cw (due to long time between two neighboring pulses) pumping. In this regime a clear transition to stimulated emission and generated power levels of more than 1 $\mu$W peak power have been shown.

The same slicing technique was applied with a mode locked laser as a pump source. Using a high frequency modulator it was possible to cut out every 8th, 16th or 32nd pulse from the pulse comb of the laser. Peak pump power levels of more than 600 W according to the average power and duty cycle were achieved. This allows to generate output signals of several watts after just one pump pass. These power levels are more than sufficient for spectroscopic applications in the laboratory, where usually several $\mu$W are necessary. Such high power levels were obtained without using of any resonator cavity and mirror adjustment, making these devices attractive for non-laboratory applications as well.

Limitations were nonlinear effects happening in the optical fiber and EDFA, which were not designed for high power and long idle time between single pulses, leading to disturbed pump pulses and therefore reduced efficiency.

This problem has been avoided, if the generated laser pulses would be first temporally stretched, using normal dispersion of the fiber, amplified and afterwards compressed again, using, for example, a grating. This will avoid idle of the EDFA and nonlinear effects at the high power levels in the fiber.

In this case more than 1 kW of the pump power was achieved, giving almost 1 W of the MIR radiation.

OPF in the bent waveguide structure was also investigated. The nonlinear rise of the MIR radiation in this case was observed at lower pump power levels, than in the straight waveguides, giving more than 7 nW of the MIR power at 900 mW of the pump (about 2 nW for the straight waveguide).

Optical Parametric Oscillators allow to generate power, which is orders of magnitude larger, than OPGs. Therefore these devices are more attractive for the routine measurements not under the laboratory conditions.

External and for the first time deposited mirrors for the MIR range have been

investigated and quantitatively compared. Mirrors, deposited with our equipment, have similar reflectivity as commercial mirrors. Hovewer, using the last ones has shown better finesse, as the mirrors, deposited directly on the waveguide end face. One very important factor was the substrate, which was used for the mirror. High quality sapphire with polished surfaces was showing comparable results for the commercial mirrors as well as deposited with our equipment. Nonhomogeneity and curved surface of deposited mirrors at the moment make it impossible to achieve the same finesse as the theory predicts and as it was achieved with external mirrors.

Measured threshold power of OPO with directly deposited mirrors was about a factor 3 larger, as predicted from the theory. Nevertheless, overall power characteristics (which is actually more important for the *every day* application) is in a good agreement with the theory. Output powers of more than 6 mW was obtained using 350 mW of pump power in doubly resonant configuration. An attempt to improve the flatness has been discussed, using the counter sample approach. It improves the coupling of the pump into the waveguide, reflects back the generated MIR radiation without any disturbance of the phase front and makes the device more simple for the end users.

Here, as in the case of OPG, cw pumping has been investigated first. If pulsed pumping is used instead, then it is possible to achieve even higher efficiency on one hand, and later on utilize this device for time resolved spectroscopy on the other. Definition of synchronization has been discussed. For the first time synchronously pumped integrated OPO for the MIR spectral range has been investigated.

Tuning characteristics, which are quite similar to the above mentioned OPGs and OPOs, were also measured. Despite of more complicated pump source with several adjustable parameters, tuning in the range from 2.6 to 3.6 $\mu$m was achieved.

A key point for this device is the power characteristics, which depends on the temporal relation between pump and generated signal and idler pulses. Due to the special behaviour of lithium niobate at these particular wavelengths GVM is not very critical. However, changing the time between two pump pulses in the range of 11 psec has shown strong increase of the output power level and an efficient generation of MIR radiation in case of synchronization of the pump with signal or idler. Measured results are in good agreement with theory.

A large discrepancy has been observed between measured and calculated power characteristics, which cannot be explained just by some mistakes during the experiment. A more detailed understanding behavior of the generated pulses is necessary.

The measured autocorrelation functions of the generated MIR radiation has shown, that in case, when the repetition rate of the MLL is adjusted to the signal round trip time, several idler pulses will be generated and travel simultaneously according to the dispersion properties of the material. Experimental results here are in a good agreement with the theory. More complicated idler structure has to be considered for the calculation of the MIR peak powers. Previously discussed duty cycles cannot be transferred straightforward from the pump to the MIR radiation.

## 6.2 Comparison with the Results of Other Groups and Possible Future Activities

In this section an overview of similar developments of another groups in the world will be given. Possible future activities to investigate our nonlinear devices will be discussed as well.

There is no direct competitor, who uses the same principle, process and wavelength combination, we are using. Therefore, only a relative comparison is possible.

As it has been mentioned before, the photorefractive effect is one of the big problem for the efficient generation of MIR radiation at the moderate temperature using Ti:PPLN. This problem may be avoided by doping the crystal with, for example, magnesium oxide. This technology works very well for the bulk PPLN devices [96]. MIR radiation was generated, for example, in the wavelength range from 2.6 to 4.5 $\mu$m with highest pulse energy of 17 $\mu$J using 7 % doped MgO:$LiNbO_3$.

Proton exchanged waveguides, having as well a low photorefractive damage, are also promising candidates for generation of the MIR radiation. Tunable radiation by using a difference frequency generation is shown in details in [97]. Output power up to 2.7 mW at $\lambda = 3428$ nm was reported.

Mid-infrared module with the output power up to 3 mW, generated by the DFG process in the direct-bonded ridge waveguide was reported by the NTT group [98].

The DFG process has a potential to cover larger MIR range without any mode hoping and therefore is a better candidate for spectroscopic applications in the laboratory. Tunable radiation between 3.2 and 4.8 $\mu$m using two femtosecond pump sources (one is fixed at 1.58 $\mu$m and the other is tunable between 1.05 $\mu$m and 1.18 $\mu$m) was reported [99].

Using Ti:$LiNbO_3$ waveguides the tunable radiation to measure methane absorption around 3.29 $\mu$m using fixed 1.064 $\mu$m and tunable 1.55 $\mu$m was reported [100].

Femtosecond lasers for telecommunication wavelength are available nowadays, generating high power pulses. Applying such lasers as pump source would enable in the near future to generate signal and idler pulses of high energy using a single pump pass. Reducing the sample length would allow to minimize GVM and in this way utilize high conversion efficiency. Nowadays output MIR radiation can be properly resolved in the time domain, if appropiated MIR autocorrelator would be used.

Integrated OPOs with external mirrors have low threshold power of 14 mW and therefore it is possible to operate them without any high power EDFAs, by using an efficient DFB laser. DFB lasers with maximum output power of up to 80 mW are now already available. This is a clear advantage of integrated optics in comparison with the bulk OPOs, where such low threshold of only several mW cannot be realized at the moment.

Using Zn and Tm doped waveguides reduces the photorefractive effect. Up to 65 mW of MIR radiation by DFG process is reported in [101]. If such deposited waveguides of a good quality would be available, integrated OPGs and OPOs at room temperature may be investigated further and more stable output power be expected.

Doubly resonant OPOs with deposited mirrors have been demonstrated. However due to the tuning properties, these devices are not an optimal candidate for spectroscopic applications. Deposition of the mirrors on the end face for Singly Resonant OPOs would be therefore the next step. Fine tuning and higher output power make these OPOs the preferred candidates for the environmental monitoring.

Stability of the optical cavity using the heating electrode structure is also a promising direction for further investigations. Utilizing the electro-optical effect might even be better, if excess losses due to the electrodes can be kept small.

Towards a fully integrated device more complicated OPOs cavity might be realized in the future. A part of long lithium niobate sample with the waveguides can be doped with erbium [102] and pumped at 1480 nm. Appropriate iron doping would produce a modulation of an index of refraction, creating a grating, and in this way realize a wavelength selection. Generated pump may be used later for pumping of the integrated OPG and OPOs. „All-in-one“compact nonlinear device may realized and investigated.

Generation of high power MIR radiation in the wavelength range between 2 and 4 $\mu$m these days can be done using cascaded DFG/OPA processes: as a signal source in this case may still be used ECL laser at 1.55 $\mu$m, and as a pump a high power fiber [103] or solid state lasers [104]. Holmium-doped silica fiber are able to generated up to 2.5 W output power at the wavelength range 2.1 - 2.9 $\mu$m.

Chromium-doped ZnSe, ZnS and CdSe lasers, operated at the room temperature are broadband in the wavelength range from 1.6 to 3.5 $\mu$m, delivering more than 15 W output power.

Also investigations of new crystals, transparent in MIR and having larger nonlinear coefficients (up to 100 pm/V) are of the great interests [105]. If the waveguide fabrication in such materials would be possible, then efficiencies of the nonlinear processes might be one order of magnitude larger by using the same pump power.

Bent waveguides have not jet been investigated as the integrated OPOs. Deposition of the dielectric mirror along the whole sample edge would be necessary and may be investigated in the future.

This wavelength range is still of a great interest and in the near future more sources of coherent radiation are expected for any possible application, like spectroscopy or controlling or medicine, giving a powerful tool for further and deeper investigations.

# Appendix A

# Pulse Distortion at High Power Levels

As it has been found experimentally and described above in chapter 4.6, generation of pulses of high peak power by slicing them from the pulse comb leads to the pulse distortions and, therefore, efficient conversion is not possible to obtain. Spectrum of the pump pulses in the frequency domain after every element of the pump chain has been taken (Fig. 4.10). After each optical element higher distortions were observed.

Besides of amplification of the pump pulse by EDFA, spontaneous emission can also be amplified, if not sufficient pump power for the amplifier is provided. Therefore, a preamplifier has been used. To find the origin of this distortion and an influence of the different optical elements, pump pulses were investigated in more details. Following setup has been built up (Fig. A.1). MLL has been set to emit at $\lambda = 1549.25$ nm.

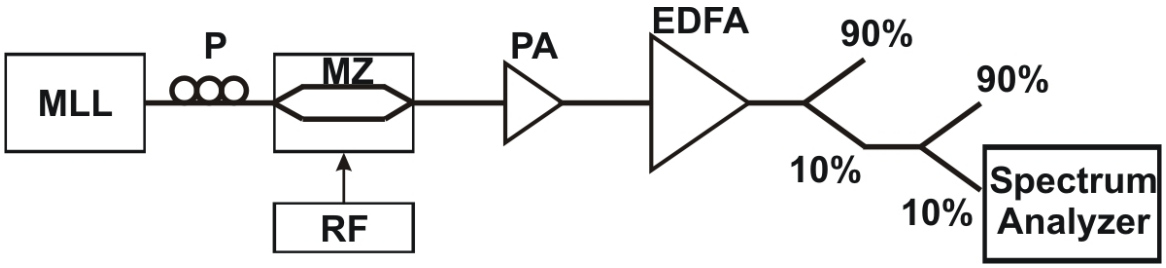


**Figure A.1:** Experimental setup for investigations of the distortion of the pump pulses: MLL - mode locked laser; P - Polarization controller; MZ - Mach-Zehnder integrated optical modulator; RF - Radio Frequency generator (f = 900 kHz; duty cycle 1/10; Amplitude = 7 V; Offset = 2.8 V); PA - Erbium doped fiber PreAmplifier; EDFA - Erbium doped fiber power amplifier.

Output parameters were optimized (pulse length of 6.4 psec at $\approx$ 0.7 nm spectral linewidth). TM polarized light was launched into the Mach-Zehnder modulator. The modulator was driven by the radio frequency generator (f = 900 kHz; duty cycle 1/10; amplitude = 7 V; offset = 2.8 V). Output optical signal was amplified in the preamplifier, and afterwards in the main amplifier. Due to the large power levels output signals of the EDFA could not be directly measured by the optical spectrum

analyzer and therefore were attenuated by two serial 10/90 couplers. Finally the pulse with 1% of the generated power was anylized.

Depending on the duty cycle different distortions might occur and have been already shown (see Fig. 4.10). Internal photodiode of the EDFA has measured 6.3 mW at the input. This power is sufficient for proper saturation of the device and to produce pulses of a good quality without ASE. Afterwards, output power level of EDFA has been continuosly increased and correspondent spectra taken. Measured results are shown in Fig. A.2.

Here is clearly seen, that for the low power output spectra of the EDFA is undisturbed. No significant changes are observed in compare with MLL pulses (spectrum of the pump pulse - see Fig. 4.7). As higher the output power level is, as more disturbed pulses leave the EDFA. For the output power level of 1.9 W several peaks instead of one are clearly observed. On the right side additionally ASE is observed. The full spectral range of the pulse starting from about 2 nm (at 0 W displayed) was increased up to 7 nm with the very inhomogeneous envelope (at 1.9 W).

These types of EDFAs are not designed to work in the pulsed mode of operation[1]. In the idle a lot of spontaneous emission is rising up, what has been proved by experiment.

As a conclusion, high power pulses might be used by slicing them from the pulse comb of the MLL. Duty cycle, used to calculate overall peak power of the generated MIR radiation cannot be directly transferred from the pulse width of the MLL and generated frequency of the electronic pulse generator. High ASE part has also to be taken into account, which is not involved in generation of coherent radiation in the MIR, but is also detected by the MIR detector. Therefore experimental results (Fig. 4.17) can be corrected. Only a part of the pump power is used to generate the coherent radiation in the MIR range. Measured results can be shifted to left and in the this way better agreement between theoretical and experimental results is expected.

[1]Unofficial recomendation of the manufacture was to used EDFA in the pulsed mode of operation for the duty cycles with not more than 40% of the idle.

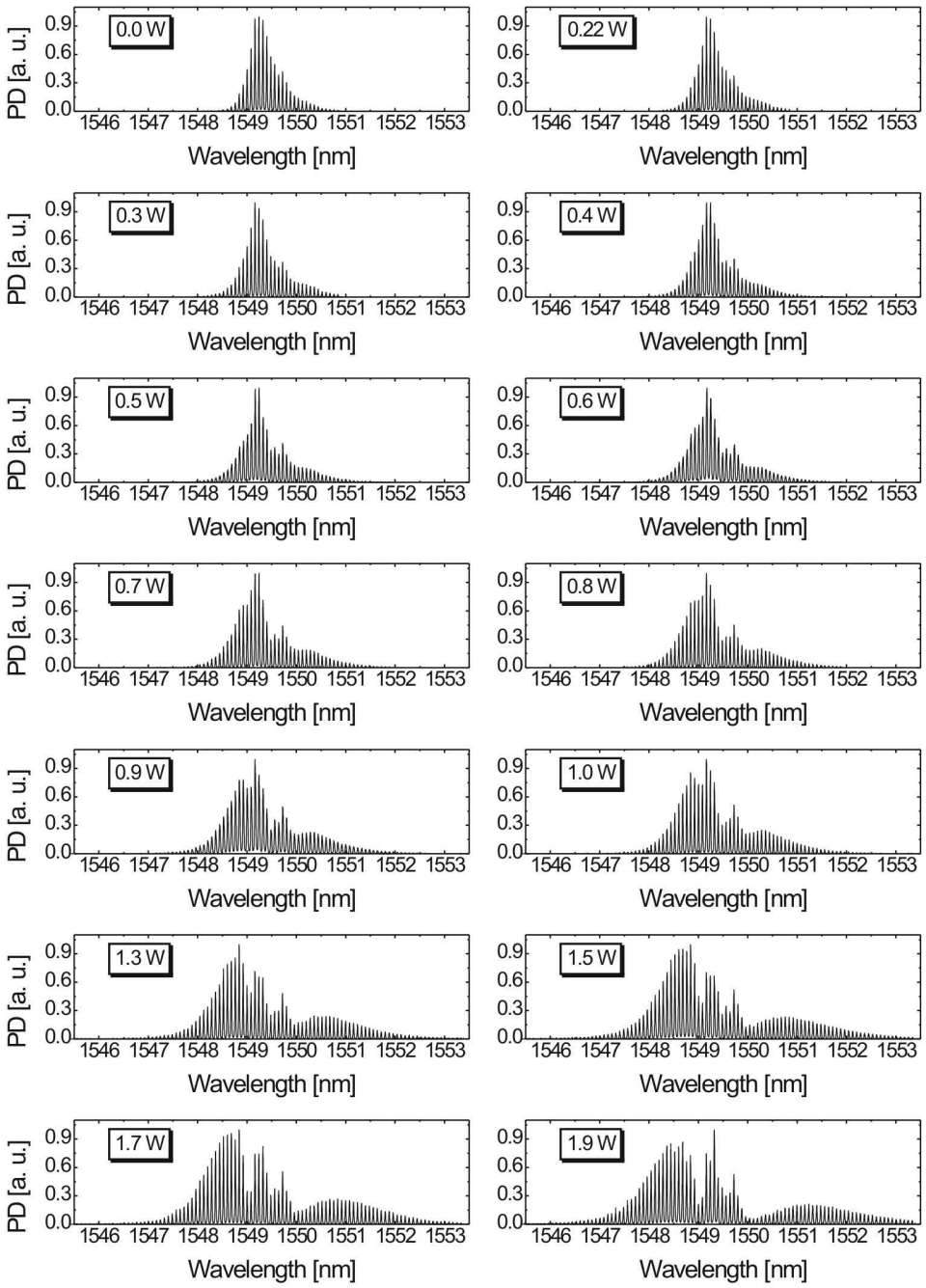


**Figure A.2:** Normalized spectra of the attenuated pump pulses, taken behind the EDFA, used for the pulse slicing. EDFA output power is shown in insets.

# Appendix B

# Cavity Stabilization Using Electrodes

OPOs, especially at the pump power levels close to the threshold, are very sensitive to any kind of fluctuations like changes in the pump power level, polarization, mechanical stress, temperature changes and so on. These instabilities may lead to the mode hopping, where the OPO will oscillate at the longitudinal frequency with the lower gain, or the resonance condition will not be fulfilled at all. For the spectroscopic applications very stable in frequency domain and output power signals are necessary. An improvement of the stability of the OPO might be realized, for example, by isolating the setup from the floor using the optical vibration isolation tables, by protecting the device from surroundings by covering the setup with appropriate boxes or improvement stabilization of the pump laser.

Usually these actions help to improve long-time stability problems (for example, temperature changes), but short-time instabilities cannot be eliminated by those methods. Feedback loop in this case should provide the necessary improvement. In the bulk OPO devices this technique is usually realized by adjusting the active cavity length to the standing changed parameters via piezo-electrical elements [106–108][1], keeping in this way the resonance condition.

Integrated OPOs, by having the goal to make a compact device with deposited mirrors, cannot implement in this manner the length control, as in the bulk devices. In this case, cavity length stabilization may be realized on the sample itself, where one part of the sample[2] is used to change the optical length, for example, via thermal expansion. By using this method it is very important to know, how fast we can change the optical cavity length by heating; whether this method is sufficient to realize the cavity stabilization.

Change of the optical path may be realized by positioning the electrodes on the waveguide, applying electrical field and using an electro-optical effect. This would provide symmetrical overlap between the optical and electrical field. Due to some

[1] At least one external mirror is placed on such type of stack piezo actuators

[2] It has to be realized on the sample part, where are no QPM domains. Otherwise phase shift in one direction will be compensated by the phase shift of the neighboring domain

reasons, which will be described in Appendix C this method was not possible to realize.

Heating elements next to the waveguides may be used instead (Fig. B.1 left). Gold electrodes, having the same width as the optical waveguides (18, 20 and 22 $\mu$m) and 0.5 mm hight, have been spattered next to the optical waveguide on the whole length of the sample (about 28 mm). Using thin pins one selected electrode has been connected to the function generator with the max amplitude voltage of 10 V. Zig-zag ramp was applied and current flow as well as the detected optical signal were measured versus the time (Fig. B.1 right). The clear response according to the applied voltage is observed.

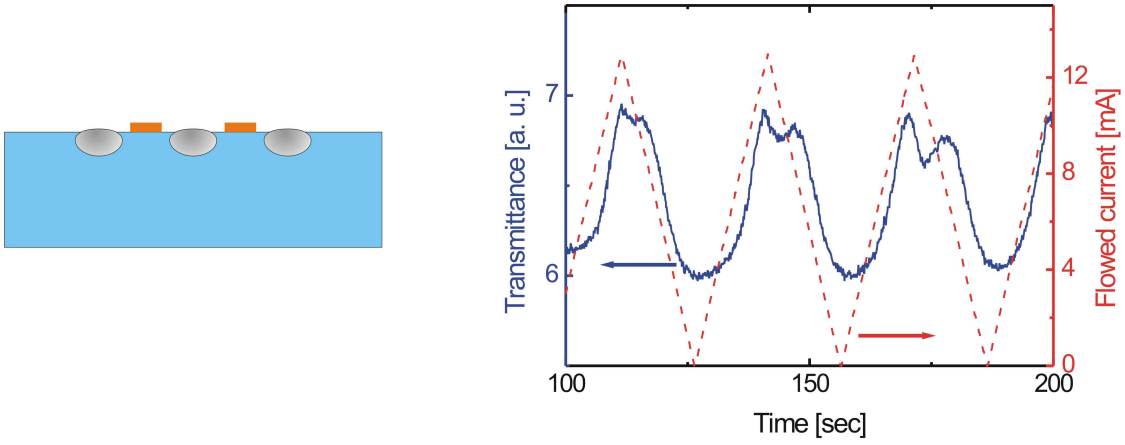


**Figure B.1:** Schematic diagram of positioning of the gold electrodes next to the optical waveguide (left); transmission signal versus the applied voltage (right).

Frequency of the generated signal has been further increased and experimental results show, that optical response after only several ms is already observed. If the second electrode would be placed next to the optical waveguide on another side, than even clearer and faster response might be achieved.

A disadvantage of this technique, that the electrodes have to be on one hand located as close as possible to the optical waveguide. On the other hand, should not cover the evanescent part of the optical field and in this way worsen the optical properties. Clear spattering technique is also necessary. Otherwise golden drops may cause some additional losses, if they would be located on the waveguides[3]. Another material (but with similar resistance) or deposition technique might be used to improve the adhesion of the metal to the lithium niobate.

Despite of some problems this method is rather compact in comparison with the bulk approaches and may be implemented in the future.

[3]It has been observed in this experiment

# Appendix C

# Looking for a Buffer Layer

In the appendix B was described, how to use the heating resistance to change the optical path inside the cavity. This relative simple method has shown a good results on the ms time scale. Some improvements to increase the response time might be done, but if control of the system has to be fulfilled in the sub ms range, then this technique is not sufficient any more.

As an option alternatively to change the optical cavity length can be a usage of a linear electro-optical effect (Pockels-effect) by applying an electrical field. The largest electro-optical coefficient for lithium niobate is $r_{33}$ ($34 \times 10^{-12}$ m/V) may be utilized by applying the field along c-axis of the crystal. In the case of $Z$-cut and $X$-propagation sample it means, that the electrode has be located on top of the optical waveguides.

Deposition of electrodes directly on the waveguide will not work, while in this case no optical guiding would be possible. Therefore, a thin buffer layer is necessary, which will isolate electrodes from the waveguides. Additionally it needs to have a low index of refraction and low absorption at the pump and MIR spectral range.

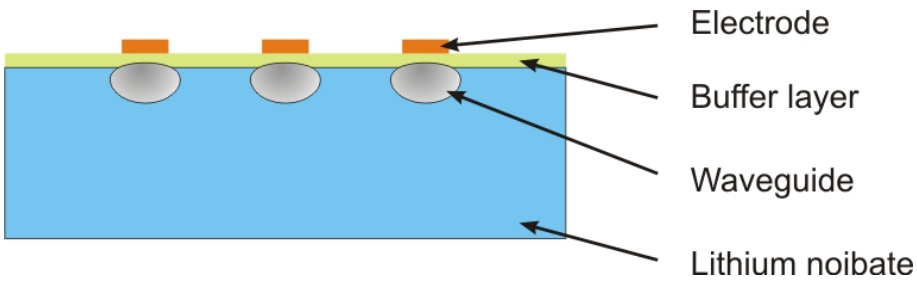


**Figure C.1:** Schematic diagram of positioning of the electrodes on the waveguides using the buffer layer.

$SiO_2$ has high transmission in the near and mid infrared and has been already used as a component for the fabrication of the MIR mirrors, showing excellent results. The losses of the sample, which has to be deposited with $SiO_2$ layer, were measured before and after the deposition.

If before the deposition average damping in the sample was below 0.07 dB/cm and in some waveguides even below 0.05 dB/cm, then after they were in the range 0.42 - 0.49 dB/cm. Assuming the usual length of MIR samples is about 8 to 9 cm and the device will be used as a cavity, where the round trip losses strongly define the threshold, then the value of about 7 dB is achieved. This is equal to the damping of the wave by the factor 4.7 after just one round trip. High damping losses make this material unusable as the buffer layer.

Next approach has been done with a commercial glue. According to the specification, it is highly transparent in the MIR range. Before the glue deposition waveguide losses of the length 55 mm were in the best case about 0.03 dB/cm. After the glue deposition, which did not cover the sample along the whole waveguide length, but only partially in the middle, no low-resonance dependence has been observed at all. All waveguides have shown similar aperiodical behavior. The difficulty in this case, that there is no option to remove the glue afterwards, if it is necessary. In this way no further investigations were possible.

As a next candidate $Al_2O_3$ was deposited, which is also highly transparent in the MIR range. Before deposition the losses of the sample (28 mm long) were near 0.05 dB/cm and after in some cases they achieved 0.2 dB/cm, but in some waveguides were staying below 0.1 dB/cm. Before deposition overall waveguide losses have a quite homogeneous distribution, afterwards the changes were from several percents to the factor 3 - 4.

Another advantage of the deposition of the buffer layer is reducing the coupling losses and improving the integrated cavity by using the deposited mirrors. As it has been discussed already in chapter 5.3.1, flat mirror surface is very important at the waveguide end face. Due to the mirror location at the edge of the waveguide, some rounding is not unavoidable. Deposited buffer layer on top of the waveguide in this case may help to get even flatter surface.

At this point it can be concluded, that, on one side, the buffer layer may be used to realize the feedback loop for the integrated OPOs, but threshold and overall power levels will be increased in this case. Inhomogeneities in the buffer layer and nonperfect technology of their deposition make difficult the fabrication of waveguides with good optical properties for the MIR spectral range. In case, where only some part of the waveguide has to be covered, it is difficult to predict, how the guiding properties will be changed. Here also has to be taken into account, that the size of MIR modes is larger, than for the near infrared and therefore a part of the field (evanescent part) is larger for the MIR. This can be a reason, why the waveguides for the near infrared do not have such a dramatic increase of the losses.

If there will be found material with very good properties to deposit it on the waveguide surface and does not reduce overall losses, then really one further step can be done towards the integrated OPOs.

# Appendix D

# Improvement of Sellmeier Equation for the MIR Range

This work was concentrated on using the largest $d_{33}$ nonlinear coefficient of lithium niobate and therefore extraordinary index of refraction $n_e$ was taken. To calculate precisely the domain periodicity and therefore phase matching curve it is necessary to know exactly $n_e$. Empirical formula to calculate $n_e$ at the particular wavelength and the temperature is called *Sellmeier equation*. Main references for the theoretical calculations for this work were [92, 93]. In between this relationship was experimentally corrected and improved for the MIR range from 2.8 $\mu$m to 4.8 $\mu$m at the temperatures 20 - 180 °C [94]. The relationship has the form:

$$n_e^2 = a_1 + b_1 f + \frac{a_2 + b_2 f}{\lambda^2 - (a_3 + b_3 f)^2} + \frac{a_4 + b_4 f}{\lambda^2 - a_5^2} - (a_6 + b_5 f)\lambda^2 \tag{D.1}$$

where $\lambda$ is the wavelength of interest in $\mu$m and $f$ is temperature dependent parameter:

$$f = (t - 24.5℃)(t + 570.82) \tag{D.2}$$

and following $a_i$ and $b_i$ coefficients D.1:

| Parameter | $a_1$ | $a_2$ | $a_3$ | $a_4$ | $a_5$ | $a_6$ |
|---|---|---|---|---|---|---|
| Value | 5.39121 | 0.100473 | 0.20692 | 100 | 11.34927 | 1.544E-2 |
| Parameter | $b_1$ | $b_2$ | $b_3$ | $b_4$ | $b_5$ | - |
| Value | 4.96827E-7 | 3.862E-8 | -0.89E-8 | 2.657E-5 | 9.62119E-10 | - |

**Table D.1:** $a_i$ and $b_i$ for the improved Sellmeier equation D.1 for lithium niobate from 2.8 $\mu$m to 4.8 $\mu$m at the temperatures 20 - 180 °C.

To calculate $n_e$ in the waveguide, the following relation has been used:

$$n_e = n_{e,bulk} + \Delta n \tag{D.3}$$

where $n_{e,bulk}$ is the extraordinary bulk refractive index of material, taken from D.1; $\Delta n$ is the increase the index of refraction in comparison with the bulk material, calculated by the „Focus“-program.

# Appendix E

# MIR Samples

MIR samples, used in experiments, are listed here:

| Sample | Bent (y/n) | L [mm] | $\Lambda$ $\mu$m | $\alpha$ dB/cm | $w$ $\mu$m | Experiment |
|---|---|---|---|---|---|---|
| Pb402z | no | 89.5 | 31.20 - 31.60 | 0.101 | 20 | OPG - power |
| Pb403z | no | 94.4 | 31.20 - 31.60 (31.44) | 0.131 | 20 | OPG - tuning |
| PbW37z | yes | R + 2 × 24 mm | 31.60 | - | 18 | OPG - tuning |
| PbW40z | yes | R + 2 × 37 mm | 31.60 | - | 18 | OPG - power |
| Pb686z | no | 90.2 | 31.20 - 31.60 | 0.100 | 18, 20, 22 | Mirror fabrication |
| Pb622z | no | 68 | 31.20 - 31.60 | 0.062 | 20 | Synch. OPO |
| Pb623z | no | 68 | 31.20 - 31.60 (31.10) | 0.065 | 18 | Synch. OPO |
| Pb678z | no | 68.4 | 31.20 - 31.60 | $< 0.060$ | 18, 20, 22 | Counter-sample |
| Pb686z | no | 90. | 31.20 - 31.60 | $< 0.100$ | 18, 20, 22 | Counter-sample |

**Table E.1:** An overview table of MIR samples, used in this work: R is the length of the bent part.

# Bibliography


[1] E. Hecht, *Optics*. Addison-Wesley, 1998. 5, 12

[2] http://cfa-www.harvard.edu/hitran/. 6

[3] K. A. Tillman, D. T. Reid, R. R. J. Maier, and E. D. McNaghten, "Mid-infrared absorption spectroscopy of methane across a 14.4 THz spectral range using a broadband femtosecond optical parametric oscillator based on aperiodically poled lithium niobate," *Proceedings of SPIE*, vol. 5989, 2005. 6

[4] D. S. Boyd and F. Petitcolin, "Remote sensing of the terrestrial environment using middle infrared radiation (3.0 - 5.0 $\mu$m)," *International journal of remote sensing*, vol. 25, pp. 3343–3368, 2004. 6

[5] T. Töpfer, K. P. Petrov, Y. Mine, D. Jundt, R. F. Curl, and F. K. Tittel, "Room-temperature mid-infrared laser sensor for trace gas detection," *Appl. Opt.*, vol. 36, pp. 8042–8049, 1997.

[6] R. Bartlome and M. W. Sigrist, "Applications of mid-infrared laser sources to trace gas sensing," *Proceedings of the conference "Mid-Infrared Coherent Sources (MICS) 2005"*, vol. Fr3., 2005.

[7] F. K. Tittel, Y. Bakhirin, A. A. Kosterev, and R. F. Curl, "Semiconductor laser based chemical sensor technology: recent advantages and applications," *Proceedings of the conference "Mid-Infrared Coherent Sources (MICS) 2005"*, vol. Fr1., 2005. 6

[8] D. J. Bamford, D. J. Cook, S. J. Sharpe, and A. D. V. Pelt, "Widely tunable rapid-scanning mid-infrared laser spectrometer for industrial gas process stream analysis," *Apl. Opt.*, vol. 49, pp. 3958–3968, 2007. 6

[9] E. Sorokin, "Spectroscopic applications of $Cr^{2+}$-based lasers," *Proceedings of the conference „Mid-Infrared Coherent Sources (MICS) 2005"*, vol. Fr.4, 2005.

[10] A. Ngai, S. Persijn, G. von Basum, and F. Harren, "Automatically tunable continuous-wave optical parametric oscillator for high-resolution spectroscopy and sensitive trace-gas detections," *Applied Physics B*, vol. 85, pp. 173–180, 2006. 6

[11] D. Halmer, S. Thelen, P. Hering, and M. Mürtz, "Online monitoring of ethane traces in exhaled breath with a difference frequency generation spectrometer," *Applied Physics B*, vol. 85, pp. 437–443, 2006. 6

[12] H. H. M. (Editor) and M. J. (Editor), *Infrared Spectroscopy: New Tool in Medicine*. Spie Proceedings Series, 1998. 6

[13] T. Tamir, *Integrated Optics*. Springer-Verlag Berlin Heidelberg New York, 1979. 7, 21

[14] C. L. Tang and L. K. Cheng, *Fundamentals of Optical Parametric Processes and Oscillators*. Harwood academic publishers, 1995. 7

[15] C. Montes, A. Picozzi, and K. Gallo, "Ultra-coherent output from an incoherent cw-pumped singly resonant optical parametric oscillator," *Opt. Commun.*, vol. 237, pp. 437–449, 2004. 8

[16] A. Picozzi and M. Haelterman, "Parametric three-wave soliton generated from incoherent light," *Phys. Rev. Lett.*, vol. 86, pp. 2010–2013, 2001. 8

[17] J. A. Armstrong, N. Bloembergen, J. Ducuing, and P. S. Pershan, "Interactions between light waves in a nonlinear dielectric," *Phys. Rev.*, vol. 127, pp. 1918 – 1939, 1962. 8, 18

[18] J. Son, Y. Yuen, S. Orlov, and L. Hesselink, "Sub-micron ferroelectric domain engineering in liquid phase epitaxy linbo$_3$ by direct-write e-beam techniques," *Journal of Crystal Growth*, vol. 281, pp. 492–500, 2005. 9

[19] C. L. Sones, C. E. Valdivia, J. G. Scott, S. Mailis, R. W. Eason, D. A. Scrymgeour, V. Gopalan, T. Jungk, and E. Soergel, "Ultraviolet laser-induced submicron periodic domain formation in congruent undoped lithium niobate crystals," *Apl. Phys. B: Lasers and Optics*, vol. 80, pp. 341–344, 2005. 9

[20] M. C. Hübner, D. Hofmann, and W. Sohler, "Efficient integrated Ti:PPLN MIR-optical parametric generator," *Technical Digest Nonlinear Guided Waves and their Applications (NLGW'02), Stresa/Italy*, 2002. 9

[21] X. Xie, A. M. Schober, C. Langrock, R. V. Roussev, J. R. Kurz, and M. M. Fejer, "Picojoule threshold, picosecond optical parametric generation in reverse proton-exchanged lithium niobate waveguides," *J. Opt. Soc. Am.*, vol. B21-7, pp. 1397–1402, 1994. 9

[22] J. R. Carruthers, I. P. Kaminow, , and L. W. Stulz, "Diffusion kinetics and optical waveguiding properties of outdiffused layers in lithium niobate and lithium tantalate," *Appl. Opt.*, vol. 13, pp. 2333–2342, 1974. 11

[23] W. K. Burns, D. H. Klein, and E. J. West, "Ti-diffusion in Ti:$LiNbO_3$ planar and channel optical waveguides," *J. Appl. Phys.*, vol. 50, pp. 6175–6182, 1979. 11

[24] S. K. Korotky and R. C. Alferness, "Ti:$LiNbO_3$ integrated optic technology," *L. D. Hutcheson (Ed.): Integrated optical circuits and components, Marcel Dekker, Inc., New York*, 1987. 11

[25] F. Caccavalle, P. Chakraborty, A. Copobianco, G. Gianello, and I. Monsoure, "Characterization and optimization of Ti-diffused $LiNbO_3$ optical waveguides by second diffusion of magnesium," *J. Appl. Phys.*, vol. 78, pp. 187–193, 1995. 12

[26] D. Hofmann, "Nichtlineare, integriert optische frequenzkonverter für das mittlere infrarot mit periodisch gepolten Ti:$LiNbO_3$-Streifenwellenleiter," Ph.D. dissertation, University of Paderborn, 2001. 12, 19, 29, 35, 55, 56

[27] E. Strake, G. P. Bava, and I. Montrosset, "Guided modes of Ti:$LiNbO_3$ channel waveguides: A novel quasi-analytical technique in comparison with the scalar finite-element method," *J. Lightwave Technol.*, vol. 6, pp. 1126–1135, 1988. 12, 30

[28] W. Grundkötter, "Theoretische Beschreibung quasi-phasenangepasster optischer Frequenzkonversion in periodisch gepolten Wellenleiter," 1999, Diplomarbeit Universität Paderborn. 13

[29] S. Korotky, W. Minford, L. Buhl, M. Divino, and R. Alferness, "Mode size and method for estimating the propagation constant of single-mode Ti:$LiNbO_3$ strip waveguides," *IEEE Journal of Quantum Electronics*, vol. 18, pp. 1796–1801, 1982. 14

[30] G. S. He and S. H. Liu, *Physics on nonlinear optics*. World Scientific, 1999. 14

[31] P. A. Franken, A. E. Hill, C. W. Peters, and G. Weinreich, "Generation of optical harmonics," *Phys. Rev. Lett*, vol. 7, pp. 118–120, 1961. 14

[32] R. S. Weis and T. K. Gaylord, "Lithium niobate: summary of physical properties and crystal structure," *Appl. Phys.*, vol. 37, pp. 191–203, 1985. 15

[33] A. Räuber, "Chemistry and physics of lithium niobate," *North-Holland Publishing Company*, vol. vol. 1 of Current topics in materials science, p. 481, 1978. 16

[34] I. Shoji, T. Kondo, A. Kitamoto, M. Shinare, and R. Ito, "Absolut scale of second-order nonlinear-optical coefficients," *Opt. Soc. Am. B*, vol. 14, p. 2268, 1997. 16

[35] L. E. Myers, R. C. Eckardt, M. M. Fejer, R. L. Byer, W. R. Bosenberg, and J. W. Pierce, "Quasi-phase-matched optical parametric oscillators in bulk periodically poled $LiNbO_3$," *Opt. Soc. Am. B*, vol. 12, p. 2102, 1995. 16, 18

[36] A. Yariv, *Quantum Electronics.* John Wiley & Sons, 1988. 17, 55

[37] G. Rosenman, P. Urenski, A. Agronin, A. Arie, and Y. Rosenwaks, "Nanodomain engineering in $RbTiOPO_4$ ferroelectric crystals," *Appl. Phys. Lett.*, vol. 82, pp. 3934–3936, 2003. 18

[38] H. Suche and W. Sohler, *Wave Electronics*, vol. 3, p. 269, 1979. 24

[39] H. P. Weber, F. A. Dunn, and W. W. Leibolt, *Appl. Opt.*, vol. 12, p. 755, 1973.

[40] K. H. Haegele and R. Ulrich, *Opt. Lett.*, vol. 4, p. 60, 1979.

[41] A. M. Glass, I. P. Kaminow, A. A. Allmann, and D. H. Olson, *Apl. Opt.*, vol. 19, p. 276, 1980. 24

[42] I. P. Kaminow and L. W. Stulz, *Apl. Phys. Lett.*, vol. 33, p. 62, 1978. 24

[43] R. Regener and W. Sohler, "Loss in low-finesse Ti:$LiNbO_3$ optical waveguide resonators," *Appl. Phys. B*, vol. 36, pp. 143–147, 1985. 24

[44] K. Morishita, "Index profiling of three-dimensional optical waveguides by the propagation-mode near-field method," *J. Lightw. Technol.*, vol. LT-4, pp. 1120–1124, 1989. 27

[45] L. McCaughan and E. Bergmann, "Index distribution of optical waveguides from their mode profile," *J. Lightw. Technol.*, vol. LT-1, pp. 241–244, 1983. 27

[46] W. T. Anderson and D. L. Philen, "Spot size measurements for singlemode fibersa comparison of four techniques," *J. Lightw. Technol.*, vol. LT-1, pp. 20–26, 1983. 27

[47] M. Artiglia, G. Coppa, P. D. Vita, M. Potenza, and A. Sharma, "Mode field diameter measurements in single-mode optical fibers," *J. Lightw. Technol.*, vol. 7, pp. 1139–1152, 1989. 27

[48] S. E. Harris, M. K. Oshman, and R. L. Byer, "Observation of tunable optical parametric fluorescence," *Phys. Rev. Lett.*, vol. 18, pp. 732–734, 1967. 29

[49] H. Suche, B. Hampel, H. Seibert, and W. Sohler, "Parametric fluorescence, amplification and oscillation in Ti:$LiNbO_3$ optical waveguides," *„SPIE Proc. "Integrated Optical Circuit Ingineering II", Cambridge*, vol. 578, p. 156, 1985. 29

[50] B. Hampel and W. Sohler, "Optical parametric fluorescence in Ti:$LiNbO_3$ channel waveguides," *„SPIE Proc. "Integrated Optical Circuit Ingineering III", Insbruck*, vol. 651, p. 229, 1986. 29

[51] H. Herrmann, "Optisch nichtlineare Differenzfrequenzerzeugung abstimbarer, kohärenter Strahlung im mittleren Infrarotbereich in Ti:$LiNbO_3$-Streifenwellenleiter," Ph.D. dissertation, University of Paderborn, 1991. 30

[52] http://www.rp-photonics.com/optical_fiber_communications.html. 32

[53] P. Baldi, M. Sundheimer, K. E. Hadi, M. P. de Micheli, and D. B. Ostrowsky, "Comparison between difference-frequency generation and parametric fluorescence in quasi-phase-matched lithium niobate stripe waveguides," *IEEE Journal of selected topics in quantum electronics*, vol. 2 - No.2, pp. 385–395, 1996. 35

[54] W. Grundkötter, "Dynamik nichtlinearer Wechselwirkungen zweiter Ordnung in integriert optischen Wellenleitern," Ph.D. dissertation, University of Paderborn, 2005. 38, 43, 50, 70, 73, 77, 78

[55] D. Strickland and G. Mourou, *Opt. Commun.*, vol. 56, p. 219, 1985. 43

[56] E. V. Kovalchuk, D. Dekorsy, A. I. Lvovsky, C. Braxmayer, J. Mlynek, A. Peters, and S. Schiller, "High-resolution doppler-free molecular spectroscopy with a continuous-wave optical parametric oscillator," *Opt. Lett.*, vol. 26, pp. 1430–1432, 2001. 53, 55

[57] J. A. Giordmaine and R. C. Miller, "Tunable coherent parametric oscillation in $LiNbO_3$ at optical frequencies," *Phys. Rev. Lett.*, vol. 14, pp. 973–976, 1995. 55

[58] K. A. Tillman, R. R. J. Maier, D. T. Reid, and E. D. McNaghten, "Mid-infrared absorption spectroscopy across a 14.4 thz spectral range using a broadband femtosecond optical parametric oscillator," *Apl. Phys. Lett.*, vol. 85, pp. 3366–3368, 2004. 55

[59] G. von Basum, D. Halmer, P. Hering, M. Mürtz, S. Schiller, F. Müller, A. Popp, and F. Kühnemann, "Parts per trillion sensitivity for ethane in air with an optical parametric oscillator cavity leak-out spectrometer," *Apl. Phys. Lett.*, vol. 29, pp. 797–799, 2004.

[60] M. E. Klein, C. K. Laue, D.-H. Lee, K.-J. Boller, and R. Wallenstein, "Diode-pumped singly resonant continuous-wave optical parametric oscillator with wide continuous tuning of the near-infrared idler wave," *Opt. Lett.*, vol. 25, pp. 490–492, 2000. 55

[61] J. Raffy, T. Debuisschert, J.-P. Pocholle, , and M. Papuchon, *Appl. Optics*, vol. 33, p. 985, 1994. 55

[62] http://www.adlares.de/index-en.php. 55

[63] W. Sohler and H. Suche, "Optical parametric oscillation in Ti-difused $LiNbO_3$ optical waveguide resonators," *Technical digest of the 3rd Int. Conf. on Int. Opt. and Opt. Fiber Commun., IOOO'81, San Francisco, paper WB1*, pp. 89–90, 1981. 55

[64] H. Suche, "Optisch parametrische Verstärkung und Oszillation in Ti-diffundierten $LiNbO_3$ Wellenleiterresonatoren," Ph.D. dissertation, Univ. Dortmund, Germany, 1981. 55

[65] A. Ashkin, G. Boyd, J. Dziedzic, R. Smith, A. Ballman, J. Levinstein, and K. Nassau, "Optically induced refractive index inhomogeneities in $LiNbO_3$ and $LiTaO_3$," *Apl. Phys. Lett.*, vol. 9, pp. 72–74, 1966. 55

[66] A. Haradaa and Y. Nihei, "Bulk periodically poled MgO-$LiNbO_3$ by corona discharge method," *Apl. Phys. Lett.*, vol. 69, pp. 2629–2631, 1996. 55

[67] M. Wengler, U. Heinemeyer, and K. Buse, "Light-induced domain patterning in magnesium-doped lithium niobate crystals," *Conference on Lasers and Electro-Optics Europe, CLEO/Europe-2005*, p. 268, 2005.

[68] K. Nakamura, J. Kurz, K. Parameswaran, and M. M. Fejer, "Periodic poling of magnesium-oxide-doped lithium niobate," *Phys. Lett.*, vol. 91, pp. 4528–4534, 2002.

[69] L. Huang, D. Hui, D. Bamford, S. Field, I. Mnushkina, L. Myers, and J. Kayser, "Periodic poling of magnesium-oxide-doped stoichiometric lithium niobate grown by the top-seeded solution method," *Appl. Phys. B*, vol. 72, pp. 301–306, 2001.

[70] A. V. Okishev and J. D. Zuegel, "Intracavity-pumped Raman laser action in a mid-IR, continuous-wave (cw) MgO:PPLN optical parametric oscillator," *Appl. Phys. B*, vol. 14, pp. 12 169–12 173, 2006.

[71] N. Lyi, K. Kitamura, Y. Yajima, S. Kimura, Y. Furukawa, and M. Sato, "Defect structure model of MgO-Doped $LiNbO_3$," *Journal of solid state chemistry*, vol. 18, pp. 148–152, 1995. 55

[72] A. Henderson and R. Stafford, "Intra-cavity power effects in singly resonant cw OPOs," *Apl. Phys. B*, vol. 85, pp. 181–184, 2006. 55

[73] H. Ishizuki and T.Taira, "High-energy quasi-phase-matched optical parametric oscillation in a periodically poled MgO:$LiNbO_3$ device with a 5 mm $\times$ 5 mm aperture," *Opt. Lett.*, vol. 30-21, pp. 2918–2920, 2005.

[74] J. Saikawa, M. Fujii, H. Ishizuki, and T. Taira, "High-energy, narrow-bandwidth periodically poled Mg-doped $LiNbO_3$ optical parametric oscillator with a volume bragg grating," *Apl. Phys. Lett.*, vol. 32-20, pp. 2996–2998, 2007.

[75] X. Zhang, B. Yao, Y. Wang, Y. Ju, and Y. Zhang, "Middle-infrared intracavity periodically poled MgO:$LiNbO_3$ optical parametric oscillator," *Chin. Opt. Lett.*, vol. 5, pp. 426–427, 2007.

[76] A. Zavadilova, V. Kubeek, and J.-C. Diels, "Picosecond optical parametric oscillator pumped synchronously, intracavity, by a mode-locked Nd:$YVO_4$ laser," *Laser Phys. Lett.*, vol. 4, pp. 103–108, 2006. 55

[77] A. Hellwig, H. Suche, R. Schrör, and W. Sohler, "Titanium-indiffused waveguides in magnesium oxide doped stoichiometric lithium niobate (MgO:SLN)," *Proc. European Conference on Integrated Optics (ECIO '05), Grenoble*, pp. 254–257, 2005. 55

[78] G. P. Bava, I. Montrosset, W. Sohler, and H. Suche, "Numerical modelling of Ti:$LiNbO_3$ integrated optical parametric oscillators," *IEEE J. of Quantum Electronics*, vol. QE-23, pp. 42–51, 1987. 55

[79] W. Karthe and R. Müller, *Integrierte Optik*. Akademische Verlagsgeselschaft Geest & Portig K.-G., 1991. 57

[80] http://www.rp-photonics.com/dielectric_mirrors.html. 57

[81] http://www.dentonvacuum.com/PDFs/Tech_papers/iad.pdf. 58

[82] V. Quiring et al. 59

[83] C. W. Hoyt, M. Sheik-Bahae, and M. Ebrahimzadeh, "High-power picosecond optical parametric oscillator based on periodically poled lithium niobate," *Opt. Lett.*, vol. 27, pp. 1543–1545, 2002. 67

[84] S. D. Butterworth, V. Pruneri, and D. C. Hanna, "Optical parametric oscillation in periodically poled lithium niobate based on continuous-wave synchronous pumping at 1.047 $\mu$m," *Opt. Lett.*, vol. 21, pp. 1345–1347, 1996.

[85] M. Ebrahimzadeh, P. J. Phillips, and S. Das, "Low-threshold mid-infrared optical parametric oscillation in periodically poled $LiNbO_3$ synchronously pumped by a Ti:sapphire laser," *Appl. Phys. B: Lasers and Optics*, vol. 72, pp. 793–801, 2001.

[86] T. Kartaloğlu, K. G. Köprülü, O. Aytür, M. Sundheimer, and W. P. Risk, "Femtosecond optical parametric oscillator based on periodically poled $KTiOPO_4$," *Opt. Lett.*, vol. 23, pp. 61–63, 1998.

[87] C. McGowan, D. T. Reid, Z. E. Penman, M. Ebrahimzadeh, W. Sibbett, and D. H. Jundt, "Femtosecond optical parametric oscillator based on periodically poled lithium niobate," *J. Opt. Soc. Am. B*, vol. 15, pp. 694–701, 1998. 67

[88] G. D. Smith and R. A. Palmer, *Fast Time-resolved Mid-infrared Spectroscopy Using an Interferometer.* WileyEurope, 2002. 67

[89] S. Okretic, N. Voelkl, and H. W. Siesler, *Mid- and near-infrared spectroscopy of polymers: time-resolved studies and remote sensing applications.* Proc. SPIE Vol. CR69, p. 3-22, Materials Characterization and Optical Probes Techniques, 1997.

[90] M. Saito and Y. Okubo, "Time-resolved infrared spectrometry with a focal plane array and a galvano-mirror," *Opt. Lett.*, vol. 32, pp. 1656–1658, 2007. 67

[91] M. A. Watson, M. V. OConnor, P. S. Lloyd, D. P. Shepherd, D. C. Hanna, C. B. E. Gawith, L. Ming, P. G. R. Smith, and O. Balachninaite, "Extended operation of synchronously pumped optical parametric oscillators to longer idler wavelengths," *Opt. Lett.*, vol. 27, pp. 2106–2109, 2002. 67

[92] G. J. Edwards and M. Lawrence, "A temperature-dependent dispersion equation for congruently grown lithium niobate," *Opt. Quant. Elect.*, vol. 20, pp. 373–375, 1984. 68, 95

[93] D. H. Jundt, "Temperature-dependent sellmeier equation for the index of refraction, $n_e$, in congruent lithium niobate," *Opt. Lett.*, vol. 22, pp. 1553–1555, 1997. 68, 95

[94] L. H. Deng, X. M. Gao, Z. S. Cao, W. D. Chen, Y. Q. Yuan, W. J. Zhang, and Z. B. Gong, "Improvement to sellmeier equation for periodically poled $LiNbO_3$ crystal using mid-infrared difference-frequency generation," *Optics Communications*, vol. 268, pp. 110–114, 2006. 68, 95

[95] S. K. Korotky, E. A. J. Marcatili, J. J. Veselka, and R. H. Bosworth, "Greatly reduced losses for small radius bends in Ti:$LiNbO_3$ waveguides," *App. Phys. Lett.*, vol. 48, pp. 92–94, 1985. 81

[96] S. Lin and T. Suzuki, "Tunable picosecond mid-infrared pulses generated by optical parametric generation/amplification in MgO:$LiNbO_3$ crystals," *Opt. Lett.*, vol. 21, pp. 579–581, 1996. 84

[97] R. V. Roussev, "Optical-frequency mixers in periodically poled lithium niobate: materials, modeling and characterization," Ph.D. dissertation, Stanford University, USA, 2007. 84

[98] http://www.phlab.ecl.ntt.co.jp/eng/theme/2007/e2007_16_01.pdf/. 84

[99] C. Erny, K. Moutzouris, J. Biegert, D. Kühlke, F. Adler, A. Leitenstorfer, and U. Keller, "Mid-infrared difference-frequency generation of ultrashort pulses tunable between 3.2 and 4.8 $\mu$m from a compact fiber source," *Opt. Lett.*, vol. 32, pp. 1138–1140, 2007. 84

[100] D. Büchter, "Generation of Mid-IR Radiation by Frequency Mixing in Ti:PPLN Waveguides for Environmental Analysis," Master's thesis, Universität Paderborn, Germany, 2007. 84

[101] M. Asobe, O. Tadanaga, T. Yanagawa, T. Umeki, Y. Nishida, and H. Suzuki, "High-power mid-infrared wavelength generation using difference frequency generation in damage-resistant Zn:$LiNbO_3$ waveguide," *Electronics Letters*, vol. 44, 2008. 84

[102] S. Reza, "Acoustooptically tunable waveguide lasers in erbium doped lithium niobate," Ph.D. dissertation, University of Paderborn, 2006. 85

[103] M. Polnau and S. D. Jackson, "Advanced in Mid-infrared fiber lasers," *Springer Book Mid-Infrared Coherent Sources and Applications, M. Ebrahimzadeh and I.T. Sorokina, eds., NATO Science for Peace and Security Series B: Physics and Biohysics*, pp. 315–346, 2007. 85

[104] I. T. Sorokina, "Broadband mid-infrared solid state lasers," *Springer Book Mid-Infrared Coherent Sources and Applications, M. Ebrahimzadeh and I.T. Sorokina, eds., NATO Science for Peace and Security Series B: Physics and Biohysics*, pp. 225–260, 2007. 85

[105] L. Isaenko, A. Yelisseyev, A. Tkachuk, and S. Ivanova, "New monocrastals with low phonon energy for MID-IR lasers," *Springer Book Mid-Infrared Coherent Sources and Applications, M. Ebrahimzadeh and I.T. Sorokina, eds., NATO Science for Peace and Security Series B: Physics and Biohysics*, pp. 3–66, 2007. 85

[106] F. Kühnemann, F. Müller, G. von Basum, D. Halmer, A. Popp, S. Schille, P. Hering, and M. Mürtzr, "CW-OPO based cavity-leak-out spectrometer for ultra-sensitive and selective mid infrared trace gas analysis," http://www.exphy.uni-duesseldorf.de/Publikationen/Papers/FK_5337-18_OPOCALOS.pdf. 91

[107] J. H. Scofield, "A frequency-domain description of a lock-in amplifier," *American Journal of Physics*, vol. 20, pp. 129–133, 1994.

[108] M. Kumagai, H. Kanamori, M. Matsushita, and T. Kato, "Development of phase-lock system between two single-mode lasers for optical-optical double resonance spectroscopy," *Jp. J. Appl. Phys.*, vol. 38, pp. 6102–6106, 1999. 91

# Acknowledgement

For this great opportunity to work in the highly technological field of „Integrated Optics“ I would like to give many thanks to Prof. Dr. Wolfgang Sohler. It was not easy to get an understanding of the physics behind of those processes we investigated together. His large background and a lot of experience, knowledges and feeling in this field were irreplaceable. During my work I was responsible (most of the time along) for the activities in the MIR range in our group. This and a very modern and very well-equipped laboratory have helped me to collect and increase my experience I had already before. I have really enjoyed to build up a setup for new and more exciting experiments and be the first one to obtain the new interesting results.

I also would like to thank Dr. Hubertus Suche and Dr. Harald Herrmann. Their advices and helps were very useful to solve different kinds of scientific problems, which are a part of our work.

My experimental results would be not very exciting, if no theoretical results confirmed this. For providing me with the theoretical results for OPGs as well as for OPOs I thank a lot Dr. Werner Grundkötter.

This work would be useless, if there were no samples of a good quality. For the fabrication of excellent waveguides and continuous discussions to characterize and improve sample and resonator cavity properties I am very grateful to Viktor Quiring and Raimond Ricken.

For the nonscientific support in any aspects of my stay in Paderborn I want to sincerely thank Mrs. Irmgard Zimmermann. She could provide me in the everyday life with some advices, where the knowledges in the Integrated Optics are useless.

I would like to thank as well all the group members who made a very kind working atmosphere. Your good mood and your knowledges were important and helpful in my work here.

I have written one more page in the book of my life. The experience I got here will help me in the future to open new and even more interesting horizons.

Sergey Orlov
Paderborn, October 2008